

# Electrocatalytic Activities of Supported Pt Nanoparticles for Low-Temperature Fuel Cell Applications

by

**Wenchao Sheng**

B.S. Chemistry  
Tongji University, Shanghai, 1999  
M.S. Chemistry  
Tongji University, Shanghai, 2002

Submitted to the Department of Chemistry  
in Partial Fulfillment of the Requirements  
for the Degree of

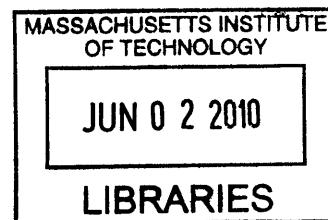
**DOCTOR OF PHILOSOPHY**

at the

MASSACHUSETTS INSTITUTE OF TECHNOLOGY

June 2010

© 2010 MASSACHUSETTS INSTITUTE OF TECHNOLOGY  
All Rights Reserved



**ARCHIVES**

Signature of Author

\_\_\_\_\_ Department of Chemistry  
May 04, 2010

Certified by

\_\_\_\_\_ Yang Shao-Horn  
Associate Professor  
Mechanical Engineering and Materials Science and Engineering  
Thesis Supervisor

Accepted by

\_\_\_\_\_ Robert W. Field  
Chairman, Departmental Committee on Graduate Students

This Doctoral thesis has been examined by a committee of the Department of Chemistry as follows:

Professor Mounji G. Bawendi

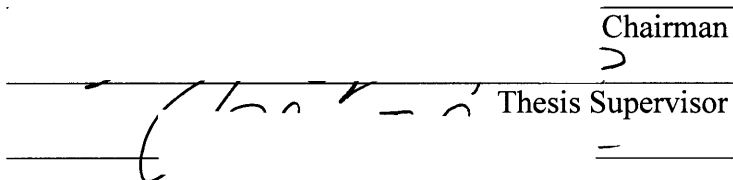
Chairman

Professor Yang Shao-Horn

>

Thesis Supervisor

Professor Sylvia Ceyer

A handwritten signature in black ink, appearing to read 'Yang Shao-Horn', is written across three horizontal lines. The signature starts on the top line, crosses the middle line, and ends on the bottom line. The middle line is labeled 'Thesis Supervisor' on the right side.

# Electrocatalytic Activities of Supported Pt Nanoparticles for Low-Temperature Fuel Cell Applications

## ABSTRACT

Low-temperature fuel cells (FCs) are highly efficient and environmentally friendly energy conversion devices that have been in the spotlight of many energy research efforts in the past few decades. However, FC commercialization is limited by several difficulties, one including the 60 % cell voltage loss caused by the sluggish oxygen reduction reaction (ORR) at the cathode despite the use of the active Pt nanoparticles (NPs) supported on high surface area carbon as the catalyst. In addition, the voltage loss due to the anode reaction kinetics in alkaline FCs (AFCs) remains unknown to the FC society, unlike for the proton exchange membrane fuel cell (PEMFC) case, where the loss due to the anode reaction has been well understood. Moreover, the high surface area carbon used for supporting nanoparticle catalysts is also known to corrode during the FC operation, degrading the cell performance over time. To offer a guideline to develop potential solutions to the above issues, this thesis seeks to explore and develop the fundamental understandings of both the cathode and the anode reaction kinetics for low temperature FCs of both PEMFCs and AFCs, and to demonstrate a new type of catalyst support that is resistant to corrosion.

On the cathode side (the ORR), how the size of the Pt nanoparticle catalyst affect the performance is still under debate. By investigating the ORR on Pt NPs at different sizes and coupling the results to the spectroscopic information, we seek to explore the fundamentals behind the size effect on the ORR activities. We found that below 5 nm, particle size does not play a big role in the catalytic activity. However, the instability of Pt NPs in acidic environment, under simulated operation conditions of a PEMFC, is found to strongly depend on the particle sizes, which is proposed to be due to the Gibbs-Thomson effect. The findings of the particle size effect on the ORR activities and instability suggest that a trade off between smaller NP catalysts, which gives a benefit of a larger mass activity, can suffer from fast degradation. Therefore, a proper NP size that balances between high mass activity and stability would be the best for FC applications according to our study.

On the anode side (the HOR), we found that the reaction kinetics in acid solution on Pt is solely limited by the diffusion of the reactant, and therefore, within the experimental uncertainty, the reaction rate of the HOR in acid is not measurable with conventional rotating disk electrode setup. However, once the same testing configuration is applied to the alkaline solution, the HOR kinetics on Pt electrode are found to be limited by the reaction kinetics, which is in contrast to the case in acid. From this finding,

the anodic overpotential loss in AFCs/AMFCs is projected for the first time and is found to be 1/3 of the ORR loss. This thesis thus highlights the need for development of highly efficient HOR catalysts in alkaline in order to make AFCs/AMFCs more efficient.

Carbon corrosion represents one of the biggest effects that contribute to the performance degradation in FCs. In this work, multi-walled carbon nanotubes (MWCNTs) supported Pt NPs as a novel corrosion-resistant electrocatalyst support for the ORR is proposed as a solution. The Pt/MWCNTs were synthesized through the electrostatic interaction between the Pt precursor and the functionalized MWCNTs, followed by chemical reduction in H<sub>2</sub> at elevated temperatures. Our Pt/MWCNTs catalysts exhibit an enhanced durability after an anodic potential holding, which simulates a typical FC environment during the carbon corrosion. The ORR activity of Pt/MWCNTs is also in agreement with that of the commercial Pt/C. The results indicate that MWCNTs have great potential to serve as a novel carbon-support material with high stability without affecting the Pt catalytic activity.

Thesis Supervisor: Yang Shao-Horn

Title: Associate Professor,

Mechanical Engineering and Materials Science and Engineering

***Dedicated to My Beloved Parents***



## Table of Contents

Title Page.....	1
Signature Page.....	2
Abstract.....	3
Dedication.....	5
Table of Contents.....	7
List of Schemes .....	9
List of Tables.....	10
List of Figures.....	11
Chapter 1: Introduction.....	17
1.1 History of fuel cells.....	17
1.2 Basics of fuel cells.....	20
1.2.1 Thermodynamics of fuel cells.....	20
1.2.2 Kinetics of fuel cells.....	22
1.2.3 Structure of a proton-exchange membrane fuel cell.....	24
1.3 Challenges of fuel cells.....	27
1.4 Open questions.....	30
1.5 Scientific approach.....	31
1.5.1 Photoemission spectroscopy.....	31
1.5.2 Cyclic voltammetry.....	33
1.5.3 Rotating disk electrode.....	35
1.6 Structure of the thesis.....	38
1.7 References.....	40
Chapter 2: Size Effect on the Oxygen Reduction Reaction Activity and Instability of Supported Pt Nanoparticles.....	43
2.1 Introduction.....	43
2.2 Experimental.....	45
2.2.1 Physical Characterization of Pt NP catalysts.....	45
2.2.2 Electrochemical Measurements.....	47
2.3. Results and Discussion.....	50
2.3.1 Size distribution and surface morphology of Pt/C catalysts.....	50
2.3.2 Surface composition and electronic structure of Pt NPs.....	52
2.3.3 Cyclic voltammograms of Pt/C catalysts.....	55
2.3.4 ORR activity as a function of particle sizes.....	58
2.3.5 Surface area loss as a function of particle size upon potential cycling.....	64
2.4 Conclusions.....	67
2.5 References.....	69
Chapter 3: Hydrogen Oxidation and Evolution Reaction Kinetics on Platinum: Acid vs. Alkaline Electrolytes.....	73
3.1 Introduction.....	73
3.2 Experimental.....	76
3.2.1 Electrode Preparation.....	76

3.2.2	Modification of the Reference Electrode.....	76
3.2.3	Electrochemical Measurements.....	77
3.2.4	Impedance Measurements.....	78
3.3	Results.....	79
3.3.1	Measurements of HOR/HER kinetics of Polycrystalline Pt.....	79
3.3.2	Measurements of HOR/HER kinetics of Pt/C.....	86
3.4	Discussion.....	90
3.4.1	Comparing HOR/HER kinetic data with proposed mechanisms in alkaline electrolyte.....	90
3.4.2	Comparing HOR/HER kinetics in Acid with Alkaline Electrolyte.....	94
3.4.3	Predicted Performance of AFCs/AMFCs vs. PEMFCs using Pt/C.....	97
3.5	Conclusions.....	101
3.6	References.....	103
Chapter 4:	Synthesis of Multi-walled Carbon Nanotube Supported Pt Nanoparticles and their Electrocatalytic Activities and Durability.....	107
4.1	Introduction.....	107
4.2	Experimental.....	109
4.2.1	Sample Preparation.....	109
4.2.2	Physical characterization of PtCl <sub>4</sub> <sup>2-</sup> /MWCNTs composite upon heat-treatment.....	110
4.2.3	Electrochemical characterization of Pt NPs/MWCNTs.....	111
4.3	Results and Discussion.....	113
4.4	Conclusions.....	123
4.5	References.....	125
Chapter 5:	Achievements and Perspectives.....	129
5.1	Achievements.....	129
5.2	Perspectives.....	131
5.3	References.....	133
Acknowledgement.....		135
List of Publications.....		137



## List of Schemes

**Scheme 1.1.** Structure of a PEMFC.

**Scheme 1.2.** Schematic of an electrochemical cell and a rotating disk electrode.

**Scheme 4.1.** Synthesis route of MWCNT supported Pt NPs.

## List of Tables

**Table 1.1.** Description of five major types of fuel cells.

**Table 2.1.** The number and volume/area averaged diameters ( $d_n/d_{v/a}$ ) over 200 Pt NP counts from HRTEM measurements for each sample, surface area values of Pt NPs calculated from  $d_{v/a}$  based on  $S^{\text{TEM}} = 6000/(\rho_{\text{Pt}}d_{v/a})^{12}$ , surface area values of Pt NPs from CV measurements, the specific ORR activities and mass activities of Pt NPs in 0.1 M HClO<sub>4</sub> and 0.5 M H<sub>2</sub>SO<sub>4</sub>. The standard deviations are constructed based on at least four repeats of measurements for each sample.

**Table 3.1.** Average HOR/HER exchange current densities ( $i_0$ ) and mass activity ( $i_{0,m}$ ) at  $294 \pm 1.5$  K for Pt(pc) and Pt/C in 0.1 M KOH. Activation energies ( $E_a$ ) were obtained by fitting the data between  $275 \pm 1.5$  K and  $314 \pm 1.5$  K (see Figure 3.4). Data were  $iR$ - and mass-transport corrected as described in the text.

**Table 3.2.** ORR specific activity ( $i_{s,0.9V}$ ) and mass activity ( $i_{m,0.9V}$ ) at 0.9 V vs. RHE, 100 kPa<sub>abs</sub> O<sub>2</sub>, and  $294 \pm 1.5$  K in 0.1 M KOH and 0.1 M HClO<sub>4</sub> for Pt(pc) and Pt/C. Data were obtained from the positive-going scans at 10 mV/s and were  $iR$ - and mass-transport corrected as described in the text.

## List of Figures

**Figure 1.1.** Simulated kinetic current densities of HOR and ORR reactions of a PEMFC running on H<sub>2</sub>-air system and at 80 °C.

**Figure 1.2.** Molecular structure of <sup>®</sup>Nafion.

**Figure 1.3.** Cell voltage loss of a H<sub>2</sub>-air PEMFC operating at 80 °C. Circles: E<sub>cell-i</sub> curve of a H<sub>2</sub>-air PEMFC at 80 °C; squares: E<sub>cell-i</sub> curve after mass and ohmic resistance correction; triangles: E<sub>cell-i</sub> curve after mass correction and diamonds: E<sub>cell-i</sub> after 50% mass correction.

**Figure 1.4.** Energy levels in the solid and the kinetic energy distribution of electrons ejected by photons with photon energy of  $\hbar\nu$ . The x-axis is the density of states.

**Figure 1.5.** Typical cyclic voltammogram of Pt/C in Ar-saturated 0.1 M HClO<sub>4</sub> at a sweep rate of 50 mV/s.

**Figure 1.6.** (a): Typical polarization curves of ORR on carbon supported Pt NPs at 10 mV/s at different rotation rates. Only the negative sweep at 1600 rpm is shown. The inset is the Koutecky-Levich plot obtained at 0.6 V/RHE. (b): Tafel plot with a TS=0.071 V/dec.

**Figure 2.1.** HRTEM images of Pt NPs for (a): Pt-9%; (b): Pt-19%; (c): Pt-46%; (d): Pt-46%-900°C-1m; (e): Pt-46%-900°C-2h; and (f): number-averaged diameters of Pt NPs for each sample. The scale bars are 5 nm. The insets are the Pt particle size distributions, and the indicated sizes are number-averaged ( $d_n$ ) and volume/area-averaged ( $d_{v/a}$ ) particle sizes. The error bars in (f) are standard deviations of the particle size based on at least 200 counts for each sample.

**Figure 2.2.** (a): Representative X-ray photoemission spectra of Pt 4f level for Pt-19% (1.7±0.6 nm) sample. Curve fitting was done after a Shirley-type background subtraction. The Pt 4f peaks were fitted into three sets of Pt species, i.e. Pt<sup>0</sup> (solid red line), Pt(II) (dashed green line) and Pt(IV) (dash-dotted blue line); and (b): the fractions of Pt surface atoms at different oxidation states calculated from the corresponding peak areas of Pt 4f spectra.

**Figure 2.3.** (a): Outer-level photoemission spectra of Pt-19% (1.7±0.6 nm, red square), Pt-46% (2.0±0.6 nm, green circle), Pt-46%-900°C-1m (3.1±0.7 nm, blue triangle), and a high-surface-area carbon sample (black star) collected at a photon energy of 80 eV; (b): subtracted photoemission signals of Pt NPs and Pt foil (grey pentagon); and (c): estimated d band center of Pt 5d emission relative to the Fermi level of different sized

samples based on  $d_{center} = \int N(\varepsilon)\varepsilon d\varepsilon / \int N(\varepsilon)d\varepsilon$ .<sup>21</sup> The error bars of x-axis in (c) are standard deviations of Pt NPs based on at least 200 particle counts for each sample, and the error bars of y-axis in (c) are the total UPS instrumental resolution (0.1 eV).

**Figure 2.4.** CVs of Pt NPs recorded at room temperature and at a sweep rate of 50 mV/s in (a): 0.1 M Ar-saturated HClO<sub>4</sub>; and (c): 0.5 M Ar-saturated H<sub>2</sub>SO<sub>4</sub>; (b): background-corrected charge density associated with Pt-OH formation in the positive sweeps (top) and Pt-OH reduction in the negative sweeps (bottom) in HClO<sub>4</sub>; (d): background-corrected charge density associated with Pt-OH formation (top) and Pt-OH reduction (bottom) in H<sub>2</sub>SO<sub>4</sub>; and (e): OH coverage at 0.9 V on the positive sweeps in HClO<sub>4</sub> and H<sub>2</sub>SO<sub>4</sub>. Error bars are standard deviations constructed from at least four repeats of experiments.

**Figure 2.5.** Representative background-corrected polarization curves of ORR on Pt-46% (2.0±0.6 nm) collected at a sweep rate of 10 mV/s and at room temperature in (a): O<sub>2</sub>-saturated 0.1 M HClO<sub>4</sub> and (c): O<sub>2</sub>-saturated 0.5 M H<sub>2</sub>SO<sub>4</sub>. The rotation rates are 100, 400, 900 and 1600 rpm. Solid lines represent positive-going scans and only negative-going scans at 1600 rpm are shown by the dotted lines. The insets are the Koutecky-Levich plot based on  $\frac{1}{i} = \frac{1}{i_k} + \frac{1}{i_D} = \frac{1}{i_k} + \frac{1}{Bc_0\omega^{1/2}}$  at 0.6 V for HClO<sub>4</sub> and 0.4

V for H<sub>2</sub>SO<sub>4</sub>; background-corrected polarization curves of ORR at a sweep rate of 10 mV/s and at 1600 rpm in (b): O<sub>2</sub>-saturated 0.1 M HClO<sub>4</sub> and (d): O<sub>2</sub>-saturated 0.5 M H<sub>2</sub>SO<sub>4</sub>. The insets are the Tafel plots of these samples obtained from the normalized polarization curves in the positive-going scans at 1600 rpm. Pt loading of 14 μg<sub>Pt</sub>/cm<sup>2</sup> on GCE was used for 4.7±1.2 sample, and Pt loading of ~6.4-7.4 μg<sub>Pt</sub>/cm<sup>2</sup> were used for all the other samples.

**Figure 2.6.** (a): The ORR specific activities at 0.9 V in 0.1 M HClO<sub>4</sub> and 0.5 M H<sub>2</sub>SO<sub>4</sub> as a function of the number-averaged diameter of Pt NPs (d<sub>n</sub>); (b): the ORR mass activities at 0.9 V in 0.1 M HClO<sub>4</sub> and 0.5 M H<sub>2</sub>SO<sub>4</sub> as a function of the number-averaged diameter of Pt NPs (d<sub>n</sub>); (c): the ORR specific activities at 0.9 V in 0.1 M HClO<sub>4</sub> in this work, compared with reference<sup>1</sup> and reference<sup>34</sup> as a function of ESA. Note that the data at 25 °C were calculated from the original data in reference<sup>1</sup> at 60 °C using an activation energy of 10 kJ/mol for the ORR as in reference<sup>39</sup>; and (d): the mass activities at 0.9 V in this work, compared with reference<sup>1</sup> and reference<sup>34</sup> as a function of ESA. The standard deviations in this work were constructed from at least four repeats of experiments.

**Figure 2.7.** Steady-state CVs of (a): Pt-46% (2.0±0.6 nm) and (b): Pt-46%-900°C-1m (3.1±0.7 nm) after every 200 potential cycles. The CVs were recorded at 50 mV/s and at room temperature in 0.5 M N<sub>2</sub>-saturated H<sub>2</sub>SO<sub>4</sub>, after every 200 cycles at 80 °C between 0.6 V and 1.0 V at 20 mV/s. (c): The specific ESA of Pt NPs as a function of the number of potential cycles for Pt-46% (2.0±0.6 nm) and Pt-46%-900°C-1m (3.1±0.7 nm); and (d): normalized specific ESA of the two samples as a function of the number of potential cycles.

**Figure 2.8.** HRTEM images of Pt-46% ( $2.0\pm 0.6$  nm) before (a) and after (b) 1200 cycles between 0.6 V and 1.0 V at 80 °C and at 20 mV/s; HRTEM images of Pt-46%-900°C-1m ( $3.1\pm 0.7$  nm) before (d) and after (e) 1200 cycles; size distributions of Pt NPs before and after potential cycling for Pt-46% ( $2.0\pm 0.6$  nm) (c) and Pt-46%-900°C-1m ( $3.1\pm 0.7$  nm) (f). The indicated sizes are number-averaged particle sizes, and the standard deviations are based on at least 200 counts for each distribution.

**Figure 3.1.** Cyclic voltammograms of Pt(pc) at  $294 \pm 1.5$  K in Ar-saturated 0.1 M KOH at 50 mV/s with two different positive potential limits. The current density is referenced to the actual Pt surface area.

**Figure 3.2.** (a) HOR/HER polarization curves (positive-going scans) on Pt(pc) at different rotation rates at  $294 \pm 1.5$  K. The inset shows a Koutecky-Levich plot at 0.5 V/RHE. (b) HOR/HER polarization curves on Pt(pc) at 1600 rpm at different temperatures (positive-going scans). The data were collected in H<sub>2</sub>-saturated 0.1 M KOH at 10 mV/s.

**Figure 3.3.** HOR/HER measured kinetic current densities (grey solid line) on Pt(pc) in 0.1 M KOH at 10 mV/s and their fit to the Butler-Volmer equation (see Eq. 3.2) with  $\alpha = 0.5$  (dashed black line): (a) at 275 K; (b) at 314 K. The HOR/HER kinetic current densities were obtained from *iR*-corrected polarization curves and are corrected for hydrogen mass transport in the HOR branch using Eq. 3.1. The corresponding insets show the HOR/HER polarization curves before (solid black line) and after (dashed red line) *iR* correction.

**Figure 3.4.** Representative Arrhenius plots of the HOR/HER exchange current densities on Pt(pc) (black squares) and Pt/C (red circles) in 0.1 M KOH. The calculated HOR/HER activation energies,  $E_a$ , are  $28.9 \pm 4.3$  kJ/mol for Pt(pc) and  $29.5 \pm 4.0$  kJ/mol for Pt/C based on four and two sets of repeat measurements, respectively.

**Figure 3.5.** Cyclic voltammograms of Pt/C at  $294 \pm 1.5$  K in Ar-saturated 0.1 M KOH at 50mV/s with two different positive potential limits. The current density is referenced to the actual Pt surface area.

**Figure 3.6.** HOR/HER measured kinetic current densities (grey solid line) on Pt/C in 0.1 M KOH at 10 mV/s and their fit to the Butler-Volmer equation (see Eq. 3.2) with  $\alpha = 0.5$  (dashed black line): (a) at 275 K; (b) at 314 K. The HOR/HER kinetic current densities were obtained from *iR*-corrected polarization curves and are corrected for hydrogen mass transport in the HOR branch using Eq. 3.1. The corresponding insets show the HOR/HER polarization curves before (solid black line) and after (dashed red line) *iR* correction.

**Figure 3.7.** (a) HOR/HER polarization curve on Pt(pc) in 0.1 M HClO<sub>4</sub> at 1600 rpm before ( $E_{RDE}$ , solid black line) and after ( $E_{iR-free}$ , dotted red line) *iR*-correction. The

inset is the Koutecky-Levich plot obtained at  $E=0.1$  V/RHE for the HOR at different rotation rates. (b) HOR/HER polarization curve on Pt(pc) in 0.1 M KOH at 1600 rpm before ( $E_{RDE}$ , solid black line) and after ( $E_{iR-free}$ , dotted red line)  $iR$ -correction; the dashed black line is the Nernstian diffusion overpotential calculated according to Eq. 3.12. The data are shown for the positive-going scans at 10 mV/s at a temperature of  $294 \pm 1.5$  K. Note that the x-axis potential range in (b) is double of that in (a).

**Figure 3.8.** (a) HOR/HER specific exchange current density of Pt/C in a PEM fuel cell at 353 K and 101 kPa<sub>abs</sub> H<sub>2</sub> (solid circle, from reference<sup>12</sup>) compared to that obtained in 0.1 KOH in this study (solid squares) and extrapolated to 353 K (open square). (b) Projected HOR overpotential vs. Pt mass activity in KOH based either on 62 m<sup>2</sup>/g<sub>Pt</sub> for the 46%wt. Pt/C catalyst used in this study (black solid line) or on 92 m<sup>2</sup>/g<sub>Pt</sub> for the 5%wt. Pt/C catalyst used in reference<sup>12</sup> (grey dashed line); this is compared with mass activities measured on 5%wt. Pt/C in a PEMFC at 353 K (red line, from reference<sup>12</sup>).

**Figure 4.1.** Representative XPS spectra of PtCl<sub>4</sub><sup>2-</sup>/MWCNTs composites for (a): carbon 1s; and (b): Pt 4f. Curve-fitting has been made according to reference<sup>29</sup> after a Shirley-type background subtraction, and all spectra have been calibrated to SP<sup>2</sup> hybrid carbon at 284.5 eV.

**Figure 4.2.** (a): Change of atomic ratio between Pt and C with the pH of suspensions containing PtCl<sub>4</sub><sup>2-</sup> and NH<sub>2</sub>-MWCNTs. The concentration of PtCl<sub>4</sub><sup>2-</sup> is fixed at 5 mM. (b): Simulated fraction of protonated amines among the total amine functional groups at different pH based on  $pK_a = pH - \log \frac{NH_2}{NH_3^+}$ , assuming that amine functionalized MWCNTs have a same  $pK_a$  (6.9) as that of NH<sub>2</sub>(CH<sub>2</sub>)<sub>2</sub>NH<sub>2</sub>.

**Figure 4.3.** Change of atomic ratio between Pt and C with the concentration of PtCl<sub>4</sub><sup>2-</sup> in suspensions. The pH of the suspensions is about 3.5.

**Figure 4.4.** Weight change of PtCl<sub>4</sub><sup>2-</sup>/MWCNTs upon heat-treatment in H<sub>2</sub>. The sweep rate is 5 °C/minute.

**Figure 4.5.** XPS spectra of PtCl<sub>4</sub><sup>2-</sup>/MWCNTs composites upon heat-treatment for (a): Pt 4f; and (b): Cl 2p.

**Figure 4.6.** HRTEM images of Pt/MWCNTs formed by heat-treatment of PtCl<sub>4</sub><sup>2-</sup>/MWCNTs in H<sub>2</sub> atmosphere at (a): 300 °C; (b): 400 °C; (c): 500 °C and (d): 600 °C.

**Figure 4.7.** Cyclic voltammograms collected in Ar-saturated 0.1 M HClO<sub>4</sub> upon potential holding at 1.5 V/RHE for (a): Pt/MWCNTs; and (b): Pt/C. The scanning rate is 50 mV/s. (c): Normalized electrochemical surface area of Pt/MWCNTs and Pt/C upon potential holding; and (d): normalized double-layer currents at 0.6 V/RHE of Pt/MWCNTs and Pt/C upon potential holding.

**Figure 4.8.** HRTEM images of (a): Pt/C and (b): Pt/MWCNTs after potential holding

at 1.5 V/RHE for 36 hours.

**Figure 4.9.** (a): Representative ORR polarization curves of Pt/MWCNTs in O<sub>2</sub>-saturated 0.1 M HClO<sub>4</sub> at different rotating speeds. The inset is the Koutecky-Levich plot obtained at 0.6 V/RHE; and (b): specific ORR activities at 0.9 V and 0.85 V of Pt/MWCNTs treated at different temperatures, compared with those of Pt/C.





# Chapter 1

## Introduction

### 1.1 History of fuel cells

Fuel cells, as highly efficient and environmentally friendly energy conversion devices, have been in the spotlight of the energy research in the last few decades. Their origin can be dated back to the 19<sup>th</sup> century, when Christian F. Schönbein first discovered in 1838 that, once connected by electrodes, hydrogen and oxygen or chlorine could react to generate electricity<sup>1</sup>, which he termed as the “polarization effect”. Shortly afterwards, William R. Grove invented a “gas voltaic battery”<sup>2</sup>, which drew a current between the two Pt strips, one in hydrogen and another in oxygen in two separated bottles filled with sulfuric acid. While this invention has now been recognized as the “First” fuel cell, yet the concept or the term of “fuel cell” was not proposed until 1889 by Ludwig Mond and Charles Langer<sup>3</sup>, who attempted to construct the first practical fuel cell device using industrial coal gas as the fuel and air as the oxidant. At that time, they realized that increasing the surface area of Pt would enhance the current. Thus, they started to use Pt black as the electrodes and fabricated a cell that produced 6 A/ft<sup>2</sup> at 0.73 V output voltage. However, the lack of understanding of fuel cell principles and the dependence on expensive and unreliable fuel resources as well as the Pt requirement made it impossible to commercialize the technology at that time. In addition, the exploitation and utilization of fossil fuels and the emergence of internal combustion engine in the late 19<sup>th</sup> century offered a more economically viable source of energy over fuel cells. As a result, the idea

of fuel cell commercialization slowly disappeared and the research on fuel cells continued only on the laboratory scale and attracted mainly scientists' interests. Despite the lack of commercial interest, new inventions were still being reported continually during this period. For example, in 1932, Francis Bacon modified the structure of the device built by Mond and Langer and produced the very first alkaline fuel cell by utilizing alkaline electrolytes and nickel electrodes<sup>4</sup>. It was not until the 1950's that the fuel cell began to receive commercial attention again when General Electric (GE) produced the first proton exchange membrane fuel cells (PEMFCs), which were chosen by NASA for the Gemini and Apollo space projects.<sup>5</sup> However, despite the renewed public attention on the technology, the initial success of PEMFC, which contained sulphonated polystyrene ion-exchange membrane electrolyte with Pt deposited on top, was limited to just space applications due to the cost issue of PEMFC.

As human activities have involved more and more energy consumption in the past two decades, the release of greenhouse gases following the uses of fossil fuels such as carbon dioxide has increased dramatically. Despite of the tremendous consumption of fossil fuels, the energy need is still projected to grow even further, and thus human beings are facing an increasingly severe energy shortage crisis. To maintain sustainable development for the future generations, many nations and organizations have contributed numerous efforts to employ renewable energy resources such as wind, solar, hydropower, geothermal, and biofuels, etc. Among the alternative energy conversion devices, fuel cells offer one of the highest efficiency with minimum green-house gas emission, and have become alternative solutions for sustainable development.<sup>6</sup>

Based on the types of the electrolytes and charge carriers, fuel cells can be categorized into five major types: proton exchange membrane fuel cells (PEMFCs), phosphoric acid fuel cells (PAFCs), alkaline fuel cells (AFCs), molten carbonate fuel cells (MCFCs) and solid oxide fuel cells (SOFCs). PEMFCs can be further divided into two types based on the fuel: H<sub>2</sub>-O<sub>2</sub> PEMFCs and direct methanol FCs. Table 1.1 provides the technical characteristics of different types of FCs. The low-temperature FCs typically have a compact size and light weight, do not generate pollutants such as NO<sub>x</sub>, and thus are appropriate for portable and automotive applications. However, low-temperature FCs have to utilize noble metals such as Pt as the catalyst to facilitate the reaction, and thus their commercialization is constrained by the supply of the noble metals. The high-temperature FCs on the other hand, such as MCFCs and SOFCs, do not require the noble metal catalysts but instead require a complex component to recover the heat generated for steam reforming, and consequently they generally occupy much larger spaces and are more suitable for large-scale power plants.<sup>6,7</sup>

**Table 1.1.** Description of five major types of fuel cells.

	PEMFC	PAFC	AFC	MCFC	SOFC
Electrolyte	Polymer membrane	Liquid H <sub>3</sub> PO <sub>4</sub>	Liquid KOH	Molten carbonate	Ceramic
Charge carrier	H <sup>+</sup>	H <sup>+</sup>	OH <sup>-</sup>	CO <sub>3</sub> <sup>2-</sup>	O <sup>2-</sup>
Operating temperature	80°C	200°C	60-220°C	650°C	600-1000°C
Catalyst	Platinum	Platinum	Platinum	Nickel	Perovskites (ceramic)
Cell components	Carbon based	Carbon based	Carbon based	Stainless based	Ceramic based
Fuel compatibility	H <sub>2</sub> , methanol	H <sub>2</sub>	H <sub>2</sub>	H <sub>2</sub> , CH <sub>4</sub>	H <sub>2</sub> , CH <sub>4</sub> , CO

## 1.2 Basics of fuel cells

### 1.2.1 Thermodynamics of fuel cells

Unlike a combustion engine, whose energy conversion is limited by the Carnot cycle such that the efficiency can be defined by  $\eta = \frac{T_H - T_L}{T_H}$ , where a large fraction of energy is wasted in the form of heat, fuel cells directly convert chemical energy into electricity, which thermodynamically is instead limited by the ratio of  $\frac{\Delta G(r)}{\Delta H(r)}$ , where  $\Delta G(r)$  is the Gibbs free energy and  $\Delta H(r)$  is the total enthalpy change of a chemical reaction (r)<sup>6, 8</sup>. Taking a H<sub>2</sub>-O<sub>2</sub> based PEMFC as an example, the overall reaction is



$\Delta G(r)$  of this reaction is -237 kJ/mol and  $\Delta H(r)$  is -287 kJ/mol at standard conditions, i.e., 298.15 K, 1 atm of  $P_{\text{H}_2}$  and 1 atm of  $P_{\text{O}_2}$ . At these conditions, the conversion efficiency is about 83%, which is much higher than most of the other energy conversion devices. Under constant temperature and constant pressure conditions, the Gibbs free energy of a reaction can be converted into the electric work based on the following equation:

$$\varepsilon(r) = -\frac{\Delta G(r)}{nF} \quad [1.2]$$

where n is the moles of electrons transferred and F, equal to 96485 C/mol, is the Faraday constant. From the data given above, the cell voltage of a H<sub>2</sub>-O<sub>2</sub> based PEMFC at 298.15 K, 1 atm of  $P_{\text{H}_2}$  and 1 atm of  $P_{\text{O}_2}$ , is therefore  $E^0 = 1.23 \text{ V}$ . The variance of the cell

voltage with temperature can be estimated from the following equation assuming temperature-independent  $\Delta H$  and  $\Delta S$ :

$$\varepsilon(r)_T = \varepsilon^0 + \frac{\Delta S}{nF}(T - T_0) \quad [1.3]$$

where  $\varepsilon(r)_T$  represents the temperature-dependent cell voltage. For a H<sub>2</sub>-O<sub>2</sub> PEMFC operated at 80 °C, the cell voltage is decreased to 1.18 V, where  $\Delta S$  is -163 J/mol/K for the overall reaction.

From the thermodynamics of a reaction, the activities of reactants and products affect the Gibbs free energy in such a way that:

$$\Delta G(r) = \Delta G^0 + RT \ln \frac{\prod_i a_{i,prod}^{\nu_i}}{\prod_j a_{j,react}^{\nu_j}} \quad [1.4]$$

For H<sub>2</sub> +  $\frac{1}{2}$ O<sub>2</sub> → H<sub>2</sub>O , the resulting activity-dependent cell voltage under standard conditions thus becomes

$$\varepsilon(r)_a = \varepsilon^0 - \frac{RT}{nF} \ln \frac{a_{H_2O}}{a_{H_2} a_{O_2}^{1/2}} = \varepsilon^0 + \frac{RT}{nF} \ln \left( \frac{P_{H_2}}{P^0} \right) \left( \frac{P_{O_2}}{P^0} \right)^{1/2} \quad [1.5]$$

where  $\varepsilon(r)_a$  represents the activity-dependent cell voltage at the temperature of 298.15 K and  $P^0$  denotes the standard ambient pressure, i.e., 101.3 KPa. Combining the temperature-dependence and activity-dependence of the cell voltage, for a PEMFC running at any temperature and any partial pressures of H<sub>2</sub> and O<sub>2</sub>, the cell voltage can be written as

$$\varepsilon(r) = \varepsilon^0 + \frac{\Delta S}{nF}(T - T_0) + \frac{RT}{nF} \ln \left( \frac{P_{H_2}}{P^0} \right) \left( \frac{P_{O_2}}{P^0} \right)^{1/2} \quad [1.6]$$

### **1.2.2 Kinetics of fuel cells**

The kinetics of an electrochemical reaction can be described using the Butler-Volmer equation:

$$i = i_0 \left[ \exp\left(\frac{\alpha n F}{RT} \eta\right) - \exp\left(\frac{-\beta n F}{RT} \eta\right) \right] \quad [1.7]$$

where  $i_0$  is the exchange current density of an electrochemical reaction at its reversible potential on a certain surface;  $\alpha$  and  $\beta$  are the transfer coefficients;  $n$  is the number transferred; and  $\eta$  is the overpotential  $\varepsilon - \varepsilon^0$ , which is the extra potential applied to the reversible potential<sup>6, 8</sup>. Because other parameters such as  $RT$  and  $F$  are constants and have their conventional definitions, the Butler-Volmer equation can be simplified to the following:

$$i = i_0 \left[ 10^{\frac{\eta}{a}} - 10^{-\frac{\eta}{b}} \right] \quad [1.8]$$

where  $a$  and  $b$  are so-called Tafel slopes (TS) and equal to  $\frac{2.303RT}{\alpha n F}$  and  $\frac{2.303RT}{\beta n F}$ , respectively. The first term in the brackets of Eq. [1.8] represents the kinetics of the forward reaction (oxidation reaction) while the second term represents the backward reaction (reduction reaction) kinetics. Depending on the sign and the magnitude of the applied overpotential, one of the reaction directions can be favored. For example, with a positive overpotential, the reaction will proceed in the oxidation direction (first term), and vice versa. Generally, if the positive overpotential is large enough (half of the TS) such that the second term will become 10% of the first term, the equation can be further simplified to contain just the dominant term (first term, in this case) only.

Figure 1.1 demonstrates a simulated kinetic current–voltage relation of reactions on the two electrodes of a PEMFC running at 80 °C using the Butler-Volmer equation. Note that air is used at the cathode, thus the theoretical potential of the cathode is 1.169 V vs. reversible hydrogen electrode (RHE) (dashed blue in Figure 1.1). The theoretical potential of the anode is 0 V vs. RHE (dashed blue). Ideally, the output cell voltage will be 1.169 V regardless of the current density extracted from the cell. However, due to the different exchange current densities, ORR and HOR exhibit different behaviors based on the Butler-Volmer equation mentioned above. Because of the very fast kinetics of the HOR, almost no overpotential (<20mV) is needed to drive 1.5 A/cm<sup>2</sup> (a typical operating current of PEMFCs). On the contrary, the ORR is more sluggish, where the exchange current density is extremely small, on the order of  $\sim 10^{-8}$  A/cm<sup>2</sup><sub>Pt</sub>, and therefore an overpotential as large as 300 mV has to be applied even on the most active Pt-based catalysts.

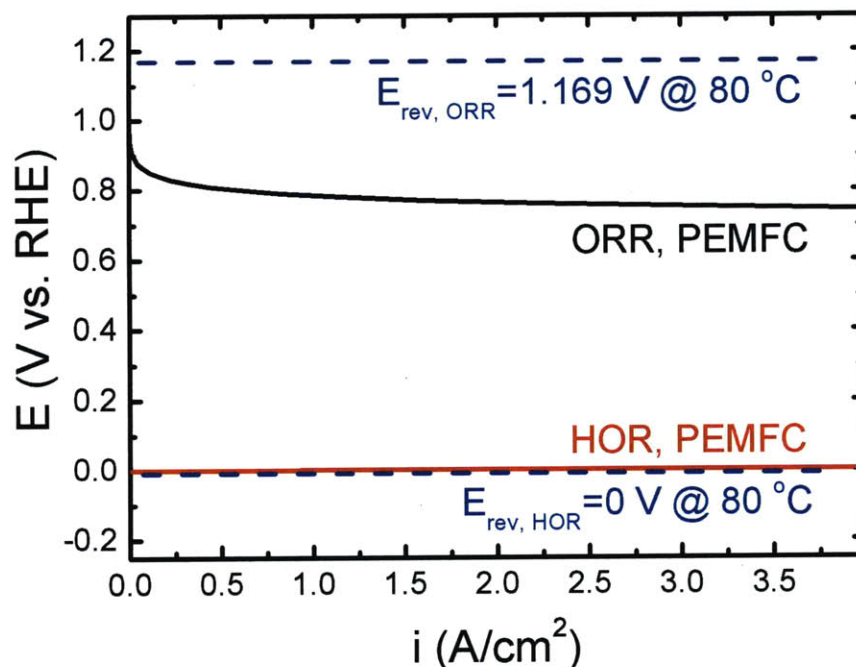


**Figure 1.1.** Simulated kinetic current densities of HOR and ORR reactions of a PEMFC running on H<sub>2</sub>-air system and at 80 °C.

### **1.2.3 Structure of a proton-exchange membrane fuel cell**

Scheme 1.1 represents a typical structure of a H<sub>2</sub>-O<sub>2</sub> based PEMFC, which consists of three major components, i.e. the cathode, the anode, and the proton-exchange membrane.<sup>7</sup> The membrane is generally sandwiched between the cathode and the anode. To facilitate the electrochemical reaction at the interfaces between the membrane and the cathode/anode, a catalyst layer is used. On each catalyst layer, Pt serves as the catalysts for both reactions. At the anode, H<sub>2</sub> splits into protons, generating a pair of electrons on Pt surfaces. Driven by the potential difference between the cathode and the anode, electrons generated at the anode are transferred through the outer circuit to reduce the O<sub>2</sub> at the cathode. Simultaneously, the protons diffuse across the membrane to the catalyst



layer of the cathode, combine with reduced  $O_2$ , and generate water. Nafion<sup>®</sup>, developed by Dupont, is the most commonly used proton-conducting membrane, which consists of a tetrafluoroethylene backbone with perfluorovinyl ether side groups terminated by sulfonate moieties (Figure 1.2). In this material, proton transport is believed to occur via the hopping mechanism along the sulphonated groups. Meanwhile, the membrane physically separates the anode and cathode and blocks the pathway for electron transfer, so that no short-circuit recombination of electrons and protons happens. Because the electrochemical reactions are proportional to the surface area of the catalyst, the current is therefore directly related to the catalyst's surface area. To maximize the surface area while minimizing the catalyst's cost, Pt nanoparticles (NPs) with high surface-volume ratio are utilized as the catalysts. However, these Pt NPs generally suffer from aggregation due to the large surface energy of the NPs, which led to a decrease the surface area over time. To prevent the aggregation of Pt NPs, high-surface-area carbon is used as the support for two reasons: to disperse and stabilize Pt NPs, and to provide a high electron conductivity channel between the catalysts and the current collector. The combination of the cathode, the anode, and the membrane is sandwiched again between two gas diffusion layers; together they constitute the so-called membrane electrode assembly (MEA). The gas diffusion layers are made of highly porous carbon cloth or paper to provide a pathway for gas delivery. Outermost are two graphite plates with engraved gas channels, serving as the gas inlets and current collectors.

**Scheme 1.1.** Structure of a PEMFC.

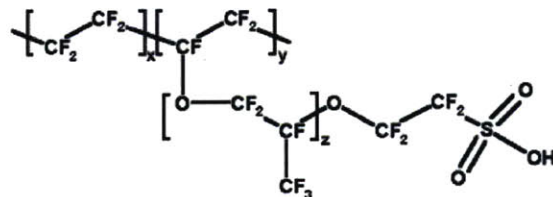
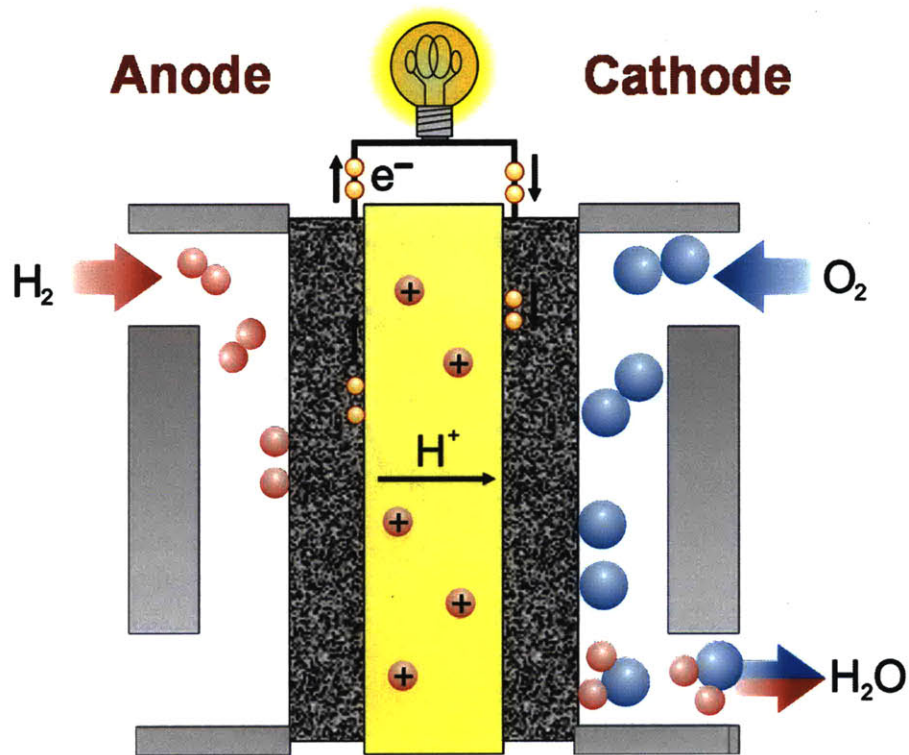
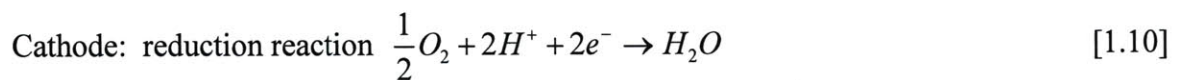
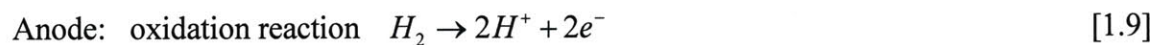


**Figure 1.2.** Molecular structure of <sup>®</sup>Nafion.

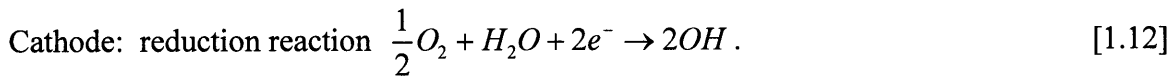
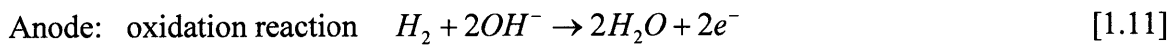
The reactions at the anode and cathode of a H<sub>2</sub>-O<sub>2</sub> based PEMFC are:



The overall cell voltage is 1.229 V at 298.15 K and at 101.3 KPa of H<sub>2</sub> and O<sub>2</sub>, which is calculated from the potential difference between the cathode and the anode. Herein, the

potential of the oxidation reaction at the anode, namely the standard hydrogen electrode (298.15 K,  $P_{H_2} = 101.3 \text{ KPa}$ ) is defined to be 0 V and, for comparison, the potential of the other half cell reactions will be constructed based on this reference. For example, with respect to the hydrogen electrode, the oxygen reduction reaction has a standard potential of 1.229 at 298.15 K and 101.3 KPa.

For an alkaline fuel cell, the reactions at each electrode instead become:



The difference between the PEMFC and the alkaline fuel cell is the use of an anion-conducting membrane instead of the proton-conducting one, which provides a conductive pathway for OH<sup>-</sup> groups.

### 1.3 Challenges of fuel cells

Despite the thermodynamic cell voltage of 1.18 V (at 80 °C), H<sub>2</sub>-O<sub>2</sub> based FCs can never achieve this value due to many potential losses during the operation such as the mass transport loss and the ohmic loss as well as the ORR kinetic loss. Figure 1.3 shows the distribution of these losses in a PEMFC, which highlights the important fact that the ORR kinetic loss accounts for about 70% of the total loss<sup>9</sup>. Note that Figure 1.3 shows a H<sub>2</sub>-Air cell, so the theoretical value is slightly decreased to 1.169 V.

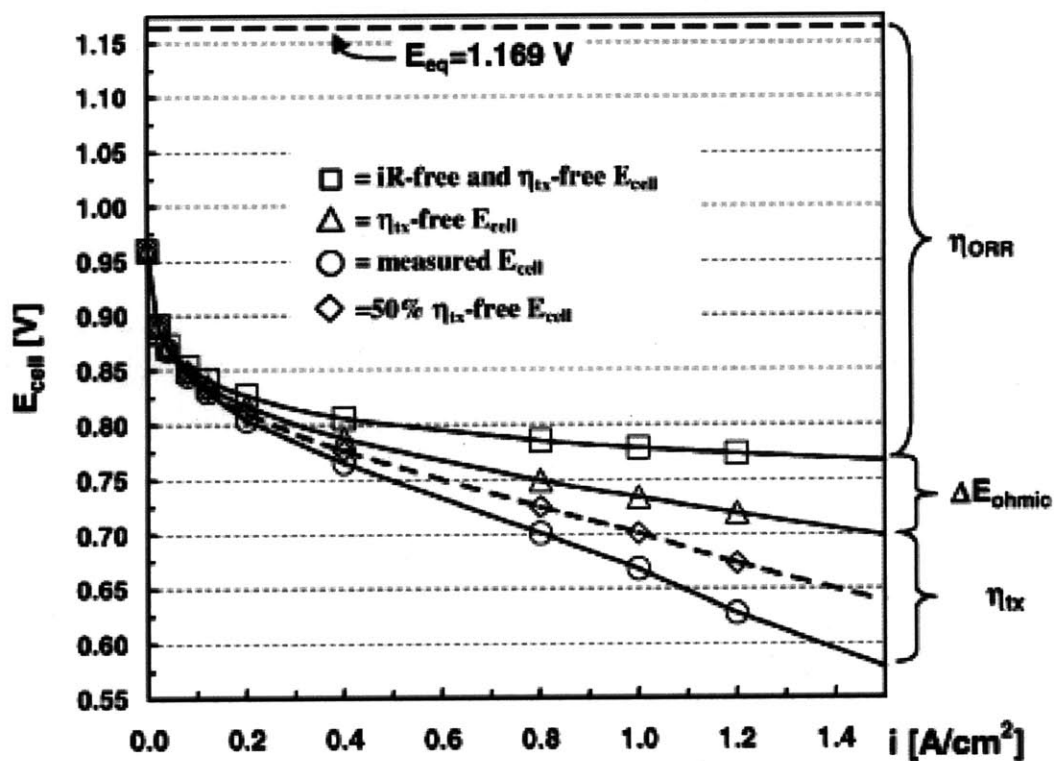


**Figure 1.3.** Cell voltage loss of a H<sub>2</sub>-air PEMFC operating at 80 °C. Circles:  $E_{\text{cell}}$ - $i$  curve of a H<sub>2</sub>-air PEMFC at 80 °C; squares:  $E_{\text{cell}}$ - $i$  curve after mass and ohmic resistance correction; triangles:  $E_{\text{cell}}$ - $i$  curve after mass correction and diamonds:  $E_{\text{cell}}$ - $i$  after 50% mass correction.<sup>9</sup>

Despite the use of the state-of-the-art Pt/C catalyst, the ORR overpotential is still very large; in addition, the reliance on the noble metal catalysts greatly inhibits the commercialization of PEMFCs and alkaline fuel cells<sup>10</sup>. Therefore more active Pt-based catalysts or non-precious metal catalysts for the ORR need to be developed to minimize the usage of Pt electrocatalysts. One strategy of boosting the electrocatalytic activity of the Pt-based catalyst is to alloy in transition metal to develop a more effective PtM alloy catalyst. For the alloyed PtM catalysts, judging from the current economical analysis of the Pt cost, at least 10-fold enhancement of the ORR activity must be achieved for the

fuel cell commercialization. Recent studies<sup>11</sup> on Pt<sub>3</sub>Ni (111) single crystals has shown that such a 10x improvement of the ORR is indeed possible and this finding has led to a recent work of Pt(111)-enriched Pt<sub>3</sub>Ni nanoparticles for highly active ORR NP catalysts<sup>12</sup>. Another strategy is to develop non-precious metal catalysts with an ORR activity comparable to the Pt NPs. Recently, a non-precious metal containing catalyst involving nitrogen-coordinated Fe ions with a comparable ORR activity to Pt has been developed for the ORR in both acid and alkaline<sup>13, 14</sup>, offering an alternative route to lower the fuel cell's cost. However, despite these developments, the greatest source of inefficiency of H<sub>2</sub>-O<sub>2</sub> fuel cells still lies in the sluggish ORR kinetics.

Another important issue that is relevant to the commercialization of fuel cells is stability. To offer a reliable power generator for portable devices and automotives applications, fuel cells have to meet the present DOE lifetime target of 5000 hours<sup>15</sup>, which to date, has not been achieved. The complexity of the degradation problem lies in the fact that many factors cause the fuel cell degradation, which can be quantified using the cell voltage drops over time. These factors include 1) the total surface area loss of Pt catalyst at the cathode due to mass loss of Pt and Ostwald-ripening of Pt NPs<sup>16</sup>; 2) chemical degradation of the membrane due to the decomposition of the polymer chain caused by the attack from the radicals generated during the fuel cell reactions<sup>17, 18</sup>; and 3) "cathode-thinning" caused by carbon support corrosion when PEMFCs experience localized H<sub>2</sub> starvation or the start-up/shut-down cycles<sup>19, 20</sup>. The latter phenomenon results in the loss of the cathode void volume, which compromises the mass transport of the reactants, and eventually the cell performance. Advanced metal catalysts with excellent ORR catalytic activities and resistance towards dissolution as well as new types

of corrosion-resistant carbon supports are needed to resolve the stability issue of fuel cells.

#### **1.4 Open questions**

Although the particle size effect of Pt (i.e. the activities of Pt catalysts at smaller sizes vs. bulk) on the ORR activities has been studied extensively, the conclusions are still under debate. Previously, it has been postulated that the unique surface structure of the Pt NPs can cause the ORR activity to decrease<sup>21</sup>. The first open question is whether there is a correlation between the surface structure of a series of Pt NPs at different sizes and the ORR activity.

The second open question lies in the performance comparison between PEMFCs and alkaline fuel cells. Previous studies<sup>10, 22</sup> have shown that Pt NPs have very similar ORR activities in either acid or alkaline electrolytes, which suggests a very similar cathodic overpotential in an alkaline fuel cell and a PEMFC. The HOR on Pt/C on the anode side, however, has seldom been studied. Often, the HOR overpotential on Pt/C in an alkaline fuel cell was extrapolated from the measurement in acid electrolytes. The second open question is whether the performance of the anode between the two systems is truly identical. The kinetic information of the HOR in an alkaline solution will provide a better understanding of the difference between the acid and the alkaline electrolytes and offer an important insight to the development of alkaline fuel cells.

The third open question is whether a development of a corrosion-resistant carbon using a more stable form of carbon nanomaterials is possible. A more corrosion-resistant catalyst support has to be developed to maintain a long-term operation of fuel cells. One

possible strategy to develop such a support is to use a material known as carbon nanotubes (CNTs). CNTs are examples of corrosion-resistant carbon nanomaterials. Owing to their highly graphitized structure with minimal defects such as O-terminated carbon, a moiety commonly found in a typical carbon support, CNTs offer a promising approach to address the corrosion issue. In this work, we will address whether such a material would truly serve as a more stable support or not.

### **1.5 Scientific approach**

The ORR and HOR kinetics in aqueous electrolytes on polycrystalline Pt disk and high surface area carbon supported Pt NPs with different sizes are investigated for the first two open questions. For the third open question, multi-walled carbon nanotube (MWCNTs) supported Pt nanoparticles will be synthesized and the durability of Pt/MWCNTs will be compared to Pt/C. The electrochemical surface area of the Pt electrodes is determined by the cyclic voltammograms, and the ORR and HOR activities on Pt electrodes are measured using the rotation disk electrode (RDE) method. Ultra-violet photoemission and X-ray photoemission spectroscopy were performed to examine the surface electronic structure and surface compositions of these Pt NPs, which will be correlated to the ORR activities.

#### **1.5.1 Photoemission spectroscopy**

Photoemission spectroscopy explores the surface electronic structure, specifically the density of states, which can be used to extrapolate the elemental compositions of studied substances. Based on the principle of the photoelectric effect, when a substance

is exposed to a light source, the electrons from the substance will be ejected with a kinetic energy of  $E_k$ , which is determined by the photon energy  $\hbar\nu$ , the work function  $\phi$  and the binding energy  $BE$  of the electron at its initial state using the following equation:

$$E_k = \hbar\nu - (BE + \phi) \quad [1.13]$$

Since each state of an element has a characteristic binding energy, the observed binding energy from the photoemission spectrum is typically used for chemical identification. Since the photon-ejected electrons have a limited escape depth with only a few surface layers of atoms, the photoemission spectroscopy can only measure the ejected electrons from those few layers and thus is a surface-sensitive technique. While the ultraviolet-photoemission spectroscopy and the X-ray photoemission spectroscopy are very similar in principle, they use very different photon energy. Thus, one is more suitable for the detection of the valence states, and another for the core levels. Figure 1.4 is the energy diagram of the photoemission spectroscopy, showing the relation between the observed kinetic energy and the binding energy of a material.<sup>23</sup>



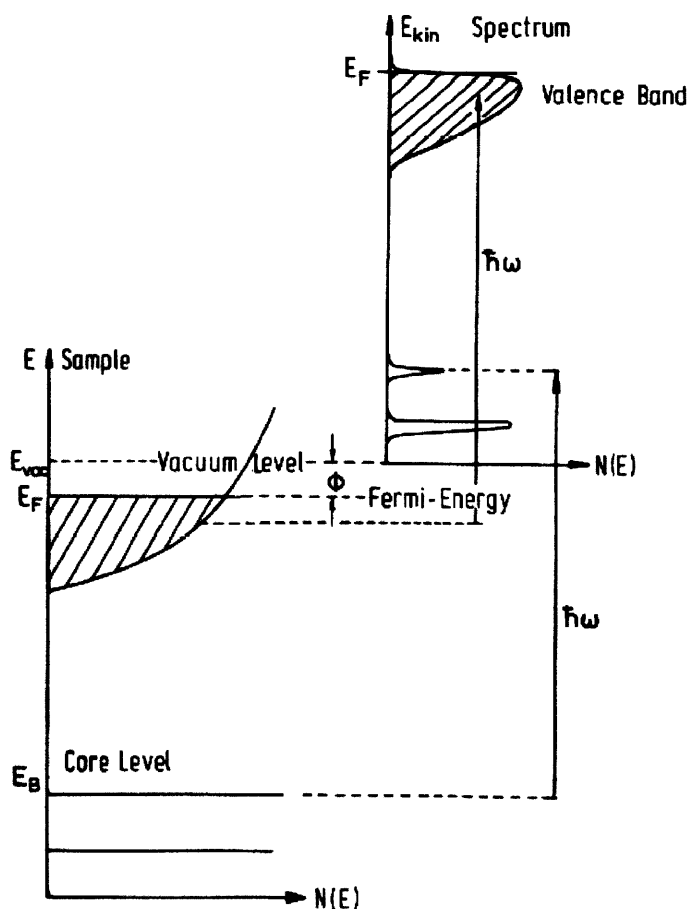


**Figure 1.4.** Energy levels in the solid and the kinetic energy distribution of electrons ejected by photons with photon energy of  $\hbar\nu$ . The x-axis is the density of states.<sup>23</sup>

### 1.5.2 Cyclic voltammetry

Cyclic voltammetry is a type of potential-controlled electrochemical techniques, which is often used to examine the electrode's electrochemical properties.<sup>8, 24</sup> The potential of the working electrode is swept linearly with time and cycled between two potential ends. By adjusting the potential of the working electrode, electrons are transferred between the electrode and the molecules in the electrolyte. Figure 1.5 is a typical CV of Pt/C collected in Ar-saturated 0.1 M HClO<sub>4</sub> at a sweep rate of 50 mV/s,

which records the current response of the working electrode when the potential is scanned from 0.05 V to 1.1 V vs. RHE (forward scan) and swept back from 1.1 V to ~0.5 V vs. RHE (backward scan). The currents above 0  $\mu\text{A}$  are conventionally defined as the oxidation current and the currents below 0  $\mu\text{A}$  represent reduction current. The CV can be divided into three regions: H underpotential deposition region (~0.05 V-0.4 V vs. RHE), double layer region (~0.4-0.7 V vs. RHE) and Pt oxide formation region (above 0.7 V vs. RHE). On the forward scan (from ~0.05 to 0.4 V vs. RHE), as the potential increases, pre-adsorbed H atoms on Pt surface are oxidized to  $\text{H}^+$  and desorb from Pt surface and diffuse into the electrolyte; as the potential goes into the high potential window (above 0.7 V vs. RHE),  $\text{H}_2\text{O}$  starts to adsorb and dissociate on Pt surface, forming Pt-OH and continue to form Pt oxides as the potential increases. On the backward scan, as the potential decreases, Pt-OH or Pt oxide is being reduced. When the potential is decreased to 0.4 V vs. RHE, the protons from the electrolyte will adsorb on Pt surface and be reduced, known as H under potential deposition. In the potential window of ~0.4 V-0.7 V, the Pt surface is free of H or OH/O, and the current is mainly a contribution of the double layer capacitance (anion adsorption such as  $\text{ClO}_4^-$ ). Due to the large surface area of the carbon support, the double layer capacitive current can also take place on carbon. After subtraction of the capacitive current, which is assumed to be a horizontal line as in the ideal case, the charges in the H desorption or adsorption region are integrated to generate the number of adsorbed H atoms. The total electrochemical surface area (ESA) of Pt can be determined using an electric charge density of 210  $\mu\text{C}/\text{cm}^2_{\text{Pt}}$ . Knowing the weight of Pt loaded on the electrode, the specific ESA in unit of  $\text{m}^2/\text{g}_{\text{Pt}}$ , known as the NP dispersion, can be obtained.

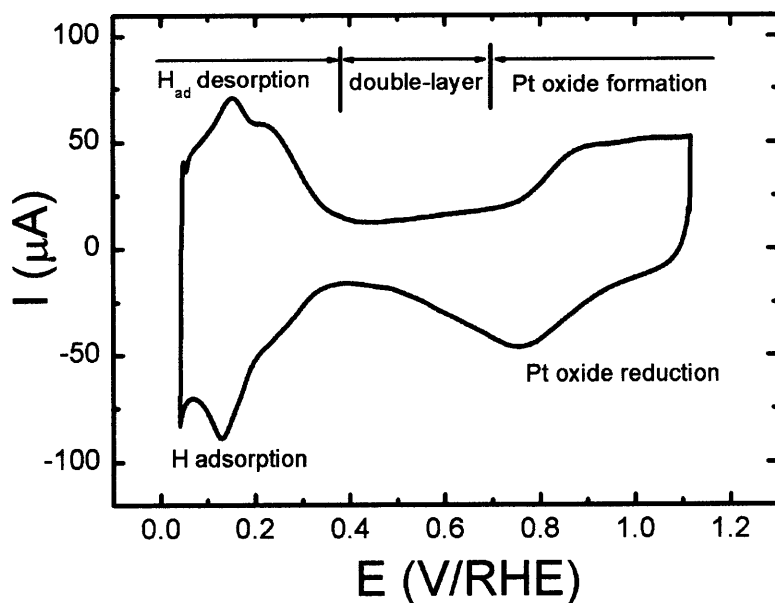
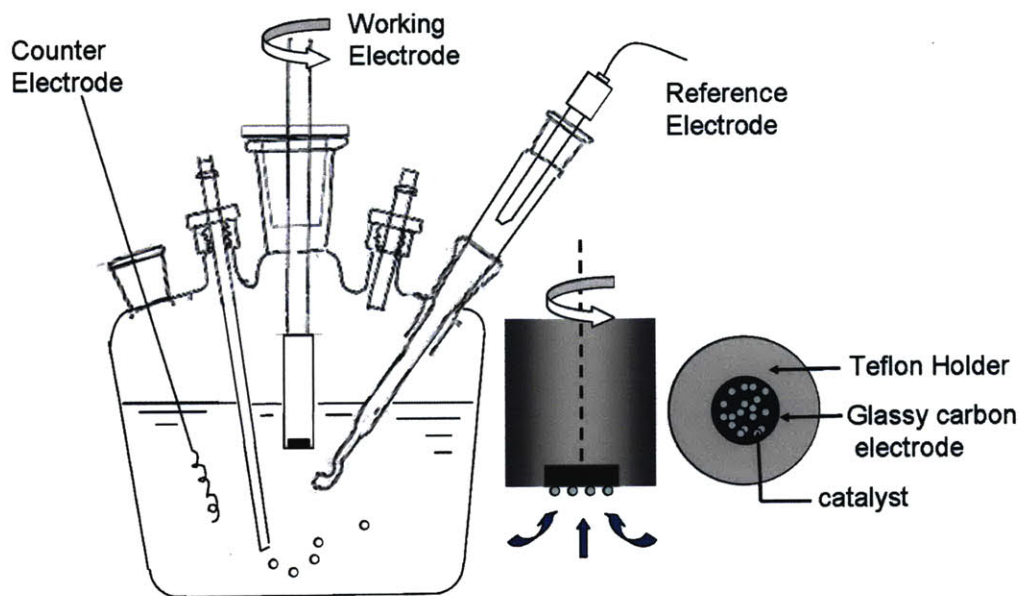


**Figure 1.5.** Typical cyclic voltammogram of Pt/C in Ar-saturated 0.1 M HClO<sub>4</sub> at a sweep rate of 50 mV/s.

### 1.5.3 Rotating disk electrode

Constructing a fuel cell device to perform an electrocatalytic characterization of the catalyst is somewhat cumbersome and time-consuming. The rotating disk electrode (RDE) technique is often utilized as an alternative screening tool for reactions that involves mass transport.<sup>8, 24</sup> In this work, a RDE technique is applied in a typical three-electrode electrochemical cell as shown in Scheme 1.2.

**Scheme 1.2.** Schematic of an electrochemical cell and a rotating disk electrode.



Because the loss in an electrochemical reaction involving gas reactant is typically a combination of the slow electrocatalytic activity of the catalyst and the poor mass transport of the reacting gas, a RDE method is generally used to differentiate between those two, allowing the electrocatalytic activity to be precisely quantified. The technique takes advantage of the convective transport induced by the rotation of the working electrode, which brought the reacting gas to the surface of the electrode in a controlled fashion. The flux of the gas to the electrode surface is dependent on the intrinsic properties of the electrolyte and the rotation rate. The measured current  $i$ , the kinetic current  $i_k$  and the mass transport limited current  $i_d$  satisfies the Levich equation:

$$\frac{1}{i} = \frac{1}{i_k} + \frac{1}{i_D} = \frac{1}{i_k} + \frac{1}{Bc_0\omega^{1/2}} = \frac{1}{i_k} + \frac{1}{0.2nFCD^{2/3}\nu^{-1/6}\omega^{1/2}} \quad [1.14]$$

where  $n$  is the number of transferred electrons,  $F$  is Faraday constant,  $C$  is the concentration of dissolved gas species,  $D$  is the diffusivity of the gas,  $\nu$  is the kinetic

viscosity of the electrolyte and  $\omega$  is the rotation rate. Plotting  $\frac{1}{i}$  vs.  $\frac{1}{\omega^{1/2}}$ , known as the Koutecky-Levich plot, will generate a straight line with a y-axis intercept given by the value  $\frac{1}{i_k}$ , and the slope being  $\frac{1}{Bc_0}$ . From the y-axis intercept, the kinetic current ( $i_k$ ) of the electrode can be determined, and from the slope ( $1/Bc_0$ ), the number of electrons being transferred can also be extracted. The kinetic current (typically at 0.9 V for the ORR) can then be normalized to the electrochemical surface area from cyclic voltammograms to generate specific activities as in mA/cm<sup>2</sup><sub>Pt</sub> or normalized by the Pt catalyst loading to generate mass activity as in A/mg<sub>Pt</sub>. The former provides an intrinsic electrocatalytic value of a catalyst and the latter provides the economical value of the catalyst, which essentially is the activity normalized to cost.

Figure 1.6 shows a typical polarization curve of the ORR on carbon supported Pt NPs in 0.1 M HClO<sub>4</sub> electrolyte. At high potential larger than 0.9 V, minimal current is observed due to the insufficient overpotential to drive the ORR forward. At potential more negative than 0.7 V, the overpotential is sufficiently large that all the O<sub>2</sub> molecules coming to the surfaces will be reduced immediately. As a result, the current in this potential range is limited by the O<sub>2</sub> mass transport to the electrode. In the potentials in between 0.7 – 0.9 V, the current is now under control by both the ORR kinetics and the O<sub>2</sub> mass transport. The inset is the Koutecky-Levich plot obtained at 0.6 V. From the calculated slope, the number of electron transferred is determined to be four, indicating that per mole of O<sub>2</sub>, a total of 4 moles of electrons are transferred, and thus prove a four-electron pathway of the ORR. Figure 1.6 (b) illustrates the relationship between the

potential ( $E$ ) and the specific activity ( $i_k$ ), known as the Tafel plot. From this figure, the Tafel slope of the ORR on Pt/C can be calculated, which yielded a value of 71 mV/dec.

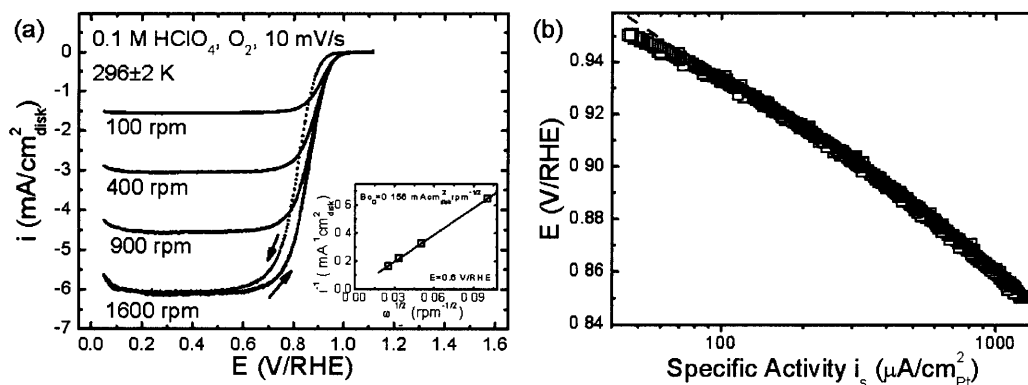


**Figure 1.6.** (a): Typical polarization curves of ORR on carbon supported Pt NPs at 10 mV/s at different rotation rates. Only the negative sweep at 1600 rpm is shown. The inset is the Koutecky-Levich plot obtained at 0.6 V/RHE. (b): Tafel plot with a TS=0.071 V/dec.

## 1.6 Structure of the thesis

In the following sections of this thesis, I will first present the study on the Pt particle size effect on the ORR activities in both acid and alkaline electrolytes and on the Pt instability in Chapter 2. The ORR activities of Pt NPs with a particle diameter between 1.6 nm to 4.7 nm are investigated in HClO<sub>4</sub> and H<sub>2</sub>SO<sub>4</sub> electrolyte using the RDE method. The surface electronic structure and surface compositions of Pt NPs examined by photoemission spectroscopic measurements including UPS and XPS are correlated to the ORR activity. Following that, the instability of Pt NPs with different particle diameters

under simulated PEMFC operation condition will be presented. The physics behind the size effect of Pt NPs on the ORR activity and Pt instability is discussed.

Chapter 3 deals with the HOR/HER activities on Pt electrodes in acidic and alkaline electrolytes. First, the HOR/HER activities on polycrystalline Pt disk and high surface area carbon supported Pt NPs in the alkaline electrolyte at different temperatures are demonstrated. The method of extracting the exchange current densities of the HOR/HER on Pt electrodes by fitting the experimental data to the theoretical Butler-Volmer equation is presented in great details. The kinetic information such as the exchange current densities and activation energies are compared to the DFT calculation results and the mechanisms of the HOR/HER on Pt electrodes in the alkaline electrolyte is discussed intensively. The consequence of the observed HOR/HER activities on Pt electrodes in alkaline electrolyte on the Pt anodic performance in an alkaline FC is predicted and compared to that in a PEMFC under identical operation conditions.

Chapter 4 presents the synthesis of multi-walled carbon nanotube supported Pt NPs as a corrosion-resistant electrocatalyst to overcome the carbon corrosion issue associated with the startup-shutdown cycles during the PEMFC operation. The synthesis of Pt/MWCNTs will be presented first, followed by the electrochemical characterizations to quantify both surface areas and electrocatalytic activities. Finally, the durability of Pt/MWCNTs under high potential is compared to that on high surface area carbon supported Pt NPs.

Chapter 5 summarizes all my major contributions to the understanding of the basic kinetics of the H<sub>2</sub>-O<sub>2</sub> based FC reactions from the proceeding chapters, and provides an overview of the future work.

## 1.7 References

1. Wand, G., *Fuel Cells History, part I*. Johnson Matthey: 2008;
2. Grove, W. R., *Phil. Trans. R. Soc. Lond.*, **1843**, (133).
3. Mond, L.; Langer, C., A New Form of Gas Battery, *Proceedings of the Royal Society of London*, **1889**, (46), 296.
4. Williams, K. R., Francis Thomas Bacon. 21 December 1904-24 May 1992, *Biographical Memoirs of Fellows of the Royal Society*, **1994**, 39, 2-18.
5. EG&G Technical Services, I., *Fuel Cell Handbook*. U.S. Department of Energy: 2004;
6. O'Hayre, R.; Cha, S.-W.; Colella, W.; Prinz, F. B., *Fuel Cell Fundamentals*. John Wiley & Sons: New York, 2006;
7. Vielstich, W.; Lamm, A.; Gasteiger, H. A., *Handbook of Fuel Cells: Fundamentals, Technology, Applications*. John Wiley & Sons: 2003;
8. Bard, A. J.; Faulkner, L. R., *Electrochemical Methods - Fundamentals and Applications*. John Wiley & Sons: New York, 2001;
9. Gasteiger, H. A.; Kocha, S. S.; Sompalli, B.; Wagner, F. T., Activity benchmarks and requirements for Pt, Pt-alloy, and non-Pt oxygen reduction catalysts for PEMFCs, *Applied Catalysis B-Environmental*, **2005**, 56, (1-2), 9-35.
10. Lima, F. H. B.; Zhang, J.; Shao, M. H.; Sasaki, K.; Vukmirovic, M. B.; Ticianelli, E. A.; Adzic, R. R., Catalytic activity-d-band center correlation for the O<sub>2</sub> reduction reaction on platinum in alkaline solutions, *Journal of Physical Chemistry C*, **2007**, 111, (1), 404-410.
11. Stamenkovic, V. R.; Fowler, B.; Mun, B. S.; Wang, G. F.; Ross, P. N.; Lucas, C. A.; Markovic, N. M., Improved oxygen reduction activity on Pt<sub>3</sub>Ni(111) via increased surface site availability, *Science*, **2007**, 315, (5811), 493-497.
12. Zhang, J.; Yang, H. Z.; Fang, J. Y.; Zou, S. Z., Synthesis and Oxygen Reduction Activity of Shape-Controlled Pt<sub>3</sub>Ni Nanopolyhedra, *Nano Letters*, **2010**, 10, (2), 638-644.
13. Lefevre, M.; Proietti, E.; Jaouen, F.; Dodelet, J. P., Iron-Based Catalysts with Improved Oxygen Reduction Activity in Polymer Electrolyte Fuel Cells, *Science*, **2009**, 324, (5923), 71-74.
14. Meng, H.; Jaouen, F.; Proietti, E.; Lefevre, M.; Dodelet, J. P., pH-effect on oxygen reduction activity of Fe-based electro-catalysts, *Electrochemistry Communications*, **2009**, 11, (10), 1986-1989.
15. Garland, N., DOE Hydrogen Program Annual Program Review, **2006**.
16. Shao-Horn, Y.; Sheng, W. C.; Chen, S.; Ferreira, P. J.; Holby, E. F.; Morgan, D., Instability of supported platinum nanoparticles in low-temperature fuel cells, *Topics in Catalysis*, **2007**, 46, (3-4), 285-305.
17. Iojoiu, C.; Guilminot, E.; Maillard, F.; Chatenet, M.; Sanchez, J. Y.; Claude, E.; Rossinot, E., Membrane and active layer degradation following PEMFC steady-state operation - II. Influence of Pt<sup>2+</sup> on membrane properties, *Journal of the Electrochemical Society*, **2007**, 154, (11), B1115-B1120.
18. Borup, R.; Meyers, J.; Pivovar, B.; Kim, Y. S.; Mukundan, R.; Garland, N.; Myers, D.; Wilson, M.; Garzon, F.; Wood, D.; Zelenay, P.; More, K.; Stroh, K.;



Zawodzinski, T.; Boncella, J.; McGrath, J. E.; Inaba, M.; Miyatake, K.; Hori, M.; Ota, K.; Ogumi, Z.; Miyata, S.; Nishikata, A.; Siroma, Z.; Uchimoto, Y.; Yasuda, K.; Kimijima, K. I.; Iwashita, N., Scientific aspects of polymer electrolyte fuel cell durability and degradation, *Chemical Reviews*, **2007**, *107*, (10), 3904-3951.

19. Patterson, T. W.; Darling, R. M., Damage to the cathode catalyst of a PEM fuel cell caused by localized fuel starvation, *Electrochemical and Solid State Letters*, **2006**, *9*, (4), A183-A185.

20. Reiser, C. A.; Bregoli, L.; Patterson, T. W.; Yi, J. S.; Yang, J. D. L.; Perry, M. L.; Jarvi, T. D., A reverse-current decay mechanism for fuel cells, *Electrochemical and Solid State Letters*, **2005**, *8*, (6), A273-A276.

21. Kinoshita, K., Particle-Size Effects for Oxygen Reduction on Highly Dispersed Platinum in Acid Electrolytes, *Journal of the Electrochemical Society*, **1990**, *137*, (3), 845-848.

22. Mayrhofer, K. J. J.; Strmcnik, D.; Blizanac, B. B.; Stamenkovic, V.; Arenz, M.; Markovic, N. M., Measurement of oxygen reduction activities via the rotating disc electrode method: From Pt model surfaces to carbon-supported high surface area catalysts, *Electrochimica Acta*, **2008**, *53*, (7), 3181-3188.

23. Hüfner, S., *Photoelectron Spectroscopy: Principles and Applications* Springer: Berlin Heidelberg, 2003;

24. Wang, J., *ANALYTICAL ELECTROCHEMISTRY*. John Wiley & Sons: Hoboken, New Jersey, 2006;



## Chapter 2

# Size Effect on the Oxygen Reduction Reaction Activity and Instability of Supported Pt Nanoparticles

### 2.1 Introduction

Oxygen reduction reaction (ORR)<sup>1-3</sup> is kinetically sluggish, even on the surface of Pt, which limits the efficiency of fuel cells. One of the intensively debated issues over the last two decades is centered on whether and how the intrinsic ORR activity of Pt nanoparticles (NPs) should be dependent on particle size. Although it is clear that Pt NPs have much reduced ORR activity than Pt bulk surfaces<sup>1, 4</sup>, the influence of particle size on the intrinsic ORR activity in the size range relevant to practical catalysts used in proton exchange membrane fuel cells (PEMFCs) is not well understood. Kinoshita<sup>5</sup> have first showed that the intrinsic ORR activity of Pt NPs with decreasing sizes (~15 to ~1.5 nm) in H<sub>2</sub>SO<sub>4</sub> and H<sub>3</sub>PO<sub>4</sub> reduces with increasing fractions of surface under-coordinated sites. The reduced ORR activity of smaller Pt NPs has been attributed to lower ORR activity on under-coordinated sites due to stronger adsorption of SO<sub>4</sub><sup>2-</sup> and PO<sub>4</sub><sup>3-</sup>, and decreasing fractions of highly active Pt (100) facets. Subsequently it is noted that decreasing Pt particle sizes (~30 to ~1 nm) also lowers ORR activity in HClO<sub>4</sub>,<sup>1, 6</sup> having minimal anion adsorption. This trend has been attributed to increasing surface oxygenated species with decreasing coordination of surface Pt atoms on smaller Pt NPs<sup>6</sup>, which thus inhibits the ORR as a spectator<sup>7</sup>. This argument is supported by increasing

OH/O adsorption strength on Pt NPs smaller than 5 nm as revealed from X-ray photoelectron spectroscopy<sup>8,9</sup>, and X-ray absorption spectroscopy<sup>10</sup>. In contrast, Yano et al.<sup>11</sup> have found that specific ORR activity of carbon-supported Pt NPs in the range of 1 to 5 nm in 0.1 M HClO<sub>4</sub> is size-independent, which has been attributed to comparable surface electronic structure of different Pt NPs from <sup>195</sup>Pt electrochemical nuclear magnetic resonance (EC-NMR) measurements.

In addition to the size-dependent ORR activity of Pt NPs, understanding the size-dependent instability of Pt NPs is of great importance to develop PEMFCs with required lifetime of a few thousands of hours for automotive applications.<sup>12</sup> Previous studies have shown that the electrochemical surface area (ESA) loss of Pt-based catalysts in the cathode limits PEMFC efficiency and lifetime<sup>12-15</sup>. Two processes are considered to contribute significantly to the ESA loss of Pt NPs in PEMFCs<sup>12, 14</sup>: i) coarsening of Pt NPs by Pt dissolution of smaller NPs and redeposition onto larger Pt NPs (also known as electrochemical Ostwald Ripening,<sup>12</sup> ii) loss of Pt mass from cathode.<sup>12-15</sup> Previous studies<sup>16-18</sup> have shown that the stability of Pt NPs can be highly size-dependent, which can be explained by the Gibbs-Thomson relation,<sup>16-18</sup> giving rise to higher free energy for Pt NP surface by  $\frac{2\gamma\Omega}{R}$  ( $\gamma$  is the surface energy of the particle,  $\Omega$  is the volume per atom, and  $R$  is the radius of the particle.) than that bulk surface.<sup>19</sup>

In this study, we examine the ORR activity of supported Pt NPs on carbon in the particle size from 1.6 nm to 4.7 nm in HClO<sub>4</sub> and H<sub>2</sub>SO<sub>4</sub> by using rotating disk electrode (RDE) measurements. The intrinsic ORR activity of Pt NPs in these catalysts is then correlated to the coverage of oxygenated species deduced from cyclic voltammetry, and surface Pt oxidation states and valence band information of Pt NPs obtained from X-ray

photoemission spectroscopy and ultraviolet photoemission spectroscopy measurements. In addition, we further compare the trend in the ORR activity of these Pt NPs as a function of particle size with that in the stability measured from potential cycling experiments. The origin in the size influence on the ORR activity and instability of Pt NPs having sizes smaller than ~5 nm is discussed.

## **2.2 Experimental**

### **2.2.1 Physical Characterization of Pt NP catalysts**

Five samples of Pt catalysts supported on high-surface-area carbon (Pt/C) were investigated in our study to explore the size-dependent behavior of the ORR. Three pristine Pt/C catalysts supplied by Tanaka Kikinzoku (TKK) have Pt weight fractions of 9% (TEC10E10A), 19% (TEC10E20A) and 46% (TEC1050E), respectively. The Pt/C catalyst containing 46% Pt NPs was further treated in Ar (99.999%, Airgas) at 900 °C for one minute or two hours (the ramping rate was ~30 °C per minute) to create larger Pt particle sizes. The samples were referred to as Pt-9%, Pt-19%, Pt-46%, Pt-46%-900°C-1m and Pt-46%-900°C-2h in the following text.

*2.2.1.1 High resolution transmission electron microscopy (HRTEM) measurements.* The Pt NP sizes of these samples were examined by high-resolution transmission electron microscope (HRTEM) on a JEOL 2010F operated at 200 kV with a point-to-point resolution of 0.19 nm. TEM samples were prepared by drop casting the catalyst powders dispersed ultrasonically for five minutes in ethanol onto TEM grids (Lacey carbon coated copper grids, Electron Microscopy Sciences) and then dried in air. Pt NP diameters ( $d$ ) were measured from bright field TEM micrographs. The number-

averaged ( $\bar{d}_n = \frac{\sum_1^n d_i}{n}$ ) diameter and the volume/area-averaged diameters, defined as

$$\bar{d}_{v/a} = \frac{\sum_1^n d_i^3}{\sum_1^n d_i^2} \quad \text{were calculated.}$$

*2.2.1.2 X-ray photoemission spectroscopy measurements.* Surface oxidation of supported Pt NPs was investigated by X-ray photoemission spectroscopy (XPS) on a Kratos Axis Ultra Spectrometer (Manchester, UK) with a monochromatized Al X-ray source (Al K $\alpha$ ). High-resolution spectra were collected for quantitative analysis of surface composition of Pt NPs. All spectra were calibrated with the sp<sup>2</sup> hybridized carbon component of C 1s at 284.5 eV. The photoemission spectra of Pt 4f were fitted to three species<sup>20, 21</sup> including Pt<sup>0</sup> at ~71.5 eV, Pt (II) at ~72.5 eV and Pt (IV) at ~74.8 eV after Shirley-type background subtraction. The ratios between Pt species of different oxidation states were calculated from the peak areas of deconvoluted Pt 4f spectra.

*2.2.1.3 Ultraviolet photoemission spectroscopy measurements.* Surface electronic structures of three Pt/C catalysts (Pt-19%, Pt-46% and Pt-46%-900°C-1m) and high-surface-area carbon (TKK) were examined by ultraviolet photoemission spectroscopy (UPS), and compared with Pt foil. Pt valence band of Pt-9% were not resolved because of the low signal to noise ratio due to its extremely low Pt loading. The catalyst powder samples were deposited on clean highly oriented pyrolytic graphite (HOPG, SPI Supplies). UPS measurements were performed at the U5UA beam line at the National Synchrotron Light Source at the Brookhaven National Laboratory. The ultraviolet photoemission spectra were collected with a 125-mm hemispherical analyzer at photon

energies of 80 eV under ultra high vacuum conditions of 5E-11 torr. The total instrument resolution was set to 0.10 eV. As the photoemission cross section of Pt is dominated by the d states at a photon energy of 80 eV<sup>22</sup>, the valence band structure measured mostly reflects the valence d states. Shirley-type background was subtracted to remove the secondary electron scattering as described in the literature<sup>23</sup>. To obtain the photoemission contribution from Pt NPs only, the density of states of carbon was subtracted from those of Pt/C samples. This method has been previously used by Eberhardt et al.<sup>24</sup> The d band center energy relative to the Fermi level was calculated from the density of states based

$$\text{on } d_{\text{center}} = \frac{\int N(\varepsilon)\varepsilon d\varepsilon}{\int N(\varepsilon)d\varepsilon} \quad 23.$$

## **2.2.2 Electrochemical Measurements**

*2.2.2.1 Preparation of Pt catalyst electrodes.* Pt loading of ~6.4-7.4  $\mu\text{g}_{\text{Pt}}/\text{cm}^2$  (except for 14  $\mu\text{g}_{\text{Pt}}/\text{cm}^2$  for Pt-46%-900°C-2h) on GCE without any Nafion<sup>®</sup> was used for cyclic voltammetry and the ORR measurements in both HClO<sub>4</sub> and H<sub>2</sub>SO<sub>4</sub>. Suspension of Pt-19%, Pt-46%, Pt-46%-900°C-1m and Pt-46%-900°C-2h of 0.15-0.70 mg/mL were obtained by dispersing the catalysts in de-ionized water (18.2 M $\Omega$ •cm, Millipore) using ultrasonication in ice-bath. 20  $\mu\text{L}$  of the Pt/C catalyst suspension was deposited on the glassy carbon electrode (GCE) (5 mm in diameter, Pine Instrument), which was pre-polished using alumina of 0.05 micron and dried in air at room temperature. Pt loading of ~10  $\mu\text{g}_{\text{Pt}}/\text{cm}^2$  was used for potential cycling experiments of Pt/C catalysts (Pt-46% and Pt-46%-900°C-1m). In addition, 20  $\mu\text{L}$  of 0.025 wt% Nafion<sup>®</sup> water solution (diluted

from 5 wt% Nafion®, Ion Power, Inc.) was added to dried catalyst thin film on GCE, which was dried subsequently in air to immobilize the catalysts.

#### *2.2.2.2 Electrochemical surface area measurements from cyclic voltammetry.*

Cyclic voltammograms (CV) on Pt/C were collected in both 0.1 M HClO<sub>4</sub> (diluted from 70% HClO<sub>4</sub>, GFS Chemicals.) and 0.5 M H<sub>2</sub>SO<sub>4</sub> (diluted from 18 M H<sub>2</sub>SO<sub>4</sub>, Sigma Aldrich). A Pt wire and a saturated calomel electrode (SCE, Analytical Sensor, Inc.) were employed as the counter electrode and the reference electrode, respectively. However, all the potentials reported in this paper were referenced to that of the reversible hydrogen electrode (RHE), which was calibrated from the RDE measurements of hydrogen oxidation<sup>25</sup>. After the electrolyte was saturated with Ar, the steady-state CV of the working electrode was recorded at 50 mV/s from 0.03 V to 1.1 V vs. RHE at the room temperature (296±2 K) after it was scanned between ~0.03 V and ~1.1 V vs. RHE at a sweep rate of 50 mV/s for ~20 cycles. CVs of catalyst thin films without Nafion® binder were measured with rotation at 1600 rpm to ensure that no catalyst fell off from GCE, where no change in the CV data was found before and after rotation. The ESA of Pt/C was determined from the Pt-hydrogen desorption region between 0.05 V and ~0.4 V (the onset of the double layer region) vs. RHE, assuming a surface charge density of 210 μC/cm<sup>2</sup><sub>Pt</sub> for a monolayer adsorption of hydrogen on Pt surface<sup>26</sup>.

#### *2.2.2.3 ORR activity measurements using rotating disk electrode.*

ORR activities of these Pt/C catalysts were examined in 0.1 M HClO<sub>4</sub> and 0.5 M H<sub>2</sub>SO<sub>4</sub> using RDE measurements. After the electrolyte was purged with pure oxygen (99.995%, Airgas) for at least half an hour, polarization curves were recorded between ~0.03 V and ~1.1 V vs. RHE at a sweep rate of 10 mV/s with rotation rates of 100, 400, 900 and 1600 rpm at



room temperature. To remove the capacitive currents of these Pt/C samples, oxygen reduction currents collected in O<sub>2</sub> atmosphere were obtained from subtracting the polarization curve in O<sub>2</sub> by the corresponding CV in Ar at the same sweep rate. The kinetic current  $i_k$  was calculated based on the Levich equation,  $\frac{1}{i} = \frac{1}{i_k} + \frac{1}{i_D}$  where  $i$  is the measured current and  $i_D$  is the mass-transport limited current. The specific activity  $i_s$  of ORR was then obtained by normalization of  $i_k$  by the electrochemical surface area of Pt.  $i_s$  and the mass activity  $i_m$  ( $i_k$  normalized by the weight of Pt) at 0.9V/RHE were used to compare the catalytic properties among the samples. The error bars were constructed from at least four repeat experiments. The Koutecky-Levich plot was obtained at E = 0.6 V/RHE for HClO<sub>4</sub> and 0.4 V/RHE for H<sub>2</sub>SO<sub>4</sub>, based on  $\frac{1}{i} = \frac{1}{i_k} + \frac{1}{i_D} = \frac{1}{i_k} + \frac{1}{Bc_0\omega^{1/2}}$ .  $Bc_0$ , determined from the slope, reflects the number of electrons transferred in the reaction and the predicted value for  $Bc_0$  is calculated based on  $i_D = 0.2nFC_{O_2}(D_{O_2})^{2/3}\nu^{-1/6}\omega^{1/2}$  where  $n$  is the number of transferred electrons,  $F$  is Faraday constant,  $C_{O_2}$  is the concentration of dissolved O<sub>2</sub>,  $D_{O_2}$  is the diffusivity of O<sub>2</sub>,  $\nu$  is the kinetic viscosity of the electrolyte and  $\omega$  is the rotation rate.

*2.2.2.4 Pt/C instability upon potential cycling.* Accelerated instability measurements of Pt/C catalysts were performed in N<sub>2</sub>-saturated 0.5 M H<sub>2</sub>SO<sub>4</sub> using potential cycling from 0.6 V to 1.0 V vs. RHE at 20 mV/s and at 80 °C. At the beginning of each potential cycling experiment, the working electrode was scanned between ~0.03 V and ~1.1 V vs. RHE at a sweep rate of 200 mV/s for 60 cycles to reach steady-state CV. After every 200 cycles at 80 °C, steady-state CVs were recorded subsequently at 50 mV/s

from 0.03 V to 1.1 V vs. RHE and at room temperature, from which the ESA of Pt/C catalysts was obtained as a function of cycles.

## **2.3. Results and Discussion**

### **2.3.1 Size distribution and surface morphology of Pt/C catalysts**

Figure 2.1a-e shows representative HRTEM images of supported Pt NPs of five catalyst samples used in this study, where single-crystalline Pt NPs were found to uniformly distribute on carbon support. The pristine Pt-9%, Pt-19% and Pt-46% catalysts have a number-averaged particle size of  $1.6\pm 0.5$  nm,  $1.7\pm 0.6$  nm and  $2.0\pm 0.6$  nm, respectively. As shown in Figure 2.1f, Pt-46%-900°C-1m and Pt-46%-900°C-2h have considerably larger particle sizes and wider size distributions of  $3.1\pm 0.7$  nm and  $4.7\pm 1.2$  nm, respectively. In addition, the volume/area-averaged diameter of each sample was calculated from the histogram data, from which the specific surface area based on HRTEM data was estimated, which is listed in Table 2.1.

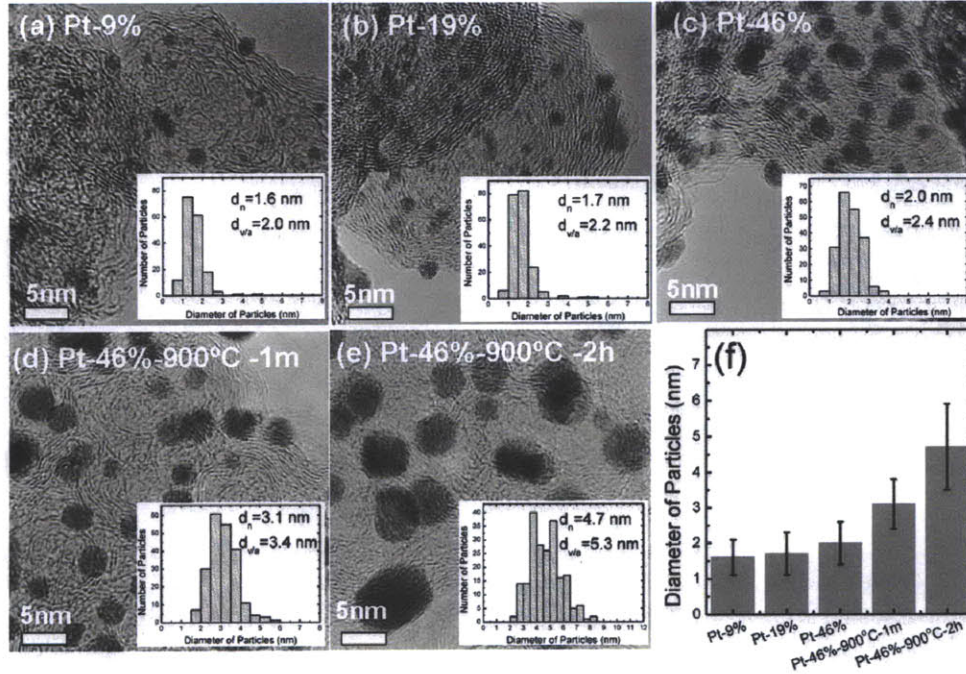


**Figure 2.1.** HRTEM images of Pt NPs for (a): Pt-9%; (b): Pt-19%; (c): Pt-46%; (d): Pt-46%-900°C-1m; (e): Pt-46%-900°C-2h; and (f): number-averaged diameters of Pt NPs for each sample. The scale bars are 5 nm. The insets are the Pt particle size distributions, and the indicated sizes are number-averaged ( $d_n$ ) and volume/area-averaged ( $d_{v/a}$ ) particle sizes. The error bars in (f) are standard deviations of the particle size based on at least 200 counts for each sample.

**Table 2.1.** The number and volume/area averaged diameters ( $d_n/d_{v/a}$ ) over 200 Pt NP counts from HRTEM measurements for each sample, surface area values of Pt NPs calculated from  $d_{v/a}$  based on  $S^{TEM} = 6000/(\rho_{Pt}d_{v/a})^{12}$ , surface area values of Pt NPs from CV measurements, the specific ORR activities and mass activities of Pt NPs in 0.1 M HClO<sub>4</sub> and 0.5 M H<sub>2</sub>SO<sub>4</sub>. The standard deviations are constructed based on at least four repeats of measurements for each sample.

	Particle size $d_n$ (nm)/ $d_{v/a}$ (nm)	$S^{TEM}$ (m <sup>2</sup> /g)	$S^{EC}$		$i_{s,0.9V}$ ( $\mu$ A/cm <sup>2</sup> <sub>Pt</sub> )	$i_{m,0.9V}$ (A/mg <sub>Pt</sub> )	$i_{s,0.9V}$ ( $\mu$ A/cm <sup>2</sup> <sub>Pt</sub> )	$i_{m,0.9V}$ (A/mg <sub>Pt</sub> )
			(0.1 M HClO <sub>4</sub> )	(0.5 M H <sub>2</sub> SO <sub>4</sub> )				
Pt-9%	1.6/2.0	140	148 ± 3		204 ± 8	0.30 ± 0.02		
Pt-19%	1.7/2.2	127	126 ± 3	117 ± 4	239 ± 9	0.30 ± 0.01	57 ± 4	0.067 ± 0.004
Pt-46%	2.0/2.4	117	78 ± 3	73 ± 4	355 ± 12	0.28 ± 0.01	66 ± 2	0.048 ± 0.002
Pt-46%-900°C-1m	3.1/3.4	82	38 ± 6	46 ± 2	238 ± 71	0.09 ± 0.03	57 ± 6	0.026 ± 0.003
Pt-46%-900°C-2h	4.7/5.3	53	24 ± 4	24 ± 2	299 ± 31	0.07 ± 0.02	72 ± 8	0.017 ± 0.002

### 2.3.2 Surface composition and electronic structure of Pt NPs

XPS was used to determine the Pt oxidation state of Pt NPs. Pt 4f doublet profile can be fitted to three components: Pt<sup>0</sup>, a Pt (II) and a Pt (IV) species. Representative Pt 4f doublet profile of the 1.7±0.6 nm sample is shown in Figure 2.2a, having Pt<sup>0</sup> with Pt 4f<sub>7/2</sub> peak at ~71.5 eV, Pt (II) with Pt 4f<sub>7/2</sub> peak centered at ~72.5 eV, and Pt (IV) at ~74.8 eV<sup>20, 21</sup>. The surface fractions of Pt<sup>0</sup> was found to increase from 47% to 56% with increasing particle size from 1.6±0.5 nm to 3.1±0.7 nm, and eventually level off at 4.7±1.2 nm (Figure 2.2b). This apparent size-dependent surface oxidation can be attributed to 1) increasing under-coordinated sites on smaller particles, which can bind more strongly with oxygen-containing species than terrace sites<sup>28</sup>.

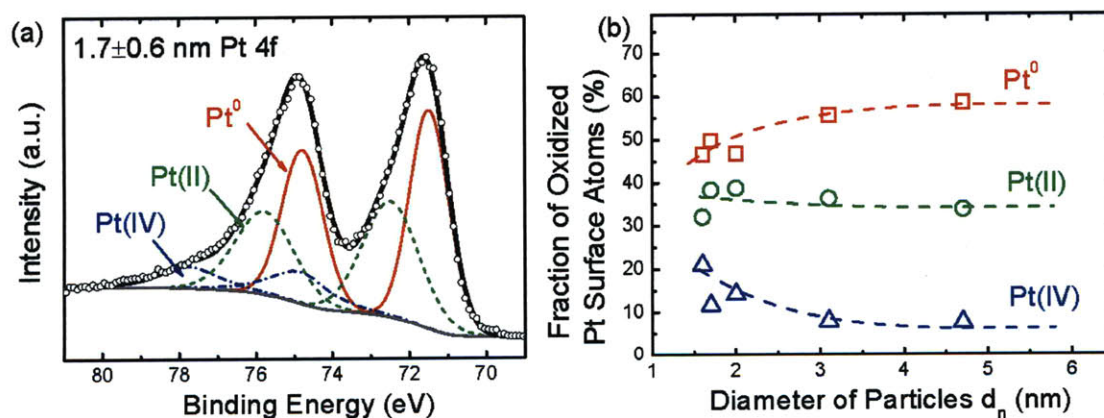


**Figure 2.2.** (a): Representative X-ray photoemission spectra of Pt 4f level for Pt-19% (1.7±0.6 nm) sample. Curve fitting was done after a Shirley-type background subtraction. The Pt 4f peaks were fitted into three sets of Pt species, i.e. Pt<sup>0</sup> (solid red line), Pt(II) (dashed green line) and Pt(IV) (dash-dotted blue line); and (b): the fractions of Pt surface atoms at different oxidation states calculated from the corresponding peak areas of Pt 4f spectra.

Surface electronic structure of these Pt NPs were examined using UPS. Figure 2.3a shows the partial valence band of bare HSAC and HSAC supported Pt NPs. The sole photoemission contributions of Pt NPs were obtained by subtracting the spectrum of HSAC from that of Pt/C, as shown in Figure 2.3b. All Pt NPs show well-developed density of states comparable to that of Pt foil near the Fermi level (binding energy equal to 0) while Pt NPs illustrate a higher density of states from -4 to -8 eV below the Fermi level. The valence band structure measured mostly reflects the valence d states because the cross section of s and p states is much smaller than that of d states at 80 eV<sup>22</sup>. It was found that Pt NPs have a much lower d band center compared to Pt foil, and interestingly the d band center was reduced slightly with decreasing particle size, as shown in Figure 2.3c. Although larger fractions of low-coordinated surface atoms<sup>5</sup> on Pt NPs than bulk surface should lead to a narrowed and up-shifted d band from previous DFT studies<sup>29-31</sup>, surface oxygen on Pt NPs can cause d band broadening and thus lower the d band center<sup>32</sup>. Therefore, the d-band lowering of smaller Pt NPs shown in UPS data can be attributed to increasing surface oxygenated species on Pt NPs with decreasing size as revealed by XPS results (Figure 2.2).

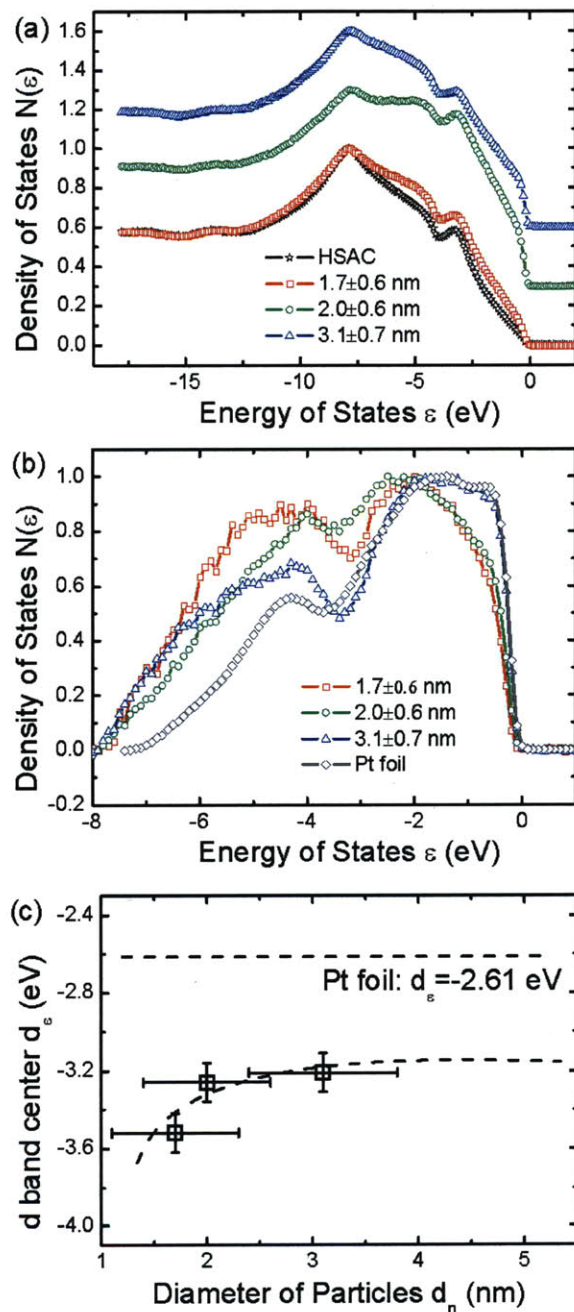


**Figure 2.3.** (a): Outer-level photoemission spectra of Pt-19% (1.7±0.6 nm, red square), Pt-46% (2.0±0.6 nm, green circle), Pt-46%-900°C-1m (3.1±0.7 nm, blue triangle), and a high-surface-area carbon sample (black star) collected at a photon energy of 80 eV; (b): subtracted photoemission signals of Pt NPs and Pt foil (grey pentagon); and (c): estimated d band center of Pt 5d emission relative to the Fermi level of different sized samples based on  $d_{center} = \int N(\epsilon)\epsilon d\epsilon / \int N(\epsilon)d\epsilon$ .<sup>23</sup> The error bars of x-axis in (c) are standard deviations of Pt NPs based on at least 200 particle counts for each sample, and the error bars of y-axis in (c) are the total UPS instrumental resolution (0.1 eV).

### **2.3.3 Cyclic voltammograms of Pt/C catalysts**

*2.3.3.1 ESA estimation of Pt/C catalysts.* Figures 2.4a and 2.4c show CVs of five catalyst samples collected in Ar-saturated 0.1 M HClO<sub>4</sub> and 0.5 M H<sub>2</sub>SO<sub>4</sub>. The CVs of these catalysts clearly show underpotential deposition of hydrogen on Pt between 0.05 V and ~0.4 V, followed by a double layer region, and Pt-OH formation and reduction in the voltage range from 0.6 to 0.8 V vs. RHE, which is in good agreement with previous studies<sup>26, 33, 34</sup>. The peaks in between 0.1 and 0.2 V and the broad shoulder in between 0.2 and 0.3 V correspond to the Pt-H adsorption/desorption on Pt (110) and Pt (100) facets, respectively. The ESA of Pt/C catalysts, estimated from the charge in the hydrogen desorption region, are compared with those calculated from the HRTEM data in Table 2.1. Pt NPs in pristine catalysts (Pt-9%, Pt-19% and Pt-46%) have very large ESA values in the range from 78 m<sup>2</sup>/g<sub>Pt</sub> to 148 m<sup>2</sup>/g<sub>Pt</sub>. As expected, Pt-46%-900°C-1m and Pt-46%-900°C-2h with larger particles have considerably lower ESA values. The ESA values of Pt NPs in pristine Pt-9% and Pt-19% catalysts are in very good agreement with the apparent, specific surface area estimated from HRTEM data, suggesting ~95% to ~99% of the apparent, specific surface area electrochemically active. This agreement should be treated with caution as HRTEM measurements in this study failed to detect Pt particles smaller than ~0.5 nm, which can contribute to ESA. With increasing particle sizes, the ratio between the ESA and the apparent, specific surface area from HRTEM data decreases to ~45% for the heat-treated catalysts, which can be attributed to the facts that 1) Pt NPs are perfectly spherical, 2) the contact between Pt NPs and the carbon support can reduce the percentage of the apparent, specific surface area electrochemically accessible and 3) the number of Pt NPs smaller than 0.5 nm is reduced significantly by

the heat-treatment.<sup>14</sup> Lastly, the ESA obtained in HClO<sub>4</sub> and H<sub>2</sub>SO<sub>4</sub> are very comparable, which suggests that anion adsorption may not interfere with H underpotential deposition on Pt.

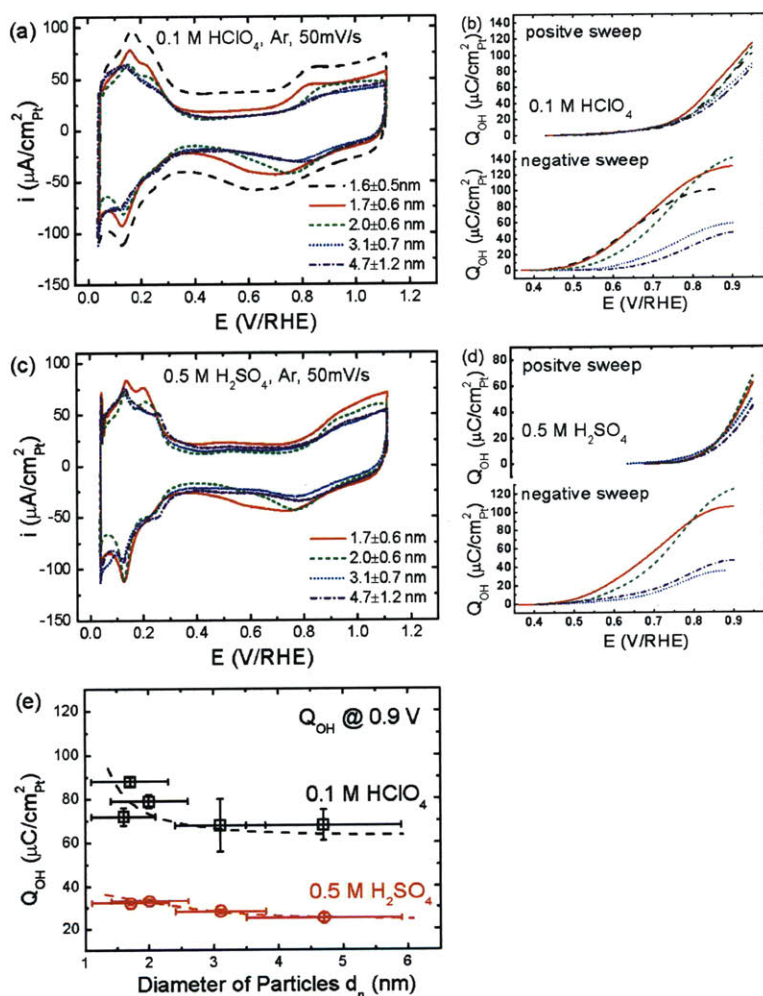


**Figure 2.4.** CVs of Pt NPs recorded at room temperature and at a sweep rate of 50 mV/s in (a): 0.1 M Ar-saturated HClO<sub>4</sub>; and (c): 0.5 M Ar-saturated H<sub>2</sub>SO<sub>4</sub>; (b): background-corrected charge density associated with Pt-OH formation in the positive sweeps (top) and Pt-OH reduction in the negative sweeps (bottom) in HClO<sub>4</sub>; (d): background-corrected charge density associated with Pt-OH formation (top) and Pt-OH reduction (bottom) in H<sub>2</sub>SO<sub>4</sub>; and (e): OH coverage at 0.9 V on the positive sweeps in HClO<sub>4</sub> and H<sub>2</sub>SO<sub>4</sub>. Error bars are standard deviations constructed from at least four repeats of experiments.



*2.3.3.2 Estimated surface coverage of oxygenated species on Pt NPs.* In the CVs, increasing oxidation current with an onset voltage at  $\sim 0.7$  V in the positive-going scan is associated with the formation of oxygenated species on Pt (e.g.  $\text{OH}_{\text{ad}}$ ) while the reduction peak around  $0.6\sim 0.8$  V in the negative-going scan is related to the reduction of Pt oxides. With decreasing Pt particle sizes, the onset voltage of rising oxidation current and the peak voltage of the reduction peak are shifted negatively. To examine this further, the charge densities associated with the formation and reduction of Pt oxygenated species, were calculated from CV data, as shown in Figures 2.4b and 2.4d. It is interesting to note that the coverage of oxygenated species such as  $\text{OH}_{\text{ad}}$  at  $0.9$  V, where ORR activity is typically measured, increased slightly with decreasing particle size in  $\text{HClO}_4$  and  $\text{H}_2\text{SO}_4$ , as shown in Figure 2.4e. This particle-size dependent trend is more apparent for reduction of Pt oxygenated species on the negative-going scan (Figure 2.4b and 2.4d, bottom panels). Not only the peak potential of Pt oxide reduction shifts significantly to the negative potential in the CV data with decreasing particle sizes, which can be attributed to increasing oxyphilicity of smaller Pt NPs and the formation of more irreversible oxide species,<sup>35</sup> but also the surface charge density or coverage of oxygenated species is much higher for smaller Pt NPs in the voltage range ( $0.8 - 0.9$  V vs. RHE), where ORR activity was determined typically.<sup>6</sup> Moreover, the onset voltage for the formation of oxygenated species on Pt NPs was influenced by anion adsorption, where it were delayed from  $\sim 0.7$  V in  $\text{HClO}_4$  to  $\sim 0.8$  V in  $\text{H}_2\text{SO}_4$  in the positive-going sweep due to strong (bi)sulfate anion adsorption<sup>36</sup>. This effect can be seen more clearly in the charge density of oxygenated species on Pt NPs in Figures 2.4b and 2.4d (top panels). For example, the

charge density of  $50 \mu\text{C}/\text{cm}^2_{\text{Pt}}$  was obtained at 0.85 V in  $\text{HClO}_4$  while this was achieved at 0.95 V in  $\text{H}_2\text{SO}_4$ .

### **2.3.4 ORR activity as a function of particle sizes**

ORR polarization curves of all catalyst samples on RDE show a diffusion-controlled region at voltages lower than 0.6-0.7 V, a diffusion-kinetic combined region, and a kinetic-controlled region<sup>2, 34</sup> at voltages equal to or greater than 0.9 V vs. RHE. Representative background-corrected polarization curves of the Pt-46% sample ( $2.0 \pm 0.6$  nm) at different rotation speeds in  $\text{HClO}_4$  and  $\text{H}_2\text{SO}_4$  are shown in Figures 2.5a and 2.5c, respectively. Diffusion-controlled currents are well defined for all catalysts as 1) diffusion currents of different catalysts are very comparable at a given rotation speed; and 2) representative Koutecky-Levich plots in Figures 2.5a and 2.5c insets show that diffusion currents linearly scale with  $\omega^{-1/2}$ , having  $Bc_0$  parameters of  $0.156 \text{ mAcm}^{-2} \text{ rpm}^{-1/2}$  (obtained at 0.6 V in  $\text{HClO}_4$ ) and  $0.133 \text{ mAcm}^{-2} \text{ rpm}^{-1/2}$  (obtained at 0.4 V in  $\text{H}_2\text{SO}_4$ ) in good agreement with previous studies<sup>37, 38</sup>. The background-corrected polarization curves of all catalysts compared at 1600 rpm in  $\text{HClO}_4$  and  $\text{H}_2\text{SO}_4$  show very comparable diffusion currents and a positive potential shift in the kinetic-controlled region with decreasing Pt NP size, as shown in Figures 2.5b and 2.5d, respectively. To remove the influence of catalyst loading on the current-potential profile in the kinetic-controlled region, kinetic currents extracted from these polarization curves were normalized to Pt ESA (specific ORR activity  $i_s$ ), which is plotted as a function of potential in the voltage range from 0.85 to 0.95 V in Figures 2.5b and 2.5d insets. While all the catalysts show very similar Tafel slopes having  $\sim 72$  mV/dec for  $\text{HClO}_4$  and 80

mV/dec for H<sub>2</sub>SO<sub>4</sub>, which agree well with previous studies<sup>2, 37</sup>, there is no apparent trend for size-dependent ORR activity, which will be examined in detail below.

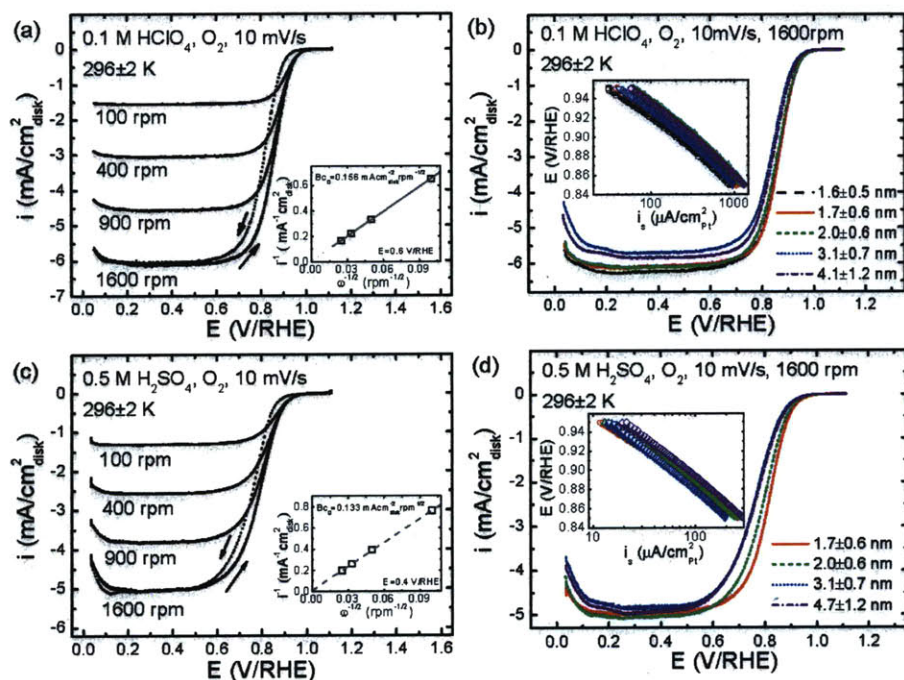


**Figure 2.5.** Representative background-corrected polarization curves of ORR on Pt-46% ( $2.0\pm 0.6$  nm) collected at a sweep rate of 10 mV/s and at room temperature in (a): O<sub>2</sub>-saturated 0.1 M HClO<sub>4</sub> and (c): O<sub>2</sub>-saturated 0.5 M H<sub>2</sub>SO<sub>4</sub>. The rotation rates are 100, 400, 900 and 1600 rpm. Solid lines represent positive-going scans and only negative-going scans at 1600 rpm are shown by the dotted lines. The insets are the Koutecky-Levich plot based on  $\frac{1}{i} = \frac{1}{i_k} + \frac{1}{i_D} = \frac{1}{i_k} + \frac{1}{Bc_0\omega^{1/2}}$  at 0.6 V for HClO<sub>4</sub> and 0.4 V for H<sub>2</sub>SO<sub>4</sub>;

background-corrected polarization curves of ORR at a sweep rate of 10 mV/s and at 1600 rpm in (b): O<sub>2</sub>-saturated 0.1 M HClO<sub>4</sub> and (d): O<sub>2</sub>-saturated 0.5 M H<sub>2</sub>SO<sub>4</sub>. The insets are the Tafel plots of these samples obtained from the normalized polarization curves in the positive-going scans at 1600 rpm. Pt loading of  $14 \mu\text{g}_{\text{Pt}}/\text{cm}^2$  on GCE was used for  $4.7\pm 1.2$  sample, and Pt loading of  $\sim 6.4\text{-}7.4 \mu\text{g}_{\text{Pt}}/\text{cm}^2$  were used for all the other samples.

The specific ORR activity  $i_s$  values at 0.9 V in HClO<sub>4</sub> and H<sub>2</sub>SO<sub>4</sub> as a function of number-averaged Pt NP size are summarized in Table 2.1 and Figure 2.6a. The specific ORR activity values for all catalyst samples were found to be  $\sim 300 \mu\text{A}/\text{cm}^2_{\text{Pt}}$  in HClO<sub>4</sub>

and  $\sim 60 \mu\text{A}/\text{cm}^2_{\text{Pt}}$  in  $\text{H}_2\text{SO}_4$ , which is in reasonable agreement with those reported previously<sup>1, 2, 6, 34</sup>. The five-fold reduction in the specific ORR activity in  $\text{H}_2\text{SO}_4$  can be attributed to strong adsorption of  $\text{SO}_4^{2-}$  ions.<sup>36</sup> Clearly between Pt NP sizes from  $1.6\pm 0.5$  nm to  $4.7\pm 1.2$  nm examined in this study, the specific ORR activity of Pt NPs is independent of particle size in both acids. Figure 2.6c compares the specific ORR activity in 0.1 M  $\text{HClO}_4$  in this work with those in previous studies.<sup>1, 34</sup> The specific ORR activity is plotted against the specific ESA of Pt instead of number-averaged size as different catalysts with comparable number-averaged sizes of Pt NPs can have very different specific ESA values. The specific ORR activity values at 25 °C from Gasteiger et al.<sup>1</sup> were extrapolated using an activation energy of 10 kJ/mol reported previously<sup>39</sup>. The specific ORR activity on Pt (pc) having specific ESA of  $0 \text{ m}^2/\text{g}_{\text{Pt}}$  was also included in the plot, where the values obtained from this study agree very well with those reported previously<sup>1, 34</sup>. Interestingly, we note that the ORR activity values of all Pt/C catalysts scatter from  $100 \mu\text{A}/\text{cm}^2_{\text{Pt}}$  to  $400 \mu\text{A}/\text{cm}^2_{\text{Pt}}$  without an obvious trend in the ESA range from  $30 \text{ m}^2/\text{g}_{\text{Pt}}$  ( $\sim 5$  nm) to  $150 \text{ m}^2/\text{g}_{\text{Pt}}$  ( $\sim 1.5$  nm), as shown in Figure 2.6c. Nevertheless, it should be pointed out that the specific ORR activity values of the three pristine Pt/C samples decrease with decreasing number-averaged sizes of Pt NPs ( $1.6\pm 0.5$  nm,  $1.7\pm 0.6$  nm and  $2.0\pm 0.6$  nm), which is in agreement with previous findings of similar catalysts<sup>34</sup>, the sizes of Pt NPs (0.5 nm and greater from HRTEM measurements shown in Figure 2.1) in these catalyst samples are very comparable considering standard deviation in the particle size histograms. This is in contrast to the fact that Pt NPs with considerably greater sizes (such as  $4.7\pm 1.2$  nm) prepared by a heat-treatment, do not show higher specific ORR activity, which suggests that the Pt NP size of Pt/C catalysts alone is not

sufficient to describe the specific ORR activity of Pt NPs. It is postulated that very small Pt NPs (smaller than  $\sim 0.5$  nm) present in the pristine catalyst samples but not in the heat-treated catalyst samples, may play a role in the weak size-dependent ORR activity, which needs to be studied in detail in future work. The significant increase in the specific ORR activity from several hundred  $\mu\text{A}/\text{cm}^2_{\text{Pt}}$  on Pt/C to over a thousand  $\mu\text{A}/\text{cm}^2_{\text{Pt}}$  on Pt (pc) appears to occur between  $\sim 30$   $\text{m}^2/\text{g}_{\text{Pt}}$  ( $\sim 5$  nm) and  $\sim 10$   $\text{m}^2/\text{g}_{\text{Pt}}$  ( $\sim 15$  nm), which is good agreement with the fact that Pt black<sup>1</sup> or nanostructured thin films of Pt<sup>34</sup> have specific ORR activity approaching that of Pt (pc).

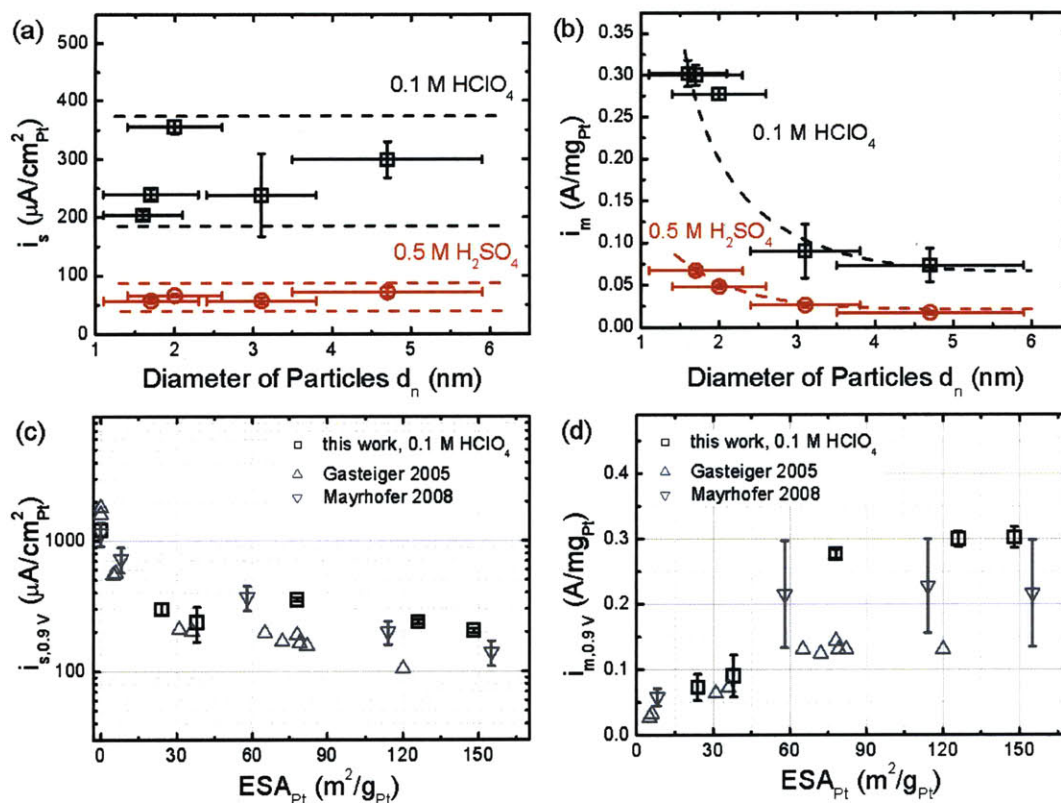


**Figure 2.6.** (a): The ORR specific activities at 0.9 V in 0.1 M HClO<sub>4</sub> and 0.5 M H<sub>2</sub>SO<sub>4</sub> as a function of the number-averaged diameter of Pt NPs ( $d_n$ ); (b): the ORR mass activities at 0.9 V in 0.1 M HClO<sub>4</sub> and 0.5 M H<sub>2</sub>SO<sub>4</sub> as a function of the number-averaged diameter of Pt NPs ( $d_n$ ); (c): the ORR specific activities at 0.9 V in 0.1 M HClO<sub>4</sub> in this work, compared with reference<sup>1</sup> and reference<sup>34</sup> as a function of ESA. Note that the data at 25 °C were calculated from the original data in reference<sup>1</sup> at 60 °C using an activation energy of 10 kJ/mol for the ORR as in reference<sup>39</sup>; and (d): the mass activities at 0.9 V in this work, compared with reference<sup>1</sup> and reference<sup>34</sup> as a function of ESA. The standard deviations in this work were constructed from at least four repeats of experiments.

Previous work<sup>6</sup> has suggested that increasing coverage of surface oxygenated species on Pt NPs of supported catalysts can reduce ORR activity of small Pt NPs, which is supported by a clear size-dependent coverage of oxygenated species obtained from CV data in the negative-going scans. However, it should be noted that the reported ORR activity in this previous study was obtained from the positive-going scans. Considering the coverage of oxygenated species in the negative-going scans can differ significantly

from that in the positive-going scans at the same potential, and there is a considerable difference in the specific activity between the negative-going and positive-going scans, as shown in Figure 2.4b and 2.4d, one may argue that it is more appropriate to correlate specific ORR activity with the coverage of oxygenated species in the same positive-going direction, which yields a weak size-dependent coverage of oxygenated species in Figure 2.4e. The slight increase in the oxygenated species with decreasing Pt NP size from CV measurements can be attributed to increasing fractions of surface under-coordinated sites. This finding is further supported by the increasing fraction of oxidized Pt species (Figure 2.2) and lowered d band center (Figure 2.3) with decreasing Pt NP size. Our previous work<sup>3</sup> has suggested that majority terrace sites instead of minor under-coordinated sites (such as edge and corner sites) on Pt NPs govern specific ORR activity. It is thus postulated that the size-independent activity in particle sizes lower than ~5 nm can be attributed to the following: 1) the specific ORR activity and the coverage of oxygenated species on terrace sites are comparable for all catalysts in this Pt NP size range, and 2) the specific ORR activity on majority terrace sites is much greater than those of minority under-coordinated sites.

As expected from the size-independent specific activity up to 5 nm, the mass activity values of these catalysts increase with decreasing particle size and reach a maximum for catalysts of  $1.6 \pm 0.5$  nm and  $1.7 \pm 0.6$  nm in  $\text{HClO}_4$  and  $\text{H}_2\text{SO}_4$ , as shown in Figures 2.6b and 2.6d. Specifically, with a three-fold reduction in the number-averaged particle size, the mass activity was found to increase by four-fold from  $0.07 \text{ A/mg}_{\text{Pt}}$  ( $4.7 \pm 1.2$  nm) to  $0.3 \text{ A/mg}_{\text{Pt}}$  ( $1.6 \pm 0.5$  nm). As catalysts are expected to operate in

PEMFCs for thousands of hours, the stability of these catalysts as a function of Pt NP size was examined by potential cycling, which is discussed in detail below.

### **2.3.5 Surface area loss as a function of particle size upon potential cycling**

Unlike the size-independent ORR activity, the instability of Pt NPs was found to be strongly dependent on the particle size even in a narrow size range, as shown in Figure 2.7. Upon potential cycling, Pt NPs with Pt-46% ( $2.0\pm 0.6$  nm) exhibit a faster current drop in the Pt-H interaction than Pt-46%-900°C-1m ( $3.1\pm 0.7$  nm), and in the Pt-OH region, as shown in Figures 2.7a and 2.7b, respectively. The specific and normalized ESA of Pt NPs of  $2.0\pm 0.6$  and  $3.1\pm 0.7$  nm as a function of the number of potential cycles in Figures 2.7c and 7d show a total ESA loss of 60% and 40%, respectively. The ESA loss upon potential cycling was accompanied with visible growth for Pt NPs of  $2.0\pm 0.6$  nm (Figures 2.8a-2.8c), where the number of particles below 1 nm was decreased greatly after 1200 cycles. On the other hand, no visible change was detected for Pt NPs of  $3.1\pm 0.7$  nm before and after cycling (Figures 2.8d-2.8f).



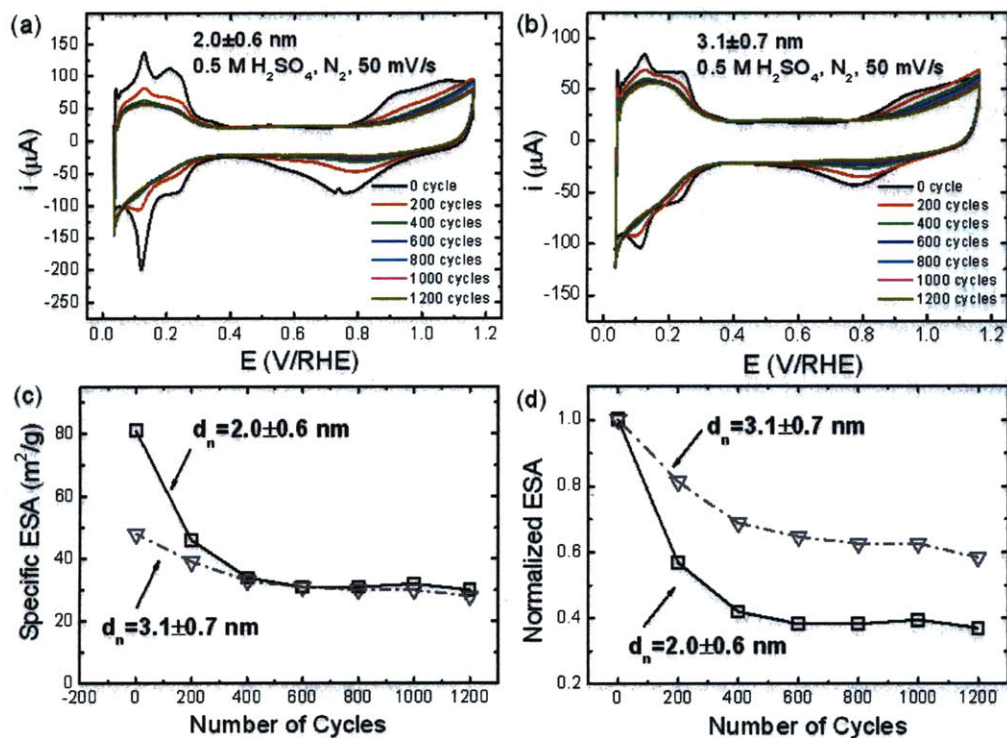


**Figure 2.7.** Steady-state CVs of (a): Pt-46% ( $2.0\pm 0.6$  nm) and (b): Pt-46%-900°C-1m ( $3.1\pm 0.7$  nm) after every 200 potential cycles. The CVs were recorded at 50 mV/s and at room temperature in 0.5 M N<sub>2</sub>-saturated H<sub>2</sub>SO<sub>4</sub>, after every 200 cycles at 80 °C between 0.6 V and 1.0 V at 20 mV/s. (c): The specific ESA of Pt NPs as a function of the number of potential cycles for Pt-46% ( $2.0\pm 0.6$  nm) and Pt-46%-900°C-1m ( $3.1\pm 0.7$  nm); and (d): normalized specific ESA of the two samples as a function of the number of potential cycles.

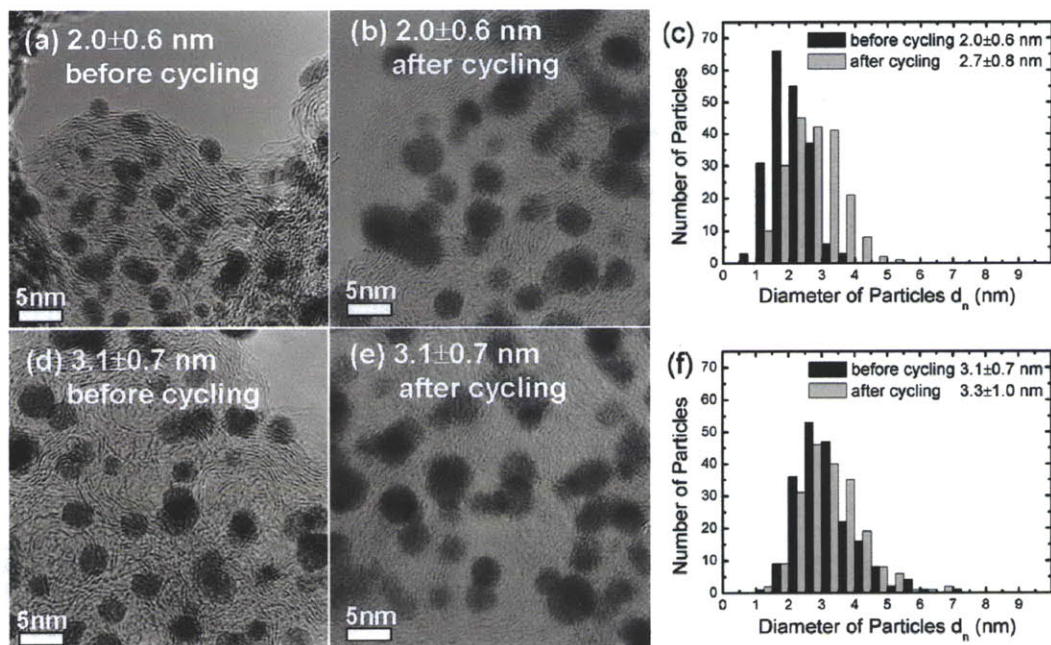


**Figure 2.8.** HRTEM images of Pt-46% ( $2.0\pm 0.6$  nm) before (a) and after (b) 1200 cycles between 0.6 V and 1.0 V at 80 °C and at 20 mV/s; HRTEM images of Pt-46%-900°C-1m ( $3.1\pm 0.7$  nm) before (d) and after (e) 1200 cycles; size distributions of Pt NPs before and after potential cycling for Pt-46% ( $2.0\pm 0.6$  nm) (c) and Pt-46%-900°C-1m ( $3.1\pm 0.7$  nm) (f). The indicated sizes are number-averaged particle sizes, and the standard deviations are based on at least 200 counts for each distribution.

It is very interesting to note that the P-H features on Pt(110) and Pt(100) diminish after the first 400 cycles for both samples. The remaining featureless Pt-H currents are probably coming from Pt(111)<sup>40</sup> as the most surface planes of Pt NPs are Pt(111) planes, which may suggest that Pt(110) and Pt(100) most likely dissolve faster than Pt(111).

Smaller particles with greater fractions of under-coordinated sites can show higher oxyphilicity towards O-containing species. Upon cycling to higher potentials, these oxygenated species on under-coordinated sites can promote Pt dissolution, which leads to loss of Pt mass (soluble Pt species) into the acid solution, and deposition of soluble Pt species onto larger Pt NPs upon potential cycling to lower potentials (Ostwald-

ripening). Therefore, it is hypothesized that the ESA loss for Pt NPs of 2 nm could come from Pt dissolution of smaller particles (smaller than 1 nm), and Ostwald ripening by which particles grow at the expense of smaller particles. Previous studies<sup>14, 19, 41, 42</sup> have shown that the size-dependent stability can be explained reasonably well by the Gibbs-Thomson relation.

## 2.4 Conclusions

The particle size effect on the ORR of Pt NPs is important to the fundamental understanding of the electrocatalysis process. By investigating a series of carbon-supported Pt NPs, we demonstrate that ORR activity is independent on the particle size in a range of particle size from  $1.6\pm 0.5$  nm to  $4.7\pm 1.2$  nm in both HClO<sub>4</sub> and H<sub>2</sub>SO<sub>4</sub> with ORR in H<sub>2</sub>SO<sub>4</sub> being significantly lower than that in HClO<sub>4</sub> due to strong (bi)sulfate adsorption. UPS measurements show that the surface valence band structure of Pt NPs is broadened and down-shifted compared to bulk material and XPS measurements illustrate that the amount of Pt oxides including Pt(II) and Pt(IV) on Pt surface increases as particle size increases. CVs demonstrate a weak size-dependent surface coverage by OH anion on different sized Pt NPs, which is most likely caused by Pt clusters smaller than 0.5 nm in pristine Pt samples. However, the coverage of oxygenated species on terrace sites are probably comparable for all catalysts in this Pt NP size range, and the specific ORR activity on majority terrace sites is much greater than those of minority under-coordinated sites, which results in the size-independent specific ORR activities. On the contrary, the instability of Pt NPs in acidic environment is found to strongly dependent on the particle sizes due to the Gibbs-Thomson effect. It suggests that a balance has to be maintained in

terms of decreasing particle sizes to obtain larger surface areas, thus a better overall PEMFC performance while keeping a reasonable durability of the catalysts under PEMFC operation.

## 2.5 References

1. Gasteiger, H. A.; Kocha, S. S.; Sompalli, B.; Wagner, F. T., Activity benchmarks and requirements for Pt, Pt-alloy, and non-Pt oxygen reduction catalysts for PEMFCs, *Applied Catalysis B-Environmental*, **2005**, *56*, (1-2), 9-35.
2. Paulus, U. A.; Schmidt, T. J.; Gasteiger, H. A.; Behm, R. J., Oxygen reduction on a high-surface area Pt/Vulcan carbon catalyst: a thin-film rotating ring-disk electrode study, *Journal of Electroanalytical Chemistry*, **2001**, *495*, (2), 134-145.
3. Seung Woo Lee; Shuo Chen; Jin Suntivich; Kotaro Sasaki; Radoslav R. Adzic; Shao-Horn, Y., Role of Surface Steps of Pt Nanoparticles on the electrochemical Activity for Oxygen Reduciton, *the Journal of Physical Chemistry Letters*, **2010**, (1), 1316-1320.
4. Stamenkovic, V. R.; Fowler, B.; Mun, B. S.; Wang, G. F.; Ross, P. N.; Lucas, C. A.; Markovic, N. M., Improved oxygen reduction activity on Pt<sub>3</sub>Ni(111) via increased surface site availability, *Science*, **2007**, *315*, (5811), 493-497.
5. Kinoshita, K., Particle-Size Effects for Oxygen Reduction on Highly Dispersed Platinum in Acid Electrolytes, *Journal of the Electrochemical Society*, **1990**, *137*, (3), 845-848.
6. Mayrhofer, K. J. J.; Blizanac, B. B.; Arenz, M.; Stamenkovic, V. R.; Ross, P. N.; Markovic, N. M., The impact of geometric and surface electronic properties of Pt-catalysts on the particle size effect in electrocatalysis, *Journal of Physical Chemistry B*, **2005**, *109*, (30), 14433-14440.
7. Strmcnik, D. S.; Rebec, P.; Gaberscek, M.; Tripkovic, D.; Stamenkovic, V.; Lucas, C.; Markovic, N. M., Relationship between the surface coverage of spectator species and the rate of electrocatalytic reactions, *Journal of Physical Chemistry C*, **2007**, *111*, (50), 18672-18678.
8. Peuckert, M.; Yoneda, T.; Betta, R. A. D.; Boudart, M., Oxygen Reduction on Small Supported Platinum Particles, *Journal of the Electrochemical Society*, **1986**, *133*, (5), 944-947.
9. Takasu, Y.; Ohashi, N.; Zhang, X. G.; Murakami, Y.; Minagawa, H.; Sato, S.; Yahikozawa, K., Effects of platinum particles on the electroreduction of oxygen, *Electrochimica Acta*, **1996**, *41*, (16), 2595-2600.
10. Mukerjee, S.; McBreen, J., Effect of particle size on the electrocatalysis by carbon-supported Pt electrocatalysts: an in situ XAS investigation, *Journal of Electroanalytical Chemistry*, **1998**, *448*, (2), 163-171.
11. Yano, H.; Inukai, J.; Uchida, H.; Watanabe, M.; Babu, P. K.; Kobayashi, T.; Chung, J. H.; Oldfield, E.; Wieckowski, A., Particle-size effect of nanoscale platinum catalysts in oxygen reduction reaction: an electrochemical and Pt-195 EC-NMR study, *Physical Chemistry Chemical Physics*, **2006**, *8*, (42), 4932-4939.
12. Ferreira, P. J.; la O', G. J.; Shao-Horn, Y.; Morgan, D.; Makharia, R.; Kocha, S.; Gasteiger, H. A., Instability of Pt/C electrocatalysts in proton exchange membrane fuel cells - A mechanistic investigation, *Journal of the Electrochemical Society*, **2005**, *152*, (11), A2256-A2271.
13. Bi, W.; Gray, G. E.; Fuller, T. F., PEM fuel cell Pt/C dissolution and deposition in nafion electrolyte, *Electrochemical and Solid State Letters*, **2007**, *10*, (5), B101-B104.

14. Shao-Horn, Y.; Sheng, W. C.; Chen, S.; Ferreira, P. J.; Holby, E. F.; Morgan, D., Instability of supported platinum nanoparticles in low-temperature fuel cells, *Topics in Catalysis*, **2007**, *46*, (3-4), 285-305.
15. Yasuda, K.; Taniguchi, A.; Akita, T.; Ioroi, T.; Siroma, Z., Platinum dissolution and deposition in the polymer electrolyte membrane of a PEM fuel cell as studied by potential cycling, *Physical Chemistry Chemical Physics*, **2006**, *8*, (6), 746-752.
16. Chen, Z. W.; Waje, M.; Li, W. Z.; Yan, Y. S., Supportless Pt and PtPd nanotubes as electrocatalysts for oxygen-reduction reactions, *Angewandte Chemie-International Edition*, **2007**, *46*, (22), 4060-4063.
17. Debe, M. K.; Schmoeckel, A. K.; Vernstrom, G. D.; Atanasoski, R., High voltage stability of nanostructured thin film catalysts for PEM fuel cells, *Journal of Power Sources*, **2006**, *161*, (2), 1002-1011.
18. Yasuda, K.; Taniguchi, A.; Akita, T.; Ioroi, T.; Siroma, Z., Characteristics of a platinum black catalyst layer with regard to platinum dissolution phenomena in a membrane electrode assembly, *Journal of the Electrochemical Society*, **2006**, *153*, (8), A1599-A1603.
19. Darling, R. M.; Meyers, J. P., Kinetic model of platinum dissolution in PEMFCs, *Journal of the Electrochemical Society*, **2003**, *150*, (11), A1523-A1527.
20. de la Fuente, J. L. G.; Rojas, S.; Martinez-Huerta, M. V.; Terreros, P.; Pena, M. A.; Fierro, J. L. G., Functionalization of carbon support and its influence on the electrocatalytic behaviour of Pt/C in H<sub>2</sub> and CO electrooxidation, *Carbon*, **2006**, *44*, (10), 1919-1929.
21. Shuangyin, W.; San Ping, J.; Timothy John, W.; Jun, G.; Xin, W., Assembling Interconnected Pt Nanoparticles on Multiwalled Carbon Nanotubes and Their Electrocatalytic Activity for Fuel Cells, *Advanced Functional Materials*, **2009**, *19*, 1-8.
22. Yeh, J. J.; Lindau, I., Atomic Subshell Photoionization Cross-Sections and Asymmetry Parameters - 1 Less-Than-or-Equal-to Z Less-Than-or-Equal-to 103, *Atomic Data and Nuclear Data Tables*, **1985**, *32*, (1), 1-155.
23. Mun, B. S.; Watanabe, M.; Rossi, M.; Stamenkovic, V.; Markovic, N. M.; Ross, P. N., A study of electronic structures of Pt<sub>3</sub>M (M=Ti, V, Cr, Fe, Co, Ni) polycrystalline alloys with valence-band photoemission spectroscopy, *Journal of Chemical Physics*, **2005**, *123*, (20), 204717-204720.
24. Eberhardt, W.; Fayet, P.; Cox, D. M.; Fu, Z.; Kaldor, A.; Sherwood, R.; Sondericker, D., Photoemission from Mass-Selected Monodispersed Pt Clusters, *Physical Review Letters*, **1990**, *64*, (7), 780-784.
25. Chen, S.; Sheng, W. C.; Yabuuchi, N.; Ferreira, P. J.; Allard, L. F.; Shao-Horn, Y., Origin of Oxygen Reduction Reaction Activity on "Pt<sub>3</sub>Co" Nanoparticles: Atomically Resolved Chemical Compositions and Structures, *Journal of Physical Chemistry C*, **2009**, *113*, (3), 1109-1125.
26. Nart, F. C.; Vielstich, W., Normalization of porous active surfaces. In *Handbook of Fuel Cells - Fundamentals, Technology and Applications*, Wolf Vielstich, H. A. G. a. A. L., Ed. John Wiley & Sons, Ltd.: 2003; Vol. 2, pp 302-315.
27. Bard, A. J.; Faulkner, L. R., *Electrochemical Methods: Fundamentals and Applications*. John Wiley & Sons: New York, 2001;

28. Han, B. C.; Miranda, C. R.; Ceder, G., Effect of particle size and surface structure on adsorption of O and OH on platinum nanoparticles: A first-principles study, *Physical Review B*, **2008**, *77*, (7), 075410-075418.
29. Hammer, B.; Nielsen, O. H.; Norskov, J. K., Structure sensitivity in adsorption: CO interaction with stepped and reconstructed Pt surfaces, *Catalysis Letters*, **1997**, *46*, (1-2), 31-35.
30. Norskov, J. K., Chemisorption on Metal-Surfaces, *Reports on Progress in Physics*, **1990**, *53*, (10), 1253-1295.
31. Sun, Y.; Zhuang, L.; Lu, J.; Hong, X.; Liu, P., Collapse in crystalline structure and decline in catalytic activity of Pt nanoparticles on reducing particle size to 1 nm, *Journal of the American Chemical Society*, **2007**, *129*, (50), 15465-15467.
32. Lynch, M.; Hu, P., A density functional theory study of CO and atomic oxygen chemisorption on Pt(111), *Surface Science*, **2000**, *458*, (1-3), 1-14.
33. Zhang, J.; Sasaki, K.; Sutter, E.; Adzic, R. R., Stabilization of platinum oxygen-reduction electrocatalysts using gold clusters, *Science*, **2007**, *315*, (5809), 220-222.
34. Mayrhofer, K. J. J.; Strmcnik, D.; Blizanac, B. B.; Stamenkovic, V.; Arenz, M.; Markovic, N. M., Measurement of oxygen reduction activities via the rotating disc electrode method: From Pt model surfaces to carbon-supported high surface area catalysts, *Electrochimica Acta*, **2008**, *53*, (7), 3181-3188.
35. Angerstein, H.; Conway, B. E.; Sharp, W. B. A., Real Condition of Electrochemically Oxidized Platinum Surfaces .1. Resolution of Component Processes, *Journal of Electroanalytical Chemistry*, **1973**, *43*, (1), 9-36.
36. Markovic, N. M.; Ross, P. N., Surface science studies of model fuel cell electrocatalysts, *Surface Science Reports*, **2002**, *45*, (4-6), 121-229.
37. Paulus, U. A.; Wokaun, A.; Scherer, G. G.; Schmidt, T. J.; Stamenkovic, V.; Radmilovic, V.; Markovic, N. M.; Ross, P. N., Oxygen reduction on carbon-supported Pt-Ni and Pt-Co alloy catalysts, *Journal of Physical Chemistry B*, **2002**, *106*, (16), 4181-4191.
38. Markovic, N. M.; Gasteiger, H. A.; Ross, P. N., Oxygen Reduction on Platinum Low-Index Single-Crystal Surfaces in Sulfuric-Acid-Solution - Rotating Ring-Pt(Hkl) Disk Studies, *Journal of Physical Chemistry*, **1995**, *99*, (11), 3411-3415.
39. Neyerlin, K. C.; Gu, W. B.; Jorne, J.; Gasteiger, H. A., Determination of catalyst unique parameters for the oxygen reduction reaction in a PEMFC, *Journal of the Electrochemical Society*, **2006**, *153*, (10), A1955-A1963.
40. Markovic, N.; Gasteiger, H.; Ross, P. N., Kinetics of oxygen reduction on Pt(hkl) electrodes: Implications for the crystallite size effect with supported Pt electrocatalysts, *Journal of the Electrochemical Society*, **1997**, *144*, (5), 1591-1597.
41. Holby, E. F.; Sheng, W. C.; Shao-Horn, Y.; Morgan, D., Pt nanoparticle stability in PEM fuel cells: influence of particle size distribution and crossover hydrogen, *Energy & Environmental Science*, **2009**, *2*, (8), 865-871.
42. Tang, L.; Han, B.; Persson, K.; Friesen, C.; He, T.; Sieradzki, K.; Ceder, G., Electrochemical Stability of Nanometer-Scale Pt Particles in Acidic Environments, *Journal of the American Chemical Society*, **2010**, *132*, (2), 596-600.





## Chapter 3

### Hydrogen Oxidation and Evolution Reaction Kinetics on Platinum: Acid vs. Alkaline Electrolytes

#### 3.1 Introduction

Fuel cells show promise to provide environmentally friendly energy conversion at high efficiency and high power density. One of the major focus areas in proton exchange membrane fuel cell (PEMFC) research is the oxygen reduction reaction (ORR) on the cathode, because the slow ORR kinetics are responsible for more than 50% of the overall cell voltage loss during PEMFC operation.<sup>1-3</sup> Thus, even on platinum (Pt), the most active ORR catalyst in PEMFCs, the ORR overpotential is typically on the order of 300 to 400 mV<sup>4</sup>, consistent with the very low ORR exchange current density of only  $\approx 10^{-8}$  A/cm<sup>2</sup><sub>Pt</sub> at 80 °C<sup>5</sup>. The same applies to the ORR in alkaline electrolytes, where Pt has similar ORR activity as in acid.<sup>6, 7</sup>, and again is among the most active catalysts<sup>8</sup> (including catalysts<sup>9, 10</sup> with active sites composed of nitrogen-coordinated iron and/or cobalt displaying ORR activities comparable to Pt). This suggests that the ORR overpotential loss in alkaline fuel cells (AFCs) or alkaline membrane fuel cells (AMFCs) is very similar to that in PEMFCs, i.e., that the cathode overpotential loss still remains the major factor limiting the overall energy conversion efficiency and performance of AFCs<sup>11</sup> and AMFCs<sup>10</sup>.

In contrast to the slow ORR kinetics, the kinetics of the hydrogen oxidation reaction (HOR) on Pt anode catalysts in a PEMFC are so fast that the cell voltage losses at the anode are negligible even for very low Pt loadings ( $<5$  mV at anode Pt loadings of  $0.05 \text{ mg}_{\text{Pt}}/\text{cm}^2_{\text{electrode}}$ <sup>12</sup>). As a matter of fact, due to the very high HOR exchange current density,  $i_0$ , on Pt in acid electrolytes, its quantification is experimentally difficult, leading to a wide range of experimentally reported values in acid electrolytes at room temperature. For example, HOR exchange current densities measured by the rotating disk electrode (RDE) technique are reported to be on the order of  $\approx 1 \text{ mA}/\text{cm}^2_{\text{Pt}}$  on polycrystalline Pt<sup>13</sup>, Pt single-crystals<sup>14</sup>, and carbon supported Pt (Pt/C)<sup>15</sup>. On the other hand, much larger values of 24 to  $50 \text{ mA}/\text{cm}^2_{\text{Pt}}$  have been obtained by micro-electrode studies on Pt/C<sup>16</sup> and polycrystalline Pt<sup>17</sup> or by Pt/C based gas-diffusion electrodes<sup>18</sup>. Moreover, the observed H<sub>2</sub>/air PEMFC performance independence of Pt anode loadings (varied between 0.4 and  $0.05 \text{ mg}_{\text{Pt}}/\text{cm}^2_{\text{electrode}}$ ), could only be rationalized by assuming very high HOR exchange current densities<sup>19</sup>, and subsequent kinetic measurements in PEMFCs at 80 °C indeed yielded  $i_0$  values of  $400 \pm 200 \text{ mA}/\text{cm}^2_{\text{Pt}}$ <sup>12</sup>. This ambiguity in the measurement of the HOR/HER kinetics in acid can be related to the fact that it is experimentally very challenging to eliminate hydrogen mass-transport resistances in RDE measurements. For example, if one were to assume that the HOR/HER exchange current density were ten-fold larger than the diffusion-limited HOR current density ( $\approx 3.5 \text{ mA}/\text{cm}^2_{\text{disk}}$  at typical maximum rotation rates of 3600 rpm<sup>14</sup>), the quantification of kinetic constants for the HOR/HER would not be possible.

As micro-electrode studies on polycrystalline Pt actually suggest two orders of magnitude lower HOR/HER exchange current densities in alkaline compared to acidic

electrolytes,<sup>17</sup> RDE measurements may allow the quantification of HOR/HER kinetics in KOH. Previous RDE measurements of the HOR/HER kinetics in alkaline electrolytes on Pt single-crystals have yielded exchange current densities on the order of  $\approx 1 \text{ mA/cm}^2_{\text{Pt}}$ .<sup>20,</sup>  
<sup>21</sup> However, neither HOR/HER exchange current densities nor reaction mechanism details have been reported for industrially relevant carbon supported Pt catalyst (Pt/C) catalysts in alkaline electrolyte. If they were on the order of only  $1 \text{ mA/cm}^2_{\text{Pt}}$ , it would imply that the anode overpotential losses in AFCs/AMFCs would be substantial, prohibiting the use of ultra-low anode Pt loadings which have been demonstrated successfully in PEMFCs ( $0.05 \text{ mg}_{\text{Pt}}/\text{cm}^2_{\text{electrode}}$ <sup>12</sup>).

In this study, we investigate the HOR/HER kinetics on polycrystalline Pt (Pt(pc)) and Pt/C at different temperatures using RDE measurements combined with in-situ uncompensated solution resistance measurements (i.e.,  $iR$ -correction term via AC impedance). In addition, the temperature-dependent HOR/HER exchange current densities can be well modeled using the Butler-Volmer equation, from which the mechanism of the HOR in alkaline solution is discussed. Moreover, comparative measurements illustrate that the HOR/HER kinetics in acid electrolyte is orders of magnitude faster, which cannot be quantified by RDE measurements due to the Nernstian diffusion overpotential as suggested previously.<sup>17, 22</sup> Furthermore, we contrast ORR activity of Pt(pc) and Pt/C in alkaline with acid, after which the performance of AFCs/AMFCs and PEMFCs using Pt/C at the anode and cathode is compared.

## **3.2 Experimental**

### **3.2.1 Electrode Preparation**

Thin film electrodes of high surface area carbon supported Pt catalyst were made with 46 (wt)% Pt (Pt/C) supplied by Tanaka Kikinok International Inc. (TKK) following previous studies.<sup>23, 24</sup> The average Pt nanoparticle (NP) diameter of the Pt/C determined by transmission electron microscopy (TEM) was  $2.0 \pm 0.6$  nm based on at least 200 particle counts. Aqueous suspensions of Pt/C of  $\sim 0.15$  mg/mL were obtained by dispersing the catalyst in de-ionized water ( $18.2$  M $\Omega$ -cm, Millipore) using ultrasonication of the suspension in an ice-bath.  $20$   $\mu$ L of the Pt/C catalyst water suspension were deposited on a glassy carbon electrode (GCE) disk ( $5$  mm diameter, Pine Instruments) which was polished with  $0.05$  micron alumina (Buehler), and dried in air at room temperature, resulting in a Pt loading of  $\sim 7.0$   $\mu$ g<sub>Pt</sub>/cm<sup>2</sup> on GCE. The polycrystalline Pt disk electrode ( $5$  mm diameter, Pine Instruments) was also polished with  $0.05$  micron alumina and was cleaned by ultrasonication in de-ionized water.

### **3.2.2 Modification of the Reference Electrode**

It is well known that glass corrodes in alkaline solution and the arising contaminants (lead and silica) can significantly influence the ORR and the HOR/HER activity of Pt electrodes.<sup>25, 26</sup> To minimize contamination from the gradual dissolution of glass, fresh alkaline electrolyte was prepared for each electrochemical measurement at each temperature, and all electrochemical data were collected within 30 minutes. More importantly, we also modified the Luggin capillary, replacing the highly KOH-soluble

vycor glass tip of the Luggin capillary with a 50  $\mu\text{m}$  thick Nafion<sup>®</sup> film, analogous to what was shown previously<sup>27</sup>. Short exposure time and modification of the Luggin capillary tip eliminated contamination; consequently, as will be shown later, the HOR/HER and ORR activities obtained in our study are equal to those reported for measurements in a Teflon<sup>®</sup> cell.<sup>26</sup>

### **3.2.3 Electrochemical Measurements**

The electrochemical measurements were carried out in a jacketed glass cell (Pine Instruments), connected to a circulating temperature-controlled water bath (Thermo Electron Corp.). As prepared Pt/C thin film electrodes or a polycrystalline Pt disk were mounted onto a rotator (Pine Instruments) and immersed into 0.1 M potassium hydroxide (99.99% purity, Sigma Aldrich) solution. A Pt wire served as the counter electrode and a saturated calomel electrode (SCE, Analytical Sensor, Inc.), immersed into the Nafion<sup>®</sup> film modified Luggin capillary filled with 0.1 M KOH was used as the reference electrode. However, all potentials reported in this paper are referenced to the reversible hydrogen electrode (RHE) potential, calibrated in the same electrolyte by measuring HOR/HER currents on the Pt RDE, whereby the potential at zero current corresponds to 0 V vs. RHE. After the electrolyte was saturated with argon, the cyclic voltammogram at 294 K was recorded between  $\sim 0.08$  and  $\sim 1.0$  V vs. RHE at a scan rate of 50 mV/s after it reached steady-state.

The HOR/HER rates were measured using rotating disk electrode measurements. After the electrolyte was saturated with pure hydrogen, polarization curves were recorded between  $\sim -0.08$  and  $\sim 1.0$  V vs. RHE at a sweep rate of 10 mV/s and rotation rates of 400,

900, 1600 and 2500 rpm. Freshly prepared 0.1 M KOH electrolyte was used for each measurement at each temperature as described above. Exchange current densities,  $i_0$ , of the HOR/HER were obtained by fitting the experimental data to the Butler-Volmer equation. The HOR/HER was also measured on Pt(pc) in H<sub>2</sub>-saturated 0.1 M HClO<sub>4</sub> (70%, GFS Chemicals Inc.) using the same method and the same experimental conditions.

After measurements of the HOR/HER at 294 K, the ORR kinetics were also measured on Pt(pc) and Pt/C in O<sub>2</sub>-saturated 0.1 M KOH at 1600 rpm and 10 mV/s. The kinetic current at 0.9 V vs. RHE was calculated based on the Levich equation:

$$\frac{1}{i} = \frac{1}{i_k} + \frac{1}{i_D} = \frac{1}{i_k} + \frac{1}{Bc_0\omega^{1/2}} \quad [3.1]$$

The kinetic currents were then normalized to the electrochemical surface area to obtain the specific activity and, in case of Pt/C also to the Pt mass to obtain the mass activity.

### **3.2.4 Impedance Measurements**

The cell resistance was measured immediately after RDE measurements using VoltaMaster (Votlab), taking the AC impedance spectra from 32 KHz to 0.1 KHz and a voltage perturbation of 10 mV. The real part of the resistance at 1 kHz was taken as the cell resistance and used to obtain the  $iR$ -free potential of the working electrode. The solution resistances at 275 K at 314 K measured were 65 and 35  $\Omega$ , respectively. These rather high non-compensated solution resistances in the relatively conductive 0.1 M KOH are due to the highly skewed potential distribution in the vicinity of the rotating disk electrode surface<sup>28</sup>, with half of the potential drop in the electrolyte phase occurring at a distance of only a disk radius from the disk surface.

### 3.3 Results

#### **3.3.1 Measurements of HOR/HER kinetics of Polycrystalline Pt**

The cyclic voltammogram of a polycrystalline Pt disk in 0.1 M KOH, Figure 3.1, shows the typical Pt-H underpotential deposition region (0.08 – 0.5 V), double layer region (0.5 – 0.6 V), and Pt-oxide region (above 0.6 V), similar to that reported previously.<sup>29</sup> The Pt-H peaks at ~0.3 V and ~0.4 V can be attributed to the Pt-H interaction on Pt (110) and Pt (100) planes, respectively, based on the cyclic voltammograms of Pt single crystal surfaces in 0.1 M KOH.<sup>20, 21</sup> To determine the Pt surface area, the positive potential window was restricted to 0.6 V in order to eliminate the interference from Pt oxide reduction in quantifying the double-layer contribution to the H-adsorption/desorption region. The Pt surface area was then obtained by integrating the H-adsorption/desorption region, subtracting the double-layer charging currents, dividing the resulting coulombic charge by two and  $210 \mu\text{C}/\text{cm}^2_{\text{Pt}}$ .<sup>23, 29</sup> The thus obtained roughness factor of the Pt(pc) disk from four independent experiments, which was defined as  $\text{ESA}/\text{area}_{\text{disk}}$ , was  $\sim 1.6 \pm 0.2 \text{ cm}^2_{\text{Pt}}/\text{cm}^2_{\text{disk}}$ .

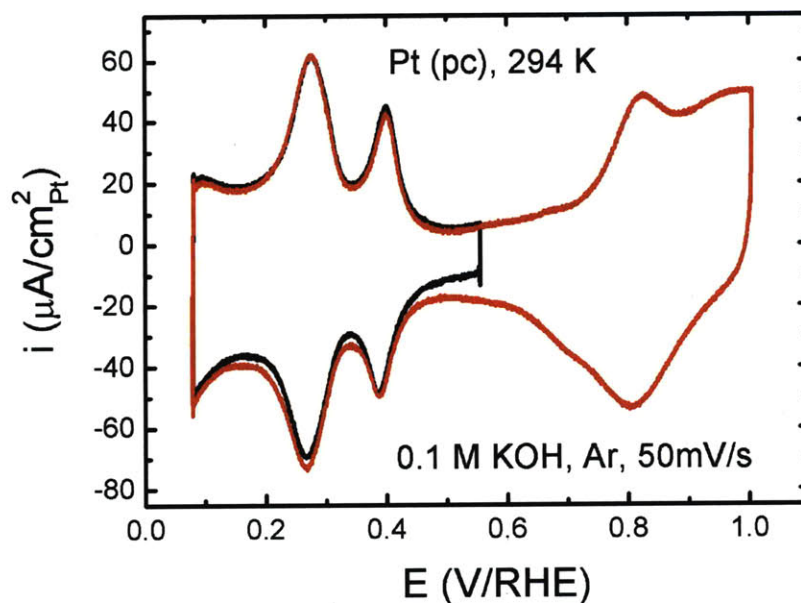


**Figure 3.1.** Cyclic voltammograms of Pt(pc) at  $294 \pm 1.5$  K in Ar-saturated 0.1 M KOH at 50 mV/s with two different positive potential limits. The current density is referenced to the actual Pt surface area.

Figure 3.2a shows the HOR/HER polarization curves on Pt(pc) in 0.1 M KOH at 294 K as a function of rotation rate, with well-defined hydrogen mass transport controlled (limiting) current densities occurring at potentials above 0.2 V/RHE. They scale linearly with the inverse of the square root of the rotation rate as shown by the Koutecky-Levich plot constructed at 0.5 V/RHE (see inset of Figure 3.2a), yielding a zero y-axis intercept and a  $Bc_0$  value (see Eq. 3.1) of  $0.0664 \text{ mA}/(\text{cm}^2_{\text{disk}} \cdot \text{rpm}^{0.5})$ . The limiting current density of  $3.31 \text{ mA}/\text{cm}^2_{\text{disk}}$  at 2500 rpm is in excellent agreement with the value obtained in a Teflon<sup>®</sup> cell<sup>26</sup>, where it was shown that impurities derived from KOH-induced glass corrosion would lead to substantially lower limiting current densities. In addition, our measured HOR half wave potential of 0.065 V/RHE on Pt(pc) at 2500 rpm and 294 K (Figure 3.2a) is actually slightly higher than that of 0.08 V/RHE obtained in a Teflon<sup>®</sup>



cell<sup>26</sup> at essentially the same conditions. The identical diffusion limited current densities and the slightly higher HOR activity in our study compared to the data reported for measurements in a Teflon<sup>®</sup> cell<sup>26</sup> clearly proves that there is no contamination by glass corrosion products in our experiments, which was accomplished by the short exposure time and the elimination of the vycor frit from the Luggin capillary.

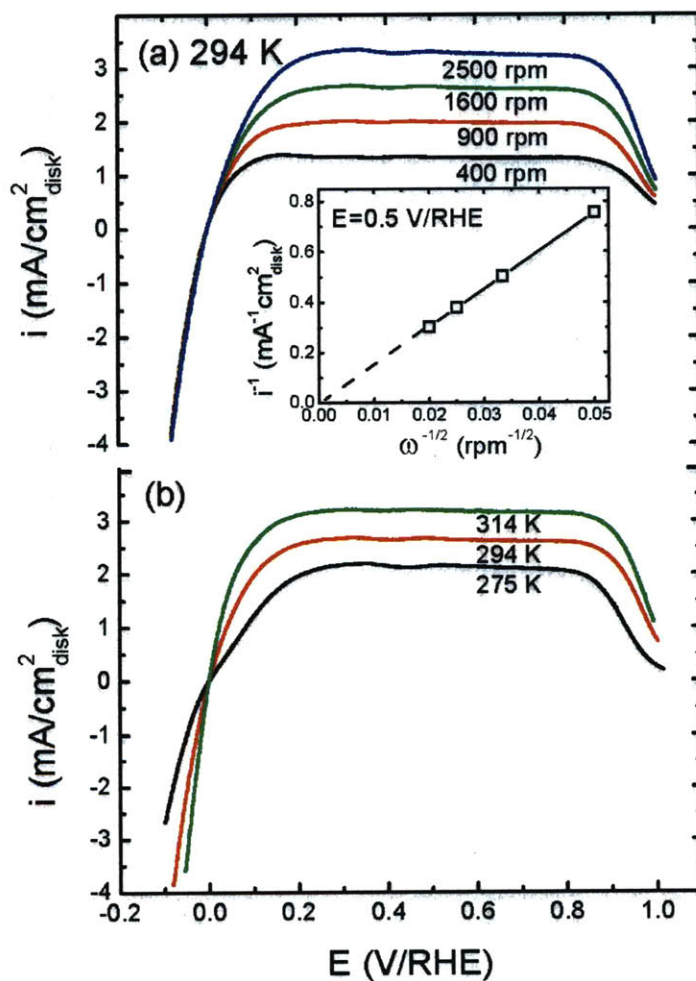


**Figure 3.2.** (a) HOR/HER polarization curves (positive-going scans) on Pt(pc) at different rotation rates at  $294 \pm 1.5$  K. The inset shows a Koutecky-Levich plot at 0.5 V/RHE. (b) HOR/HER polarization curves on Pt(pc) at 1600 rpm at different temperatures (positive-going scans). The data were collected in H<sub>2</sub>-saturated 0.1 M KOH at 10 mV/s.

The temperature dependence of the HOR limiting current densities is shown in Figure 3.2b, illustrating the previously reported observation of decreasing HOR limited current densities with decreasing temperatures. The limiting current of  $2.14 \text{ mA/cm}^2_{\text{disk}}$  at 275 K and 1600 rpm in Figure 3.2b is in good agreement with that reported for Pt(hkl) single crystals at 275 K.<sup>20</sup>

The HOR/HER kinetic current densities,  $i_k$ , on Pt(pc) are shown as a grey solid line in Figures 3.3a (at 275 K) and 3.3b (at 314 K), which were obtained from correcting the polarization curves by the measured  $iR$  resistance and the hydrogen mass transport in the HOR branch (Eq. 3.1). The voltage corrections associated with the  $iR$  resistances can be quite substantial at the higher end of the current density scale, amounting to, for example, 25 mV (275 K) and 12 mV (314 K) at  $2 \text{ mA/cm}^2_{\text{disk}}$ , as shown in the insets in Figure 3.3a and 3.3b. Following the  $iR$ -correction, the HOR/HER kinetic current densities were obtained by hydrogen mass transport resistance correction for the HOR branch using the Levich equation (Eq. 3.1). Only data below 80% of the HOR diffusion limited current density were used in order to minimize errors in the analysis, which can become substantial as the measured current approaches the mass transport limited current. Since hydrogen oversaturation and bubble formation can introduce mass transport resistances for the HER at high current densities, only data with HER current densities equal to or lower than  $-2 \text{ mA/cm}^2_{\text{disk}}$  were used, where no bubble formation was observed and where the measured current was rotation rate independent (between 900 and 2500 rpm). The thus obtained HOR/HER kinetic current densities,  $i_k$ , on Pt(pc) were then plotted in Figure 3.3 (grey solid line) at 275 K (a) and 314 K (b).

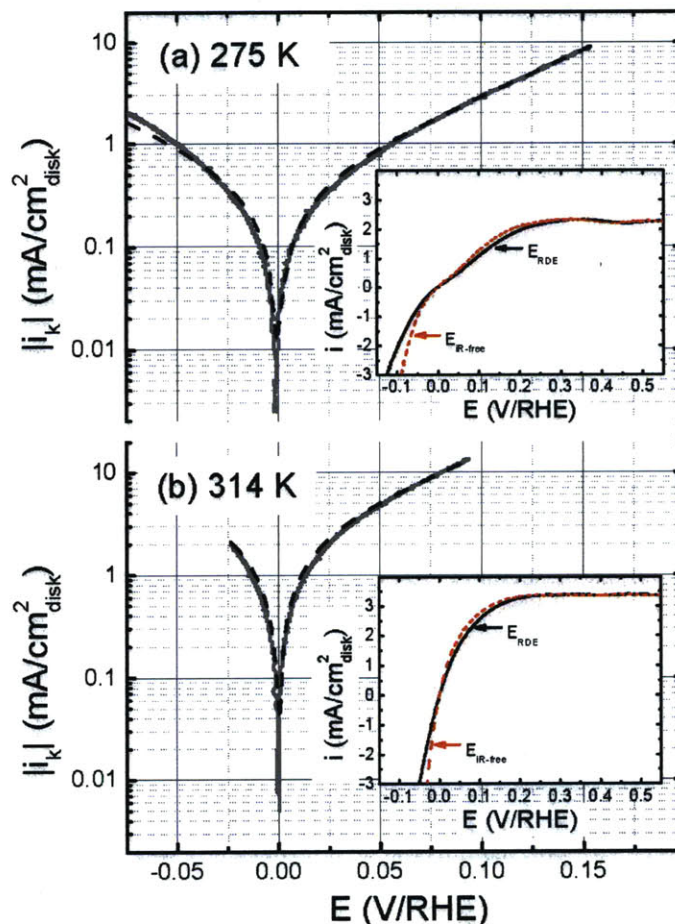


**Figure 3.3.** HOR/HER measured kinetic current densities (grey solid line) on Pt(pc) in 0.1 M KOH at 10 mV/s and their fit to the Butler-Volmer equation (see Eq. 3.2) with  $\alpha=0.5$  (dashed black line): **(a)** at 275 K; **(b)** at 314 K. The HOR/HER kinetic current densities were obtained from  $iR$ -corrected polarization curves and are corrected for hydrogen mass transport in the HOR branch using Eq. 3.1. The corresponding insets show the HOR/HER polarization curves before (solid black line) and after (dashed red line)  $iR$  correction.

The HOR/HER exchange current densities,  $i_0$ , on Pt(pc) were extracted subsequently by fitting the HOR/HER kinetic current densities to the Butler-Volmer equation (dashed black line in Figures 3.3a and 3.3b) as a function of the HOR/HER overpotential,  $\eta$ ,

$$i_k = i_0 \left[ e^{\frac{\alpha F}{RT} \eta} - e^{-\frac{(1-\alpha)F}{RT} \eta} \right] \quad [3.2]$$

where  $\alpha$  represents the transfer coefficient,  $F$  is the Faraday constant (96485 As/mol),  $R$  is the universal gas constant (8.314 J/mol/K), and  $T$  is the temperature in Kelvin. In fitting all the HOR/HER data in this study,  $\alpha$  and  $i_0$  were first set as variables, where we found that the best fit was obtained for  $\alpha=0.5$ . Therefore, the reported  $i_0$  values herein were obtained by setting  $\alpha =0.5$ . It can be seen in Figure 3.3 that the simple Butler-Volmer equation with  $\alpha =0.5$  perfectly fits the experimental HOR/HER kinetics on Pt(pc) at both 275 K and 314 K, but equally good fits were obtained at intermediate temperatures, corresponding to Tafel slopes defined as  $TS=2.303 \cdot RT/(\alpha F)$  with values of 109 mV/dec at 275 K and 125 mV/dec at 314 K. The symmetry of the anodic (HOR) and cathodic (HER) current densities with respect to the reversible potential suggests that the HOR and HER have the same reaction mechanism and intermediates, which will be discussed in more details later. It should be noted that the above determined potential-independent Tafel slopes of  $\sim 120$  mV/dec disagree with the variable Tafel slopes ranging from  $\sim 50$  mV/dec to  $\sim 150$  mV/dec at low and high overpotentials, respectively, reported for the HOR/HER on Pt(hkl) in 0.1 M KOH.<sup>20, 21</sup> However, the origin of this discrepancy is simply a misinterpretation of the definition of the Tafel slope, since the latter can only be obtained from a plot of  $\log(i_k)$  vs.  $\eta$  only if  $\eta$  is significantly larger in value than roughly one half of the Tafel slope<sup>30</sup>, so that the fitting of a Tafel slope to the low overpotential region in these studies<sup>20, 21</sup> is incorrect. Consequently, only their reported value of  $\sim 150$  mV/dec at high overpotentials is determined correctly and, is reasonably close to the Tafel slope obtained in our work.

Based on fitting at least three independent datasets at each temperature, specific HOR/HER exchange current densities of Pt (pc), normalized to the Pt ESA, are  $0.25\pm 0.01$ ,  $0.69\pm 0.01$  and  $1.26\pm 0.30$  mA/cm<sup>2</sup><sub>Pt</sub> at 275, 294, and 314 K, respectively. At 294 K, our value of  $0.69$  mA/cm<sup>2</sup><sub>Pt</sub> (listed in Table 3.1) is larger than the  $\sim 0.1$  mA/cm<sup>2</sup><sub>Pt</sub> reported for Pt(pc) in 0.5 M NaOH<sup>17</sup> and for Pt(110), which was the most active surface for the HOR/HER amongst the three low-index Pt single-crystal faces reported in an early study<sup>21</sup>. The origin of this discrepancy is likely caused by both the lack of *iR*-correction in these studies and electrolyte contamination effects, which is supported by the fact that the more recently measured HOR/HER specific exchange current density on Pt(110) at 293 K of  $0.6$  mA/cm<sup>2</sup><sub>Pt</sub><sup>20</sup> is much larger and comparable to our value on Pt(pc) (note that the exchange current density given in the reference<sup>20</sup> must be multiplied by a factor of two in order to be consistent with the definition used in Eq. 3.2 here). In addition, the activation energy of the HOR/HER on Pt(pc) was obtained by plotting  $i_0$  versus  $1/T$ , where a linear relationship was found between 275 and 314 K. A representative data set is shown in Figure 3.4. Based on four independent sets of repeat measurements, the HOR/HER activation energy,  $E_a$ , on Pt(pc) was determined to be  $28.9\pm 4.3$  kJ/mol, which is listed in Table 3.1. This value is in reasonably good agreement with 23 kJ/mol obtained for Pt(110) in the same electrolyte.<sup>20</sup>

**Table 3.1.** Average HOR/HER exchange current densities ( $i_0$ ) and mass activity ( $i_{0,m}$ ) at  $294 \pm 1.5$  K for Pt(pc) and Pt/C in 0.1 M KOH. Activation energies ( $E_a$ ) were obtained by fitting the data between  $275 \pm 1.5$  K and  $314 \pm 1.5$  K (see Figure 3.4). Data were  $iR$ - and mass-transport corrected as described in the text.

	$i_{0, 294 K}$ (mA/cm <sup>2</sup> <sub>Pt</sub> )	$i_{0,m, 294K}$ (A/mgPt)	$E_a$ (kJ/mol)
Pt(pc)	$0.69 \pm 0.03$ (4 <sup>*</sup> )	-	$28.9 \pm 4.3$ (4 <sup>*</sup> )
Pt/C	$0.57 \pm 0.07$ (2 <sup>*</sup> )	$0.35 \pm 0.05$ (2 <sup>*</sup> )	$29.5 \pm 4.0$ (2 <sup>*</sup> )

Notes: #<sup>\*</sup> indicates number of independent repeat experiments.

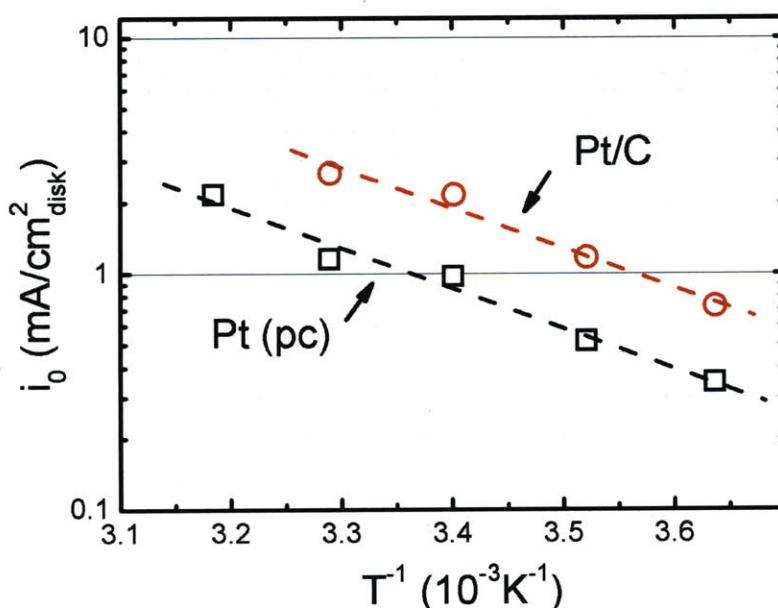


**Figure 3.4.** Representative Arrhenius plots of the HOR/HER exchange current densities on Pt(pc) (black squares) and Pt/C (red circles) in 0.1 M KOH. The calculated HOR/HER activation energies,  $E_a$ , are  $28.9 \pm 4.3$  kJ/mol for Pt(pc) and  $29.5 \pm 4.0$  kJ/mol for Pt/C based on four and two sets of repeat measurements, respectively.

### 3.3.2 Measurements of HOR/HER kinetics of Pt/C

The same HOR/HER electrochemical measurements as on Pt(pc) were made on Pt/C. Figure 3.5 depicts the cyclic voltammograms of Pt/C in 0.1 M KOH at 294 K and 50 mV/s, where current was normalized to the true Pt surface area. The observed

features resemble those of Pt(pc) except that it has higher currents in the double-layer region due to the capacitive contribution from the high surface area carbon support. Using the double-layer-corrected Pt-H underpotential deposition region, the specific surface area of Pt/C was determined to be  $62 \text{ m}^2/\text{g}_{\text{Pt}}$ , corresponding to a roughness factor of  $4.3 \text{ cm}^2_{\text{Pt}}/\text{cm}^2_{\text{disk}}$  for thin-film RDE electrodes of Pt/C.

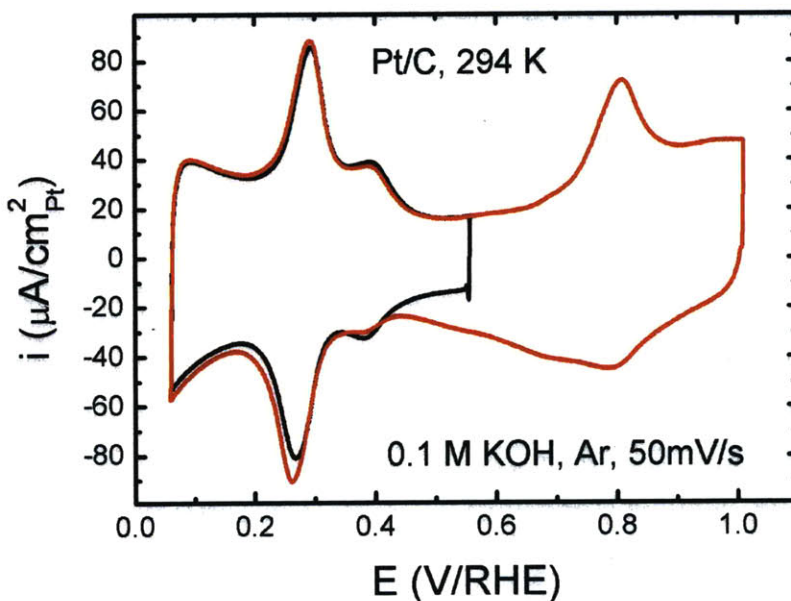


**Figure 3.5.** Cyclic voltammograms of Pt/C at  $294 \pm 1.5 \text{ K}$  in Ar-saturated  $0.1 \text{ M KOH}$  at  $50 \text{ mV/s}$  with two different positive potential limits. The current density is referenced to the actual Pt surface area.

HOR/HER kinetic current densities of Pt/C RDE electrodes are shown in Figure 3.6 and were extracted from HOR/HER polarization curves following processes analogous to what was used for Pt(pc) in Figure 3.3. It should be pointed out that the hydrogen transport limited current densities on Pt/C RDE electrodes (not shown) were within 10% of those shown for Pt(pc) in Figure 3.2. The fitting of the HOR/HER kinetic current densities using the Butler-Volmer equation with  $\alpha = 0.5$  was excellent, from

which the exchange current density  $i_0$  was obtained. The experimentally extracted and fitted kinetic current densities at 275 K and 304 K are shown in Figure 3.6 as examples while fits at intermediate temperatures (data not shown) are equally good. The specific exchange current density of the HOR/HER on Pt/C at 294 K was found to be  $0.57 \pm 0.07 \text{ mA/cm}^2_{\text{Pt}}$ , which is comparable to that obtained on Pt(pc) (see Table 3.1). Normalized to Pt mass, the mass exchange current density of Pt/C is  $0.35 \pm 0.05 \text{ A/mg}_{\text{Pt}}$ . A representative Arrhenius plot of  $i_0$  on Pt/C versus  $1/T$  ranging from 275 to 304 K is shown in Figure 3.4. Based on two independent repeat measurements, Pt/C has a HOR/HER activation energy of  $29.5 \pm 4.0 \text{ kJ/mol}$ , which is essentially identical to that on Pt(pc) (see Table 3.1) considering experimental uncertainty.



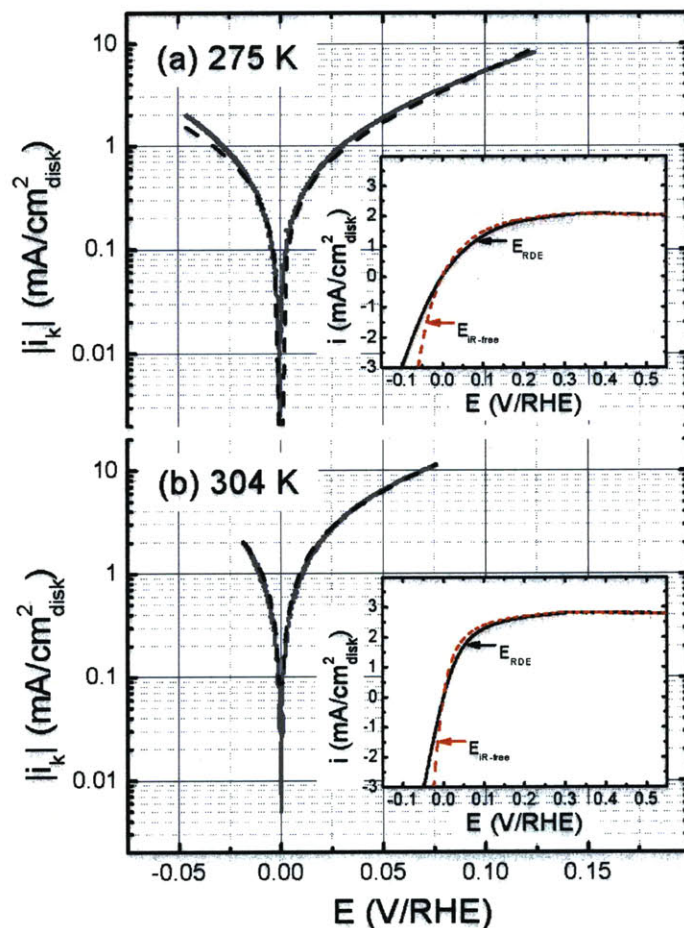


**Figure 3.6.** HOR/HER measured kinetic current densities (grey solid line) on Pt/C in 0.1 M KOH at 10 mV/s and their fit to the Butler-Volmer equation (see Eq. 3.2) with  $\alpha=0.5$  (dashed black line): **(a)** at 275 K; **(b)** at 314 K. The HOR/HER kinetic current densities were obtained from  $iR$ -corrected polarization curves and are corrected for hydrogen mass transport in the HOR branch using Eq. 3.1. The corresponding insets show the HOR/HER polarization curves before (solid black line) and after (dashed red line)  $iR$  correction.

The essentially identical specific exchange current densities, activation energies, and transfer coefficients for the HOR/HER on Pt(pc) and on Pt/C, and it is hypothesized that there is no *significant Pt particle-size effect* for the HOR/HER in 0.1 M KOH. Considering the roughly 10-fold lower specific exchange current densities reported for Pt(111) compared to Pt(110)<sup>20</sup>, future studies on Pt nanoparticles of different shapes are

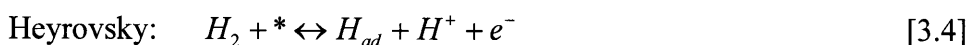
needed to examine this hypothesis further. To our knowledge, the HOR/HER kinetics on Pt/C in alkaline electrolytes have never been reported before, and this is the first comparison of the HOR/HER kinetics of polycrystalline Pt with that of Pt nanoparticles.

### 3.4 Discussion

#### 3.4.1 Comparing HOR/HER kinetic data with proposed mechanisms in alkaline electrolyte

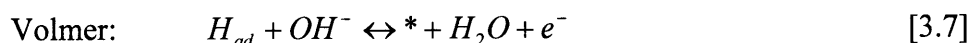
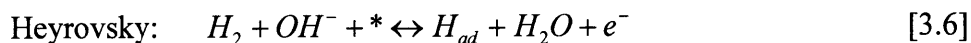
Due to the experimental difficulties of measuring the kinetic reaction rates of very fast reactions, the HOR/HER mechanism on Pt still remains inconclusive and under active investigation. This is particularly true for HOR/HER in acid as some authors argue that the rate of the HOR/HER is so high that conventional RDE measurements cannot provide sufficiently high hydrogen mass-transport rates, which would be required to unambiguously quantify kinetic rates of the HOR/HER<sup>12, 17</sup> (this will be discussed in more detail below).

Nevertheless, it is widely accepted that the HOR/HER proceeds through a combination of several of the following elementary steps: the dissociative adsorption of H<sub>2</sub> without electron transfer (Tafel reaction, see Eq. 3.3) or with simultaneous electron transfer (Heyrovsky reaction, Eq. 3.4) and the discharge of adsorbed hydrogen, H<sub>ad</sub>, (Volmer reaction, Eq. 3.5), whereby \* represents an adsorption site on Pt.<sup>31-33</sup>





While the Heyrovsky and Volmer reactions as written above apply for the HOR/HER in acidic electrolytes, they can also be written for the reactions occurring in alkaline solution.<sup>31</sup>



The possible HOR/HER mechanisms based on these three elementary reactions are thus the Tafel-Volmer (Eqs. 3.3+3.5 or 3.3+3.7) or the Heyrovsky-Volmer (Eqs. 3.4+3.5 or 3.6+3.7) reaction sequence. The most simple kinetic HOR/HER models assume that one of the reactions in each of the two reaction sequences are rate-determining steps (rds),<sup>31, 33</sup> which leads to four limiting cases: Tafel-Volmer(rds), Heyrovsky-Volmer(rds), Heyrovsky(rds)-Volmer, and Tafel(rds)-Volmer.

In the following we review and discuss the kinetic HOR/HER expressions for the first two cases (Volmer reaction being rds) in alkaline solution, which was first derived by Vetter.<sup>31</sup> The anodic reaction rate of Eq. 3.7 is proportional to the surface coverage of  $H_{ad}$ ,  $\theta_H$ , and the activity of  $OH^-$  while the cathodic reaction rate is proportional to the coverage of unoccupied surface sites,  $1 - \theta_H$ , as well as the activity of  $H_2O$ . Using the Butler-Volmer equation (Eq. 3.2) to describe this elementary reaction step, the kinetic expression can be written as:

$$i_k = k_+ \theta_H a_{OH^-} \exp\left[\frac{\alpha F}{RT} \varepsilon_V\right] - k_- (1 - \theta_H) a_{H_2O} \exp\left[\frac{-(1 - \alpha) F}{RT} \varepsilon_V\right] \quad [3.8]$$

where  $\varepsilon_V$  represents the half-cell potential across the solid/liquid interface measured against an arbitrary reference electrode. At the reversible potential of the Volmer reaction,  $\varepsilon_{0,V}$ , Eq. 3.8 can be re-written as:

$$i_{0,V} = k_+ \theta_H^0 a_{OH^-} \exp\left[\frac{\alpha F}{RT} \varepsilon_{0,V}\right] = k_- (1 - \theta_H^0) a_{H_2O} \exp\left[\frac{-(1 - \alpha)F}{RT} \varepsilon_{0,V}\right] \quad [3.9]$$

where  $i_{0,V}$  is the exchange current density of the Volmer reaction. Dividing Eq. 3.8 by Eq. 3.9 yields:

$$i_k = i_{0,V} \left\{ \frac{\theta_H}{\theta_H^0} \exp\left[\frac{\alpha F}{RT} (\varepsilon - \varepsilon_{0,V})\right] - \frac{1 - \theta_H}{1 - \theta_H^0} \exp\left[\frac{-(1 - \alpha)F}{RT} (\varepsilon - \varepsilon_{0,V})\right] \right\} \quad [3.10]$$

In the assumed case that the Volmer reaction is the rds and  $(\varepsilon - \varepsilon_{0,V})$  corresponds to the overpotential,  $\eta$ , of overall HOR/HER. Furthermore, if the HOR/HER kinetics are measured in a reasonably narrow potential range (e.g., from -0.075 to +0.15 V in our study), the variation in  $\theta_H$  is small (i.e.,  $\theta_H \approx \theta_H^0$ ). To a first approximation, the terms  $\theta_H/\theta_H^0$  and  $(1 - \theta_H)/(1 - \theta_H^0)$  can be approximated to be one, as the potential-dependence of the exponential terms influence kinetic current densities much more strongly. Thus, Eq. 3.10 can be approximated as:

$$i_k = i_{0,V} \left\{ \exp\left[\frac{\alpha F}{RT} \eta\right] - \exp\left[\frac{-(1 - \alpha)F}{RT} \eta\right] \right\} \quad [3.11]$$

Formally, Eq. 3.11 is equivalent to the Butler-Volmer equation (Eq. 3.2), which was used to fit the HOR/HER kinetic current densities in our study, providing an excellent fit with all the experimental data (see Figures 3.3 and 3.6).

An analogous derivation assuming the Heyrovsky reaction to be the rds is given in Reference<sup>31</sup>, yielding the same expression as Eq. 3.11 in the limit that  $\theta_H \approx \theta_H^0$ . Therefore, the Butler-Volmer equation given by Eq. 3.11 will describe the HOR/HER kinetics in the vicinity of the HOR/HER equilibrium potential for three of the four limiting cases, i.e., for the Tafel-Volmer(rds), Heyrovsky-Volmer(rds), and Heyrovsky(rds)-Volmer mechanisms<sup>31, 33</sup>. A very different kinetic expression is obtained only for the Tafel(rds)-Volmer mechanism<sup>31, 33</sup>, so that it can be excluded as possible HOR/HER mechanism in alkaline electrolytes on the basis of our measurements.

In recent density functional theory (DFT) calculations, a Tafel-Volmer mechanism was assumed and successfully described the HER activity trends of a wide range of metal catalysts in acid electrolyte.<sup>34</sup> It should be noted this and later DFT<sup>32</sup> calculations nominally evaluated for pH zero, should apply equally to alkaline pH, as long as the potential scale is referenced to RHE. In the later DFT study by the same group on the HER mechanism on Pt(111),<sup>32</sup> however, it was concluded that the activation barrier at zero overpotential of the Volmer reaction ( $\sim 0.15$  eV) is substantially lower than that of the Tafel ( $\sim 0.8$  eV) and Heyrovsky ( $\sim 0.6$  eV) reactions, suggesting that either one or both of the latter reactions would be rds. The calculated transfer coefficients for the Tafel and Heyrovsky reactions were  $\alpha=0.64$  and  $\alpha=0.45$ , respectively.<sup>32</sup> One major discrepancy between experimental data and their DFT calculations noted by the authors is the fact that the calculated activation barriers (0.6 to 0.8 eV) are so much larger than the experimentally reported activation energies on Pt(hkl) in acid electrolytes ( $<0.2$  eV<sup>14</sup>) measured via RDE. As will be argued below, meaningful HOR/HER kinetics in acid electrolyte cannot be obtained by RDE measurements, so that these experimental

activation energies are not meaningful. On the other hand, experimental RDE-based activation energies in 0.1 M KOH, where the HOR/HER kinetics are slow should be reliable and, indeed, the value of  $\sim 0.5$  eV on Pt(111) in 0.1 M KOH reported by Schmidt et al.<sup>20</sup> is quite comparable with the DFT-based values considering the expected uncertainties of the latter. If one were to assume that the basic learnings from the DFT model<sup>32</sup> are correct, i.e, that the Volmer reaction would have the lowest activation barrier and that the Heyrovsky reaction would have a transfer coefficient of  $\alpha=0.45$ , our experimental observation that the HOR/HER on Pt in 0.1 M KOH can be described by a simple Butler-Volmer equation with  $\alpha =0.5$ , would favor the Heyrovsky(rds)-Volmer mechanism. However, this hypothesis is very tentative. Further experimental studies on the effect of pH and the partial pressure of H<sub>2</sub> on the HOR/HER kinetics should be carried out to explore its mechanism in more detail.

### **3.4.2 Comparing HOR/HER kinetics in Acid with Alkaline Electrolyte**

Although HOR/HER kinetics on Pt in alkaline can be measured accurately from conventional RDE measurements with  $iR$  correction, we here compare HOR/HER kinetics in acid and alkaline, and show that the HOR/HER kinetics on Pt in acid cannot be separated from the hydrogen diffusion overpotential in RDE measurements due to the very fast reaction rate. To illustrate this point, we conducted RDE measurements of the HOR/HER on Pt(pc) in 0.1 M HClO<sub>4</sub>, including appropriate correction of the non-compensated solution resistance measured by AC impedance. Figure 3.7a shows the polarization curve of the HOR/HER on the Pt(pc) electrode at 1600 rpm and 294 K before (solid black line) and after (dotted red line)  $iR$  correction, and the Koutecky-

Levich plot demonstrates that hydrogen mass transport limited current densities are obtained at already 0.1 V/RHE. The dashed black line represents the calculated Nernstian diffusion overpotential,  $\eta_{diffusion}$ , assuming ideal reversibility of the HOR/HER, i.e, infinitely fast reaction kinetics:<sup>22, 31</sup>

$$\eta_{diffusion} = \frac{RT}{2F} \ln \left( 1 - \frac{i}{i_{\infty}} \right) \quad [3.12]$$

where  $i_{\infty}$  is the hydrogen diffusion limited current density. Clearly, after  $iR$  correction, the experimental current densities of the HOR/HER are indistinguishable from the Nernstian diffusion overpotential and since the latter assumes infinitely fast reaction kinetics, it is clear that it is not reasonable to attempt to extract kinetic rates for the HOR/HER on Pt in acid using the RDE method, consistent with previous conclusions.<sup>17</sup> Consequently, the several orders of magnitude lower HOR/HER exchange current density values from RDE measurements (0.1 to 1 mA/cm<sup>2</sup><sub>Pt</sub><sup>13, 14, 35</sup>) compared to those obtained from micro-electrode<sup>16, 17</sup> or gas-diffusion electrode<sup>12, 18</sup> measurements is caused both by the rather low hydrogen diffusion limited current densities in the RDE configuration (on the order of several mA/cm<sup>2</sup><sub>disk</sub>) as well as by the lack of  $iR$ -correction. In other words, kinetic currents cannot be measured with reasonable precision if the exchange current density is one or two orders of magnitude larger than the diffusion limited current density. Consequently, many RDE-based studies on the HOR/HER on Pt in acid electrolyte report Tafel slope values in the vicinity of  $TS=2.303 \cdot RT/(2F)$ <sup>14, 35</sup>, which simply reflects the apparent Tafel slope of the Nernstian diffusion overpotential (Eq. 3.12). Finally, it should be mentioned that, based on RDE and micro-electrode data for the HOR on Pt in acid electrolytes, Wang et al.<sup>36</sup> recently developed a complex

kinetic model which suggests that the HOR proceeds through parallel Heyrovsky-Volmer and Tafel-Volmer mechanisms. However, considering the difficulty of extracting HOR kinetics on Pt in acid electrolyte from RDE measurements, the complexity of the model is perhaps not warranted by the uncertainties associated with available electrochemical data.

On the other hand, the  $iR$ -corrected polarization curve of the HOR/HER on Pt(pc) in 0.1 M KOH under the same experimental conditions deviates substantially from the Nernstian diffusion overpotential, as demonstrated in Figure 3.7b. This is caused by the much slower HOR/HER kinetics on Pt in KOH, so that the diffusion-limited current density is only reached at  $\sim 0.25$  V/RHE (note that the diffusion limited current densities are essentially the same in both 0.1 M KOH and 0.1 M HClO<sub>4</sub>). Since the difference between the Nernstian diffusion overpotential relationship and the experimental data in KOH is very large, kinetic parameters for the HOR/HER can be extracted easily without interference from mass transport resistances. As was shown, this is not the case in acidic electrolyte (see Figure 3.7a), which is the reason why reliable HOR/HER kinetics on Pt with the RDE method can be obtained in alkaline but not in acid electrolytes. The fact that the HOR/HER kinetics on Pt are slower in alkaline compared to acid electrolyte was noted before<sup>17</sup>, but, its cause remains unclear and, as discussed, is not captured in recent DFT models of the HER<sup>6</sup>. Recent theoretical calculations<sup>37-39</sup> about the HOR in acid and alkaline solution suggest that the bond distance between Pt surface atoms and H<sub>ad</sub> intermediates is shorter in alkaline than in acid electrolyte, which would imply a stronger Pt-H binding energy in alkaline electrolyte, which in principle could result in lower HOR/HER kinetics<sup>34</sup>.



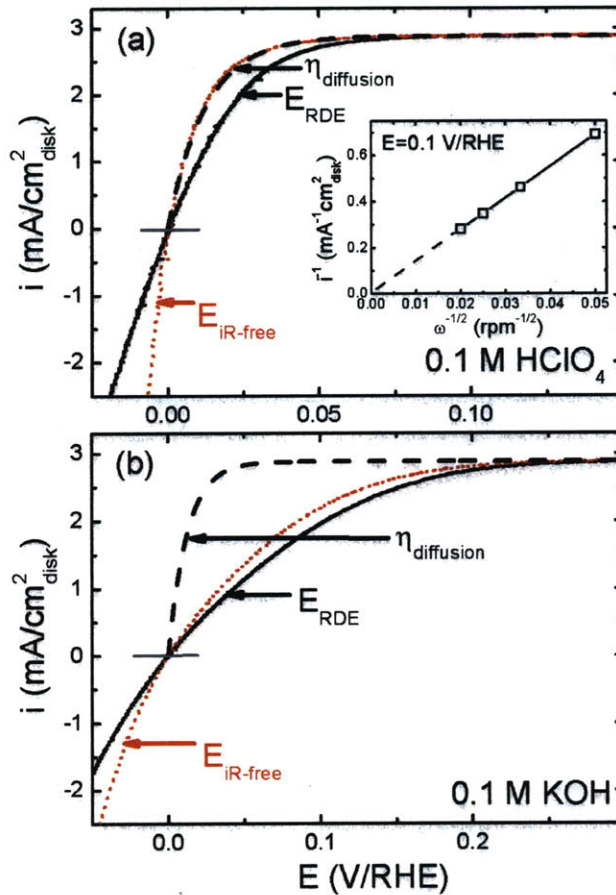


**Figure 3.7.** (a) HOR/HER polarization curve on Pt(pc) in 0.1 M HClO<sub>4</sub> at 1600 rpm before ( $E_{RDE}$ , solid black line) and after ( $E_{iR-free}$ , dotted red line)  $iR$ -correction. The inset is the Koutecky-Levich plot obtained at  $E=0.1$  V/RHE for the HOR at different rotation rates. (b) HOR/HER polarization curve on Pt(pc) in 0.1 M KOH at 1600 rpm before ( $E_{RDE}$ , solid black line) and after ( $E_{iR-free}$ , dotted red line)  $iR$ -correction; the dashed black line is the Nernstian diffusion overpotential calculated according to Eq. 3.12. The data are shown for the positive-going scans at 10 mV/s at a temperature of  $294 \pm 1.5$  K. Note that the x-axis potential range in (b) is double of that in (a).

### 3.4.3 Predicted Performance of AFCs/AMFCs vs. PEMFCs using Pt/C

In this section, we estimate and compare the performance of AFCs and PEMFCs using Pt/C on the anode and cathode. We first examine the implications of the slow HOR/HER kinetics on Pt in alkaline electrolyte on the projected HOR overpotential in an AFC/AMFC using a Pt/C anode catalyst. In order to obtain the HOR/HER exchange

current density at the typical fuel cell temperature of 80 °C, we extrapolated our experimental  $i_0$ -values to 80 °C using the Arrhenius plot, as shown in Figure 3.8a. Quite clearly, the estimated specific exchange current density in alkaline electrolyte on Pt/C is at least two orders of magnitude lower than that reported for PEMFCs.<sup>12</sup> In order to predict the fuel cell relevant Pt mass activity in KOH as a function of overpotential, we then used the Butler-Volmer equation (Eq. 3.2) in combination with the specific surface area either of our 46%wt. Pt/C catalyst ( $62 \text{ m}^2/\text{g}_{\text{Pt}}$ ) or of the 5%wt. Pt/C catalyst tested in PEMFCs ( $92 \text{ m}^2/\text{g}_{\text{Pt}}$ ).<sup>12</sup> The resulting polarization curves in KOH are compared to that measured in PEMFCs,<sup>12</sup> which is shown in Figure 3.8b. Considering an envisaged anode catalyst loading of  $0.05 \text{ mg}_{\text{Pt}}/\text{cm}^2_{\text{anode}}$  and an operating current density of  $1.5 \text{ A}/\text{cm}^2_{\text{anode}}$ , corresponding to a required mass activity of  $30 \text{ A}/\text{mg}_{\text{Pt}}$ , Figure 3.8b illustrates that one would expect a hydrogen anode overpotential in an AFC/AMFC of 130 to 150 mV depending on the specific Pt surface area. This is in stark contrast to the negligibly small anode overpotential under the same conditions measured in a PEMFC. This projection clearly emphasizes that ultra-low Pt anode loadings are not feasible in AFCs/AMFCs (in contrast to PEMFCs) and that novel anode catalysts must be developed for these applications which have either much higher mass activity for PGM-based anodes or which are PGM-free.

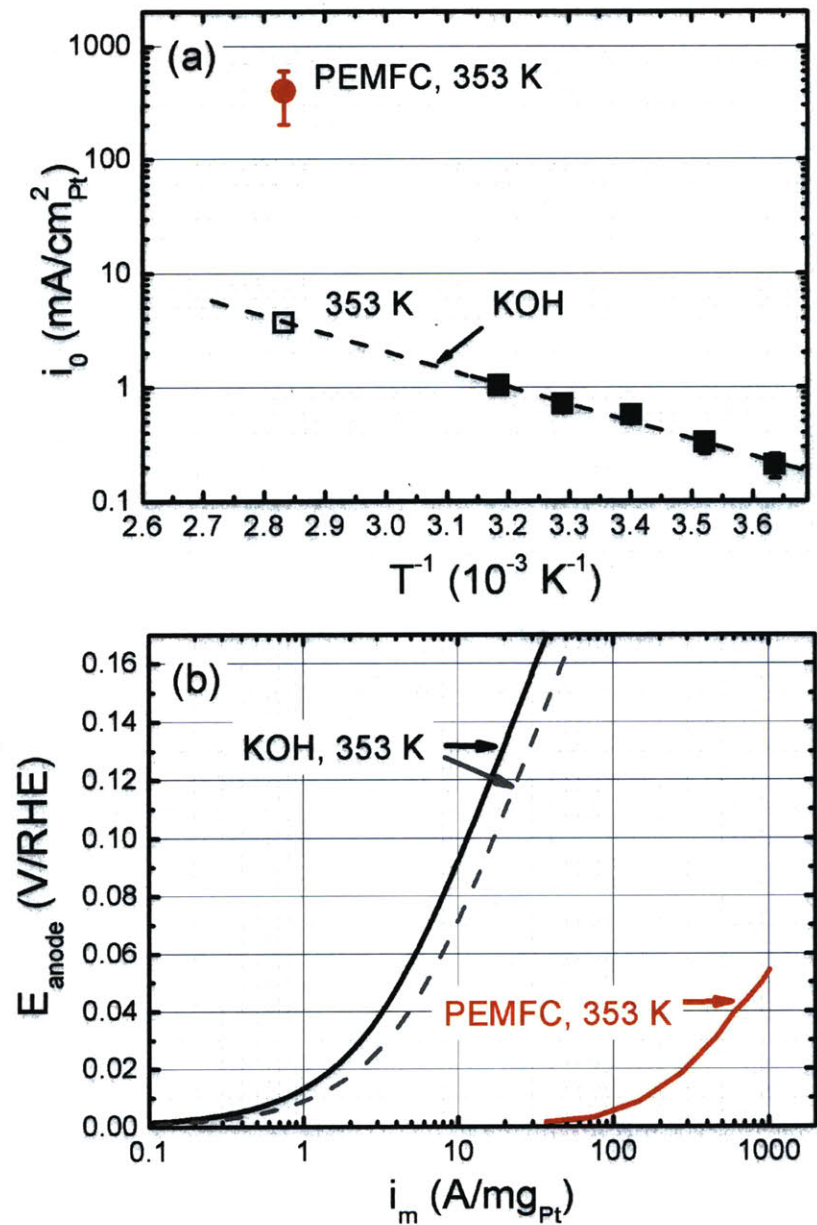


**Figure 3.8.** (a) HOR/HER specific exchange current density of Pt/C in a PEM fuel cell at 353 K and 101 kPa<sub>abs</sub> H<sub>2</sub> (solid circle, from reference<sup>12</sup>) compared to that obtained in 0.1 KOH in this study (solid squares) and extrapolated to 353 K (open square). (b) Projected HOR overpotential vs. Pt mass activity in KOH based either on 62 m<sup>2</sup>/g<sub>Pt</sub> for the 46%wt. Pt/C catalyst used in this study (black solid line) or on 92 m<sup>2</sup>/g<sub>Pt</sub> for the 5%wt. Pt/C catalyst used in reference<sup>12</sup> (grey dashed line); this is compared with mass activities measured on 5%wt. Pt/C in a PEMFC at 353 K (red line, from reference<sup>12</sup>).

Lastly we compare ORR kinetics of Pt/C in alkaline with that in acid, and discuss the implication in the performance of AFCs/AMFCs relative to PEMFCs. As Pt nanoparticles are shown to exhibit much lower ORR activity than Pt bulk surfaces in acid<sup>2, 40</sup>, we here examine the ORR specific activity of both Pt(pc) and Pt/C in 0.1 M KOH at 294 K and 100 kPa<sub>abs</sub> O<sub>2</sub>. The activities at 0.9 V/RHE are summarized in Table 3.2. The ORR activity of Pt(pc) is  $0.95 \pm 0.25$  mA/cm<sup>2</sup><sub>Pt</sub>, which is consistent with the value of  $\sim 0.8$  mA/cm<sup>2</sup><sub>Pt</sub> reported in a Teflon<sup>®</sup> cell<sup>26</sup> (confirming our measurements of ORR activity are free of glass-cell related contamination effects). Unlike HOR/HER kinetics on Pt, the ORR specific activity of Pt/C is roughly two times lower than that of Pt(pc) (see Table 3.2), indicating a Pt particle size effect on the ORR kinetics in alkaline. The ORR specific activities of Pt/C and Pt(pc), and the mass activities of Pt/C in 0.1 M KOH are identical to those in 0.1 M HClO<sub>4</sub> within the experimental error<sup>41</sup> (see Table 3.2). This is perhaps not surprising since the ORR rate-controlling formation of adsorbed oxygen-containing species, OH<sub>ad</sub>, occurs at essentially the same potential vs. RHE in both electrolytes<sup>42</sup>. For practical applications, the identical ORR activities in acid and base predict that the ORR overpotential on a Pt cathode in AFCs/AMFCs would be the same as that of PEMFC under the same conditions (i.e., under the same mass specific current density [A/g<sub>Pt</sub>], temperature, and oxygen partial pressure).

**Table 3.2.** ORR specific activity ( $i_{s,0.9V}$ ) and mass activity ( $i_{m,0.9V}$ ) at 0.9 V vs. RHE, 100 kPa<sub>abs</sub> O<sub>2</sub>, and 294 ± 1.5 K in 0.1 M KOH and 0.1 M HClO<sub>4</sub> for Pt(pc) and Pt/C. Data were obtained from the positive-going scans at 10 mV/s and were  $iR$ - and mass-transport corrected as described in the text.

	$i_{s,0.9V, 294K}$ (mA/cm <sup>2</sup> <sub>Pt</sub> ) in 0.1 M KOH	$i_{m,0.9V, 294K}$ (A/mg <sub>Pt</sub> ) in 0.1 M KOH	$i_{s,0.9V, 294K}$ (mA/cm <sup>2</sup> <sub>Pt</sub> ) in 0.1 M HClO <sub>4</sub>	$i_{m,0.9V, 294K}$ (A/mg <sub>Pt</sub> ) in 0.1 M HClO <sub>4</sub>
Pt(pc)	0.95 ± 0.25 (3 <sup>*</sup> )	-	1.27 ± 0.43 (2 <sup>*</sup> ) <sup>41</sup>	-
Pt/C	0.42 ± 0.01 (2 <sup>*</sup> )	0.26 ± 0.001(2 <sup>*</sup> )	0.45 ± 0.02 (5 <sup>*</sup> ) <sup>41</sup>	0.35 ± 0.01 (5 <sup>*</sup> ) <sup>41</sup>

Notes: #<sup>\*</sup> indicates number of independent repeat experiments.

### 3.5 Conclusions

Our RDE measurements show that the HOR/HER on Pt(pc) and Pt/C in alkaline electrolyte have very comparable specific exchange current densities (showing no size effect of HOR/HER on Pt) of ~0.6 mA/cm<sup>2</sup><sub>Pt</sub> at 294 K, and activation energies of ~29 kJ/mol. In addition, based on the fact that the kinetics of the HOR/HER in our study are very well described by the Butler-Volmer equation and considering recent DFT findings<sup>32</sup>, it is hypothesized that the mechanism of the HOR/HER in KOH may go through Heyrovsky-Volmer mechanism with the Heyrovsky step as the rate-determining step.

Analogous RDE measurements of the HOR/HER on Pt(pc) in 0.1 M HClO<sub>4</sub> clearly demonstrate that the HOR/HER current densities in acid solution simply follow the Nernstian hydrogen diffusion overpotential relationship, which is based on assuming reversible, i.e., infinitely fast HOR/HER kinetics. This implies that the HOR/HER exchange current densities in acid electrolyte are one or more orders of magnitude larger than the typical hydrogen diffusion limited current density, and can therefore not be quantified in RDE measurements. This finding is consistent with the much higher

HOR/HER exchange current densities in measurements based on micro-electrode or gas diffusion electrodes.

Our measurements and analysis suggests that the HOR/HER kinetics on Pt(pc) and Pt/C is several orders of magnitude slower in alkaline compared to acid electrolyte. Therefore, the use of Pt/C anode catalysts in AFCs/AMFCs would require high loadings, and thus become a significant cost factor unlike in PEMFCs, where very low Pt anode loadings are sufficient. On the other hand, the use of Pt/C cathode catalysts in AFCs/AMFCs would result in comparable ORR potential losses as in PEMFCs, but other non-noble metal based cathode catalysts are available for AMFCs/AFCs with ORR activity comparable to Pt/C. Therefore, the development of highly efficient catalysts towards HOR in alkaline electrolyte will be one of the critical challenges in order to make alkaline fuel cells more practical.

### 3.6 References

1. N. M. Markovic; Schmidt, T. J.; Stamenkovic, V.; Ross, P. N., Oxygen Reduction Reaction on Pt and Pt Bimetallic Surfaces: A Selective Review, *Fuel Cells*, **2001**, *1*, (2), 105-116.
2. Gasteiger, H. A.; Kocha, S. S.; Sompalli, B.; Wagner, F. T., Activity benchmarks and requirements for Pt, Pt-alloy, and non-Pt oxygen reduction catalysts for PEMFCs, *Applied Catalysis B-Environmental*, **2005**, *56*, (1-2), 9-35.
3. Mayrhofer, K. J. J.; Strmcnik, D.; Blizanac, B. B.; Stamenkovic, V.; Arenz, M.; Markovic, N. M., Measurement of oxygen reduction activities via the rotating disc electrode method: From Pt model surfaces to carbon-supported high surface area catalysts, *Electrochimica Acta*, **2008**, *53*, (7), 3181-3188.
4. Gu, W.; Baker, D. R.; Liu, Y.; Gasteiger, H. A., Proton Exchange Membrane Fuel Cell (PEMFC) Down-the-Channel Performance Model. In *Handbook of Fuel Cells - Fundamentals, Technology and Applications*, Vielstich, W.; Gasteiger, H. A.; Yokokawa, H.; Editors, Eds. Wiley: Chichester, 2009; Vol. 6, pp P. 631-657.
5. Neyerlin, K. C.; Gu, W. B.; Jorne, J.; Gasteiger, H. A., Determination of catalyst unique parameters for the oxygen reduction reaction in a PEMFC, *J. Electrochem. Soc.*, **2006**, *153*, (10), A1955-A1963.
6. Strmcnik, D.; Kodama, K.; van der Vliet, D.; Greeley, J.; Stamenkovic, V. R.; Markovic, N. M., The role of non-covalent interactions in electrocatalytic fuel-cell reactions on platinum, *Nature Chemistry*, **2009**, *1*, (6), 466-472.
7. Markovic, N. M.; Gasteiger, H. A.; Ross, P. N., Oxygen reduction on platinum low-index single-crystal surfaces in alkaline solution: Rotating ring disk(Pt(hkl)) studies, *Journal of Physical Chemistry*, **1996**, *100*, (16), 6715-6721.
8. Lima, F. H. B.; Zhang, J.; Shao, M. H.; Sasaki, K.; Vukmirovic, M. B.; Ticianelli, E. A.; Adzic, R. R., Catalytic activity-d-band center correlation for the O<sub>2</sub> reduction reaction on platinum in alkaline solutions, *Journal of Physical Chemistry C*, **2007**, *111*, (1), 404-410.
9. Meng, H.; Jaouen, F.; Proietti, E.; Lefevre, M.; Dodelet, J. P., pH-effect on oxygen reduction activity of Fe-based electro-catalysts, *Electrochemistry Communications*, **2009**, *11*, (10), 1986-1989.
10. Piana, M.; Catanorchi, S.; Gasteiger, H. A., Kinetics of Non-Platinum Group Metal Catalysts for the Oxygen Reduction Reaction in Alkaline Medium, *ECS Transactions*, **2008**, *16*, (2), 2045-2055.
11. Bidault, F.; Brett, D. J. L.; Middleton, P. H.; Brandon, N. P., Review of gas diffusion cathodes for alkaline fuel cells, *Journal of Power Sources*, **2009**, *187*, (1), 39-48.
12. Neyerlin, K. C.; Gu, W. B.; Jorne, J.; Gasteiger, H. A., Study of the exchange current density for the hydrogen oxidation and evolution reactions, *Journal of the Electrochemical Society*, **2007**, *154*, (7), B631-B635.
13. Maruyama, J.; Inaba, M.; Katakura, K.; Ogumi, Z.; Takehara, Z.-i., Influence of Nafion® film on the kinetics of anodic hydrogen oxidation, *Journal of Electroanalytical Chemistry*, **1998**, *447*, (1-2), 201-209.

14. Markovic, N. M.; Grgur, B. N.; Ross, P. N., Temperature-dependent hydrogen electrochemistry on platinum low-index single-crystal surfaces in acid solutions, *Journal of Physical Chemistry B*, **1997**, *101*, (27), 5405-5413.
15. Wang, J. X.; Brankovic, S. R.; Zhu, Y.; Hanson, J. C.; Adzic, R. R., Kinetic characterization of PtRu fuel cell anode catalysts made by spontaneous Pt deposition on Ru nanoparticles, *Journal of the Electrochemical Society*, **2003**, *150*, (8), A1108-A1117.
16. Chen, S. L.; Kucernak, A., Electrocatalysis under conditions of high mass transport: Investigation of hydrogen oxidation on single submicron Pt particles supported on carbon, *Journal of Physical Chemistry B*, **2004**, *108*, (37), 13984-13994.
17. Bagotzky, V. S.; Osetrova, N. V., Investigations of hydrogen ionization on platinum with the help of micro-electrodes, *Journal of Electroanalytical Chemistry*, **1973**, *43*, (2), 233-249.
18. Vogel, W.; Lundquist, L.; Ross, P.; Stonehart, P., Reaction pathways and poisons-II: The rate controlling step for electrochemical oxidation of hydrogen on Pt in acid and poisoning of the reaction by CO, *Electrochimica Acta*, **1975**, *20*, (1), 79-93.
19. Gasteiger, H. A.; Panels, J. E.; Yan, S. G., Dependence of PEM fuel cell performance on catalyst loading, *Journal of Power Sources*, **2004**, *127*, (1-2), 162-171.
20. Schmidt, T. J.; Ross, P. N.; Markovic, N. M., Temperature dependent surface electrochemistry on Pt single crystals in alkaline electrolytes Part 2. The hydrogen evolution/oxidation reaction, *Journal of Electroanalytical Chemistry*, **2002**, *524*, 252-260.
21. Markovic, N. M.; Sarraf, S. T.; Gasteiger, H. A.; Ross, P. N., Hydrogen electrochemistry on platinum low-index single-crystal surfaces in alkaline solution, *Journal of the Chemical Society-Faraday Transactions*, **1996**, *92*, (20), 3719-3725.
22. Gasteiger, H. A.; Markovic, N. M.; Ross, P. N., H<sub>2</sub> and Co Electrooxidation on Well-Characterized Pt, Ru, and Pt-Ru .1. Rotating-Disk Electrode Studies of the Pure Gases Including Temperature Effects, *Journal of Physical Chemistry*, **1995**, *99*, (20), 8290-8301.
23. Schmidt, T. J.; Gasteiger, H. A.; Stab, G. D.; Urban, P. M.; Kolb, D. M.; Behm, R. J., Characterization of high-surface area electrocatalysts using a rotating disk electrode configuration, *Journal of the Electrochemical Society*, **1998**, *145*, (7), 2354-2358.
24. Paulus, U. A.; Wokaun, A.; Scherer, G. G.; Schmidt, T. J.; Stamenkovic, V.; Radmilovic, V.; Markovic, N. M.; Ross, P. N., Oxygen reduction on carbon-supported Pt-Ni and Pt-Co alloy catalysts, *Journal of Physical Chemistry B*, **2002**, *106*, (16), 4181-4191.
25. Mayrhofer, K. J. J.; Crampton, A. S.; Wiberg, G. K. H.; Arenz, M., Analysis of the impact of individual glass constituents on electrocatalysis on Pt electrodes in alkaline solution, *Journal of the Electrochemical Society*, **2008**, *155*, (6), P78-P81.
26. Mayrhofer, K. J. J.; Wiberg, G. K. H.; Arenz, M., Impact of glass corrosion on the electrocatalysis on Pt electrodes in alkaline electrolyte, *Journal of the Electrochemical Society*, **2008**, *155*, (1), P1-P5.
27. Mayrhofer, K. J. J.; Ashton, S. J.; Kreuzer, J.; Arenz, M., An Electrochemical Cell Configuration Incorporating an Ion Conducting Membrane Separator between Reference and Working Electrode, *International Journal of Electrochemical Science*, **2009**, *4*, (1), 1-8.
28. Newman, J., RESISTANCE FOR FLOW OF CURRENT TO A DISK, *Journal of the Electrochemical Society*, **1966**, *113*, (5), 501-502.



29. F. C. Nart, W. Vielstich., Normalization of porous active surfaces in *Handbook of fuel cells*. John Wiley & Sons Ltd: 2003.
30. Bard, A. J., Faulkner, L.R., *Electrochemical methods: Fundamentals and applications*. John Wiley & Sons: New York, 2001.
31. Vetter, K. J., *Electrochemical Kinetics: Theoretical and experimental aspects*. Academic Press: New York, 1967.
32. Skulason, E.; Karlberg, G. S.; Rossmeisl, J.; Bligaard, T.; Greeley, J.; Jonsson, H.; Norskov, J. K., Density functional theory calculations for the hydrogen evolution reaction in an electrochemical double layer on the Pt(111) electrode, *Physical Chemistry Chemical Physics*, **2007**, *9*, (25), 3241-3250.
33. Krischer, K.; Savinova, E. R., Fundamental of Electrocatalysis. In *Handbook of Heterogeneous Catalysis*, Ertl, G.; Knözinger, H.; Schüth, F.; Weitkamp, J.; Editors, Eds. Wiley-VCH: Chichester, 2009; p p. 1873.
34. Norskov, J. K.; Bligaard, T.; Logadottir, A.; Kitchin, J. R.; Chen, J. G.; Pandelov, S.; Stimming, U., Trends in the exchange current for hydrogen evolution, *Journal of the Electrochemical Society*, **2005**, *152*, (3), J23-J26.
35. Mello, R. M. Q.; Ticianelli, E. A., Kinetic study of the hydrogen oxidation reaction on platinum and Nafion(R) covered platinum electrodes, *Electrochimica Acta*, **1997**, *42*, (6), 1031-1039.
36. Wang, J. X.; Springer, T. E.; Liu, P.; Shao, M. H.; Adzic, R. R., Hydrogen oxidation reaction on Pt in acidic media: Adsorption isotherm and activation free energies, *Journal of Physical Chemistry C*, **2007**, *111*, (33), 12425-12433.
37. Anderson, A. B.; Sidik, R. A.; Narayanasamy, J.; Shiller, P., Theoretical calculation of activation energies for  $\text{Pt} + \text{H} + (\text{aq}) + \text{e}(-) (\text{U}) \leftrightarrow \text{Pt-H}$ : Activation energy-based symmetry factors in the marcus normal and inverted regions, *Journal of Physical Chemistry B*, **2003**, *107*, (19), 4618-4623.
38. Cai, Y.; Anderson, A. B., The reversible hydrogen electrode: Potential-dependent activation energies over platinum from quantum theory, *Journal of Physical Chemistry B*, **2004**, *108*, (28), 9829-9833.
39. Zhang, T. H.; Anderson, A. B., Hydrogen oxidation and evolution on platinum electrodes in base: Theoretical study, *Journal of Physical Chemistry C*, **2007**, *111*, (24), 8644-8648.
40. Kinoshita, K., Particle-Size Effects for Oxygen Reduction on Highly Dispersed Platinum in Acid Electrolytes, *Journal of the Electrochemical Society*, **1990**, *137*, (3), 845-848.
41. Sheng, W.; Chen, S.; Crumlin, E. J.; Vescovo, E.; Shao-Horn, Y., *to be published*.
42. Markovic, N.; Gasteiger, H.; Ross, P. N., Kinetics of oxygen reduction on Pt(hkl) electrodes: Implications for the crystallite size effect with supported Pt electrocatalysts, *Journal of the Electrochemical Society*, **1997**, *144*, (5), 1591-1597.



## Chapter 4

# Synthesis of Multi-walled Carbon Nanotube Supported Pt Nanoparticles and their Electrocatalytic Activities and Durability

### 4.1 Introduction

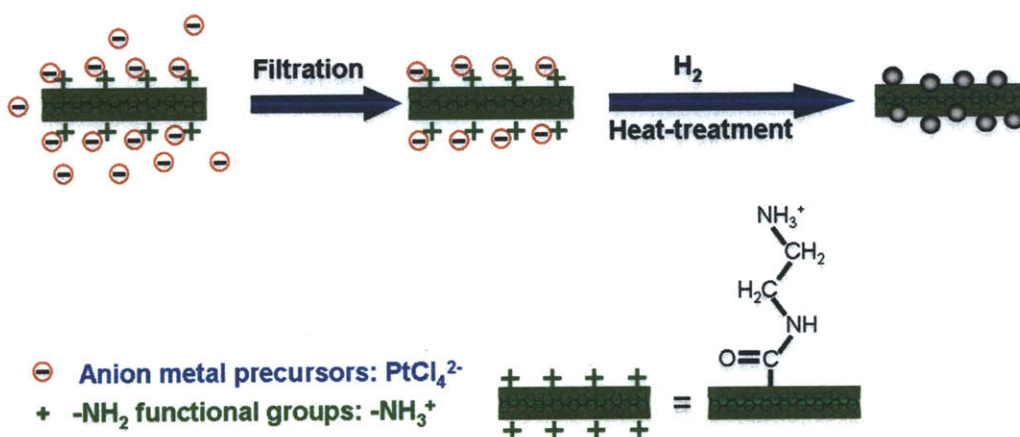
Proton exchange membrane fuel cells (PEMFC), as the highly efficient and environment-friendly energy conversion devices, have been showing great potential in the applications for both stationary and transportation power supply<sup>1-3</sup>. Screening high quality catalysts in terms of activity and durability has been an urgent mission to approach the theoretical efficiency of fuel cells, and to expedite the reactions at both electrodes, especially the very sluggish oxygen reduction reaction (ORR) at the cathode.<sup>4</sup> Among all the metal candidates, platinum (Pt) and Pt-based alloys have shown the highest activity for ORR<sup>6, 7</sup>. These catalysts are usually nanoscale and supported on carbon powders to maximize the overall surface area in a specified mass. However, a notable “cathode-thinning” effect is often caused by carbon corrosion during the PEMFC operation,<sup>8, 9</sup> which leads to a loss of the cathode void volume, thus influences the mass transport, and eventually the overall cell performance. This effect can be ascribed to the high cathode potential of 1.2 V ~ 1.5 V upon the start/stop during the PEMFC operation<sup>8, 10</sup> or under localized H<sub>2</sub> starvation condition.<sup>11-13</sup> Carbon corrosion rates significantly increase at such high potentials<sup>11</sup>. It has been found that a carbon weight loss of 5%~8%

will cause a serious current density loss of 20%~60% at 0.5V<sup>14</sup>. Therefore, a more electrochemically stable support material is desired to improve PEMFC performance.

One family of candidates is graphitic carbon materials such as carbon nanotubes (CNTs)<sup>15</sup>. CNTs have received extensive attention due to their unique structures, high conductivities, high mechanical properties and electrochemical stability.<sup>16</sup> These excellent properties of CNTs compared to amorphous carbon have made them very competitive as alternative support materials for fuel cell catalysts. To fabricate CNT supported catalysts, several synthesis methods are typically utilized: 1): direct decoration of pre-synthesized metal nanoparticles onto CNTs;<sup>17-19</sup> 2): electrodeposition of dissolved metal precursors in aqueous solution onto carbon nanotubes electrodes;<sup>20-22</sup> 3): chemical reduction of metal precursors using a reducing reagent such as supercritical methanol,<sup>23</sup> copper foil<sup>24</sup> or carbon nanotube itself;<sup>25</sup> and 4): immobilizing metal precursor on CNTs through electrostatic interaction followed by chemical reduction.<sup>26-28</sup> These methods often lack technical controls for preventing agglomerations, narrowing particle size distribution, and cleaning particle surfaces. In this study, we have employed the same concept as in references,<sup>26-28</sup> i.e., using electrostatic interaction between positively charged CNT and negatively charge Pt salts to anchor Pt precursors onto multi-walled CNTs (MWCNTs) and subsequently the Pt precursor/MWCNTs composite are heat-treated in H<sub>2</sub> atmosphere as shown in Scheme 4.1. H<sub>2</sub> not only plays a role of reducing agent but also facilitates removing of impurity and functional groups under a thermal treatment. We present the evaluation of their activities for ORR and durability under potential holding using high-surface-area carbon supported Pt NPs as reference. The

results show that this fabrication approach is very straightforward and indicates the application in the synthesis of a wide choice of metal/MWCNTs materials.

**Scheme 4.1.** Synthesis route of MWCNT supported Pt NPs.



## 4.2 Experimental

### 4.2.1 Sample Preparation

*pH effect on the loading of  $\text{PtCl}_4^{2-}$  on  $\text{NH}_2$ -MWCNT:* the amine functionalized multi-walled carbon nanotubes ( $\text{NH}_2$ -MWCNTs) were prepared based on the method reported previously<sup>29</sup>. One mg of dried  $\text{NH}_2$ -MWCNTs was dispersed in 3.5 mL of de-ionized water ( $18.2 \text{ M}\Omega\cdot\text{cm}$ , Millipore) of which pH was adjusted using chloric acid (Sigma Aldrich). 0.5 mL of  $\text{K}_2\text{PtCl}_4$  solution was added into the  $\text{NH}_2$ -MWCNT water suspension while stirring and the final concentration of  $\text{K}_2\text{PtCl}_4$  in the suspension was 5 mM. The mixture was kept stirring for overnight and the final pH was measured using pH meter (AB15plus, Sisher Scientific Inc.). Subsequently, the  $\text{PtCl}_4^{2-}$  adsorbed MWCNT

powder was collected through nylon membrane filter and washed several times using de-ionized water with the same pH.

*Concentration effect of the  $\text{PtCl}_4^{2-}$  on the loading of  $\text{PtCl}_4^{2-}$  on  $\text{NH}_2\text{-MWCNT}$ :*

One mg of dried  $\text{NH}_2\text{-MWCNTs}$  was dispersed in 3.5 mL of de-ionized water. 0.5 mL of  $\text{K}_2\text{PtCl}_4$  solution with different amount of  $\text{K}_2\text{PtCl}_4$  dissolved was added into the MWCNT water suspension under stirring, resulting in the final concentration of  $\text{K}_2\text{PtCl}_4$  ranging from 0.1 mM to 10 mM. The suspension was kept stirring for overnight, and the final pH was about 3.5. The  $\text{PtCl}_4^{2-}$  adsorbed MWCNTs were collected in the same manner as mentioned above.

*Heat-treatment of  $\text{PtCl}_4^{2-}$  adsorbed MWCNT:*  $\text{PtCl}_4^{2-}$  adsorbed MWCNTs made from the suspension with a final pH of 3.5 and a final  $\text{K}_2\text{PtCl}_4$  concentration of 5 mM were treated in 4% hydrogen ( $\text{H}_2$ ) atmosphere (balanced with argon) in a image furnace (ULVAC/SINKU-RIKO, Inc.) at 200 °C, 300 °C, 400 °C, 500 °C or 600 °C for three hours to generate MWCNT supported Pt nanoparticles.

#### **4.2.2 Physical characterization of $\text{PtCl}_4^{2-}/\text{MWCNTs}$ composite upon heat-treatment**

*X-ray photoemission spectroscopy measurements:* the element analysis of  $\text{PtCl}_4^{2-}/\text{MWCNTs}$  was done using X-ray photoemission spectroscopy (XPS) on a Kratos Axis Ultra Spectrometer (Manchester, UK) with a monochromatized aluminum X-ray source ( $\text{Al K}\alpha$ ). High-resolution spectra were collected for quantitative analysis of element composition of  $\text{PtCl}_4^{2-}/\text{MWCNTs}$ . All spectra were calibrated with  $\text{SP}^2$  hybridized carbons of C 1s photoemission peak at 284.5 eV. The photoemission spectra were fitted after a Shirley-type background subtraction. The relative sensitivity factors (RSF) values

of 0.278 and 5.575 for C 1s and Pt 4f respectively, were used for the element quantification, as supplied by the XPS manufacturer (Kratos Analytical).

*High-resolution transmission electron microscopy measurements:* The particle size and size distribution of Pt NPs/MWCNTs prepared through the heat-treatment of  $\text{PtCl}_4^{2-}$ /MWCNT in 4%  $\text{H}_2$  atmosphere at different temperature were made on JEOL 2010F high resolution transmission electron microscope (HRTEM) operated at 200k eV. TEM samples were prepared by drop casting suspensions of the Pt/MWCNTs powder in ethanol on TEM grids (Lacey carbon coated copper grids, EMS) and dried in air.

*Thermal gravimetric analysis:* The weight loss of  $\text{PtCl}_4^{2-}$  adsorbed MWCNTs upon heat-treatment was made on (Netzsch STA 449 C, Exponent) in 2.5%  $\text{H}_2$  atmosphere, balanced with Argon (Ar). The sweep rate was 5 °C/minute. Absolute loading of Pt on MWCNTs was determined by burning off MWCNTs in  $\text{O}_2$  atmosphere.

#### **4.2.3 Electrochemical characterization of Pt NPs/MWCNTs**

*Pt/MWCNTs electrode preparation:* The Pt/MWCNTs electrodes were prepared following our previous study<sup>30</sup> except that Nafion binder was not used in this work. First, Pt/MWCNTs powder under different heat-treatment temperatures was dispersed in de-ionized water (18.2  $\text{M}\Omega\cdot\text{cm}$ , Millipore) using ultrasonication in ice-bath, generating a catalyst suspension of ~0.5 mg/mL. 20  $\mu\text{L}$  of the suspension was deposited on the glassy carbon electrode (GCE) (5 mm in diameter, Pine Instrument) which was pre-polished to 0.05 micron alumina and dried in air at room temperature.

*Cyclic voltammetry:* As prepared electrodes were mounted to a rotator (Pine Instruments) as the working electrode and immersed into 0.1 M of perchloric acid

(HClO<sub>4</sub>), diluted from 70% HClO<sub>4</sub> (GFS Chemicals Inc.) with de-ionized water. A Pt wire and a saturated calomel electrode (SCE, Analytical Sensor, Inc.) were used as the counter electrode and the reference electrode respectively. However, the potentials reported throughout this paper were referred to that of the reversible hydrogen electrode (RHE), which was calibrated from the rotating disk electrode measurement of hydrogen oxidation<sup>30</sup>. After the electrolyte was bubbled with argon (Ar) for at least 20 minutes, the working electrode was scanned between ~0.03 V and ~1.1 V vs. RHE at a sweep rate of 50 mV/s for ~60 cycles before reaching the steady state. The cyclic voltammograms were then recorded at 50 mV/s and at the room temperature in the same potential window. The electrochemical surface area (ESA) of Pt nanoparticles were calculated from the Pt-hydrogen desorptions region between 0.05 V and ~0.4 V after double layer subtraction, assuming an electrical charge density of 210 μC/cm<sup>2</sup><sub>Pt</sub> for one monolayer adsorption of hydrogen on Pt surface<sup>31</sup>.

*Rotating disk electrode measurements of ORR activity:* The oxygen reduction reaction (ORR) activities on Pt/MWCNTs catalysts in 0.1 M HClO<sub>4</sub> were investigated using the rotating disk electrode method. After the electrolyte was saturated with pure oxygen (O<sub>2</sub>), polarization curves were recorded between ~0.03 V and ~1.1 V vs. RHE at a sweep rate of 10 mV/s and at room temperature. The rotation rates were 100, 400, 900, and 1600 rpm. To eliminate the background contribution from CVs, the ORR polarization curves were normalized by subtracting the corresponding CVs which were collected in Ar-saturated 0.1 M HClO<sub>4</sub> at the same sweep rate. The kinetic current  $i_k$  of ORR was obtained after mass-transport correction, e.g. calculated based on the Levich equation

$$\frac{1}{i} = \frac{1}{i_k} + \frac{1}{i_D}$$

Normalization of the kinetic current  $i_k$  by the true electrochemical surface



area (ESA) of Pt from CVs provided the specific activities  $i_s$ ; and  $i_s$  at 0.9 V vs. RHE was used to compare the catalytic properties among the samples. The Koutecky-Levich plot ( $\frac{1}{i} \propto \frac{1}{\omega^{1/2}}$ ) from  $\frac{1}{i} = \frac{1}{i_k} + \frac{1}{i_D} = \frac{1}{i_k} + \frac{1}{Bc_0\omega^{1/2}}$  was obtained at E = 0.6 V and compared to the literature. In the Levich equation,  $Bc_0 = 0.2nFC_{O_2}(D_{O_2})^{2/3}\nu^{-1/6}$  where  $n$  is the apparent number of electrons transferred in the reaction (4),  $F$  is the Faraday constant,  $C_{O_2}$  is the  $O_2$  concentration in 0.1 M  $HClO_4$ ,  $D_{O_2}$  is the diffusivity of  $O_2$  in dilute electrolyte solutions and  $\nu$  is the kinematic viscosity of the electrolyte<sup>32</sup>.

### 4.3 Results and Discussion

Chemical composition analysis of  $PtCl_4^{2-}/MWCNTs$  composites was measured using X-ray photoemission spectroscopy (XPS) (Figure 4.1).

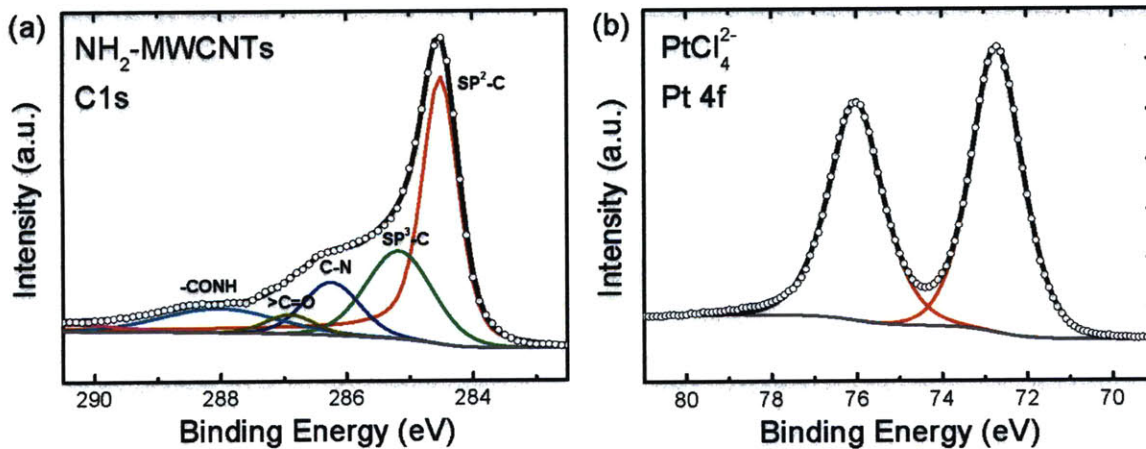


**Figure 4.1.** Representative XPS spectra of  $PtCl_4^{2-}/MWCNTs$  composites for (a): carbon 1s; and (b): Pt 4f. Curve-fitting has been made according to reference<sup>29</sup> after a Shirley-type background subtraction, and all spectra have been calibrated to  $SP^2$  hybrid carbon at 284.5 eV.

C 1s peak has been de-convoluted into SP<sup>2</sup> and SP<sup>3</sup> hybrid C peaks and other components of the functional groups. Concrete peak assignment is referred to the previous study<sup>29</sup>. Pt 4f doublets at 72.7 eV (Pt 4f<sub>7/2</sub>) and 76.0 eV (Pt 4f<sub>5/2</sub>) are assigned to PtCl<sub>4</sub><sup>2-</sup> species on MWCNTs. From the peak area ratio between Pt 4f and C 1s, with the relative sensitivity factors (RSF) taken into account, the relative loadings of Pt species on MWCNTs obtained from the suspension at different pH levels and precursor concentrations were constructed as shown in Figure 4.2a and 4.3.

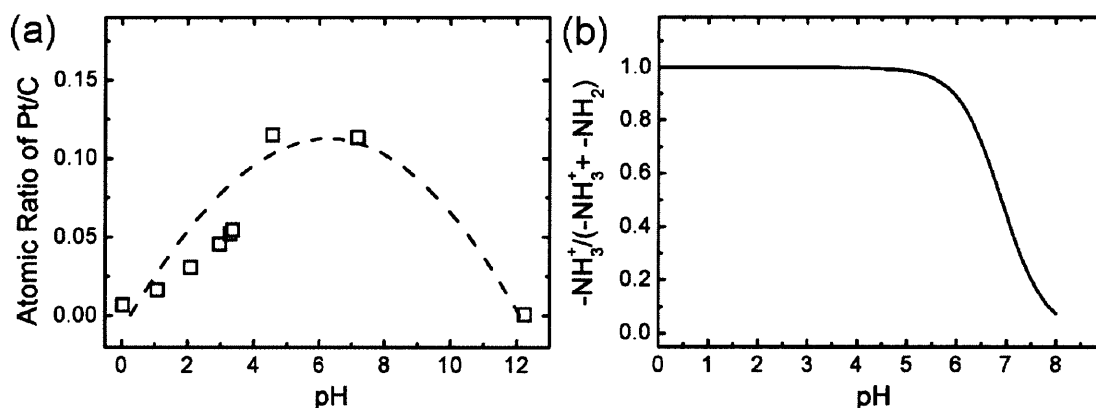


**Figure 4.2.** (a): Change of atomic ratio between Pt and C with the pH of suspensions containing PtCl<sub>4</sub><sup>2-</sup> and NH<sub>2</sub>-MWCNTs. The concentration of PtCl<sub>4</sub><sup>2-</sup> is fixed at 5 mM. (b): Simulated fraction of protonated amines among the total amine functional groups at different pH based on  $pK_a = pH - \log \frac{NH_2}{NH_3^+}$ , assuming that amine functionalized MWCNTs have a same  $pK_a$  (6.9) as that of NH<sub>2</sub>(CH<sub>2</sub>)<sub>2</sub>NH<sub>2</sub>.

Figure 4.2a shows that there is a certain range where PtCl<sub>4</sub><sup>2-</sup> loading reaches a maximum. Both strong basic and strong acidic suspensions result in a very low PtCl<sub>4</sub><sup>2-</sup> loading. In very basic environment such as pH=12, amine functional groups stay unprotonated due to abundant OH<sup>-</sup> anion groups, electrostatic interaction caused by opposite charges therefore does not take place. However, the very small Pt loading on MWCNTs

from strong acidic suspension seems to be contradictory with the predicted pH effect (Figure 4.2b). Assuming that the amine functional groups on MWCNTs have the same  $pK_a$  value as  $^+\text{NH}_3\text{-(CH}_2\text{CH}_2\text{)-NH}_3^+$ , the  $pK_a$  of which is 6.9, we calculated the fraction of protonated amine among the total amine groups based on  $pK_a = \text{pH} - \log \frac{\text{NH}_2}{\text{NH}_3^+}$  at different pH (Figure 4.2b). Obviously, the  $\text{-NH}_3^+$  fraction reaches the maximum below  $\text{pH}=6$  and keeps constant regardless of the pH. This behavior suggests that the loading of  $\text{PtCl}_4^{2-}$  onto MWCNTs should not change at low pH because all the amine functional groups are protonated and will participate in the electrostatic interaction. Nevertheless, in fact, the loading of  $\text{PtCl}_4^{2-}$  keeps decreasing as the pH becomes smaller. This discrepancy is believed to be caused by the competitive adsorption of foreign anion, mainly  $\text{Cl}^-$  which was introduced when chloric acid was used to adjust the pH value. In this study, the concentration of  $\text{PtCl}_4^{2-}$  was fixed at 5 mM. When pH decreases to 3, the concentration of  $\text{Cl}^-$  anion is 20% of  $\text{PtCl}_4^{2-}$ ; at  $\text{pH}=2$ , the concentration of  $\text{Cl}^-$  anion is as much as twice that of  $\text{PtCl}_4^{2-}$ . The electrostatic interaction between  $\text{-NH}_3^+$  and  $\text{Cl}^-$  would probably dominate at very low pH and thus the adsorption of  $\text{PtCl}_4^{2-}$  onto MWCNTs would be inhibited.

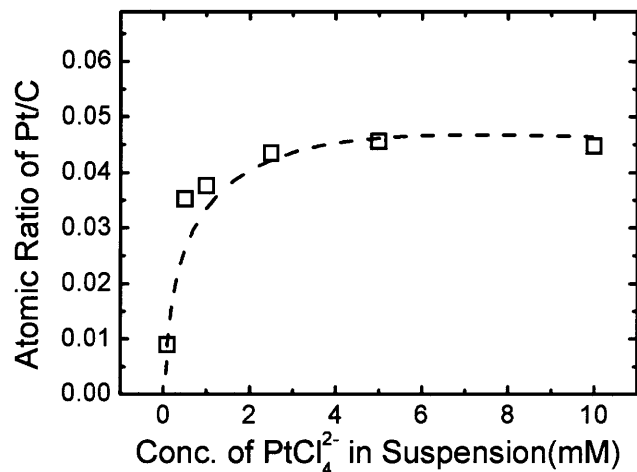


**Figure 4.3.** Change of atomic ratio between Pt and C with the concentration of PtCl<sub>4</sub><sup>2-</sup> in suspensions. The pH of the suspensions is about 3.5.

Figure 4.3 shows the change of loading of PtCl<sub>4</sub><sup>2-</sup> with the concentration of PtCl<sub>4</sub><sup>2-</sup> in the suspension containing 1 mg of MWCNTs at a final pH of about 3.5. For precursor concentrations higher than about 2 mM, the loading of PtCl<sub>4</sub><sup>2-</sup> reaches a plateau. However, at lower concentrations, loading of PtCl<sub>4</sub><sup>2-</sup> decreases accordingly. Apparently there are not enough PtCl<sub>4</sub><sup>2-</sup> anions in the suspension, which is further supported by the thermal gravimetric analysis (TGA) of PtCl<sub>4</sub><sup>2-</sup>/MWCNTs in H<sub>2</sub> atmosphere as shown in Figure 4.4.

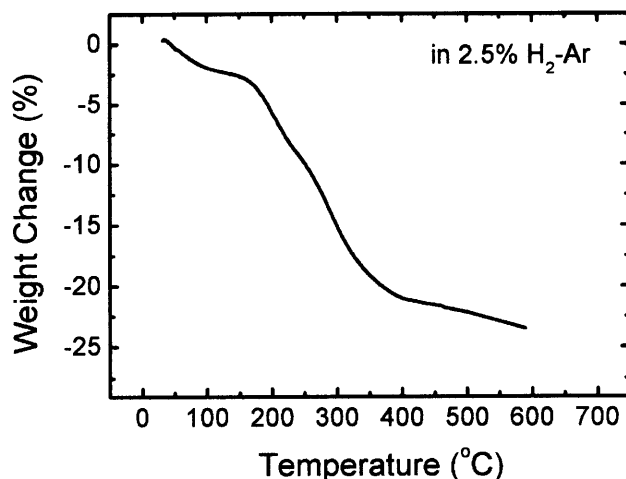


**Figure 4.4.** Weight change of PtCl<sub>4</sub><sup>2-</sup>/MWCNTs upon heat-treatment in H<sub>2</sub>. The sweep rate is 5 °C/minute.

The weight loss of PtCl<sub>4</sub><sup>2-</sup>/MWCNTs (prepared from the suspension with a pH of ~3.5, containing 1 mg of MWCNTs and 5 mM of PtCl<sub>4</sub><sup>2-</sup>) below 300 °C is due to the loss of the surface functional groups. The functional groups account for roughly 23% of the total PtCl<sub>4</sub><sup>2-</sup>/MWCNTs composites. By burning off the carbon nanotube support in O<sub>2</sub> (data not shown here), Pt weight was determined to be about 20% of total mass of PtCl<sub>4</sub><sup>2-</sup>/MWCNTs composite, corresponding to the ratio between Pt and MWCNTs of about 0.001 (mmoles of Pt) : 1 (mg of MWCNTs). When the concentration of PtCl<sub>4</sub><sup>2-</sup> in the suspension is lowered to 0.1 mM (The total volume of the suspension is 4 mL), the total PtCl<sub>4</sub><sup>2-</sup> anions would be 0.0004 mmoles, which is much lower than needed for the same loading (20%). Therefore, the loading of PtCl<sub>4</sub><sup>2-</sup> onto MWCNTs under this condition (0.1 mM of PtCl<sub>4</sub><sup>2-</sup>, 1 mg of MWCNTs, pH=3.5) is limited by the amount of PtCl<sub>4</sub><sup>2-</sup> available as mentioned above.

Element analysis of PtCl<sub>4</sub><sup>2-</sup>/MWCNTs composite upon heat-treatment in H<sub>2</sub> atmosphere was also investigated by XPS (Figure 4.5). The core level Pt 4f peaks (Figure

4.5a) show a clear positive shift as the heat-treatment temperature increases. Pt 4f<sub>7/2</sub> peak at 72.7 eV is assigned to PtCl<sub>4</sub><sup>2-</sup> precursors and it changes to 71.2 eV (Pt<sup>0</sup>) when treated at 300 °C and above, proving that PtCl<sub>4</sub><sup>2-</sup> precursors have been reduced to Pt<sup>0</sup>, while PtCl<sub>4</sub><sup>2-</sup>/MWCNTs composite treated at 200 °C falls in between. This observation is also in accordance with the TGA results that the weight loss below 200 °C is only 5% and almost no surface functional groups are removed; and the groups still bond to Pt precursors. In addition, after heat-treatment at 300 °C and above, Cl species are completely removed as shown by the disappearance of Cl 2p peaks (Figure 4.5b), supporting the argument that adsorbed PtCl<sub>4</sub><sup>2-</sup> anions have been entirely converted to Pt<sup>0</sup>.

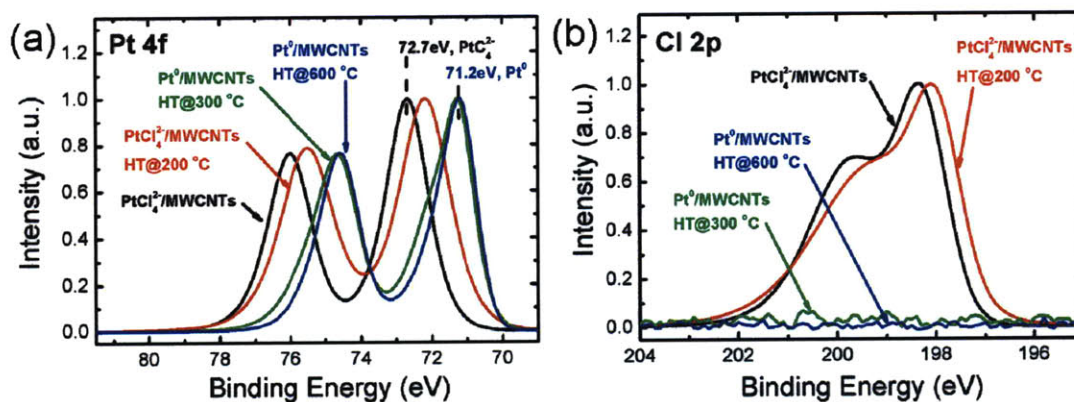


**Figure 4.5.** XPS spectra of PtCl<sub>4</sub><sup>2-</sup>/MWCNTs composites upon heat-treatment for (a): Pt 4f; and (b): Cl 2p.

High-resolution transmission electron microscopy measurements (HRTEM, Figure 4.6) shows that Pt<sup>0</sup> species form Pt NPs upon reduction by H<sub>2</sub> at elevated temperatures. Pt NPs disperse quite well on MWCNTs as can be seen from the HRTEM images and have a relatively narrow distribution. Pt NPs formed at 300 °C have an average particle size of 2.1±0.6 nm and the size slightly grows to 2.6±0.6 nm when

treated at 600 °C, yet the effect of heat-treatment temperature on particle size is not substantial.

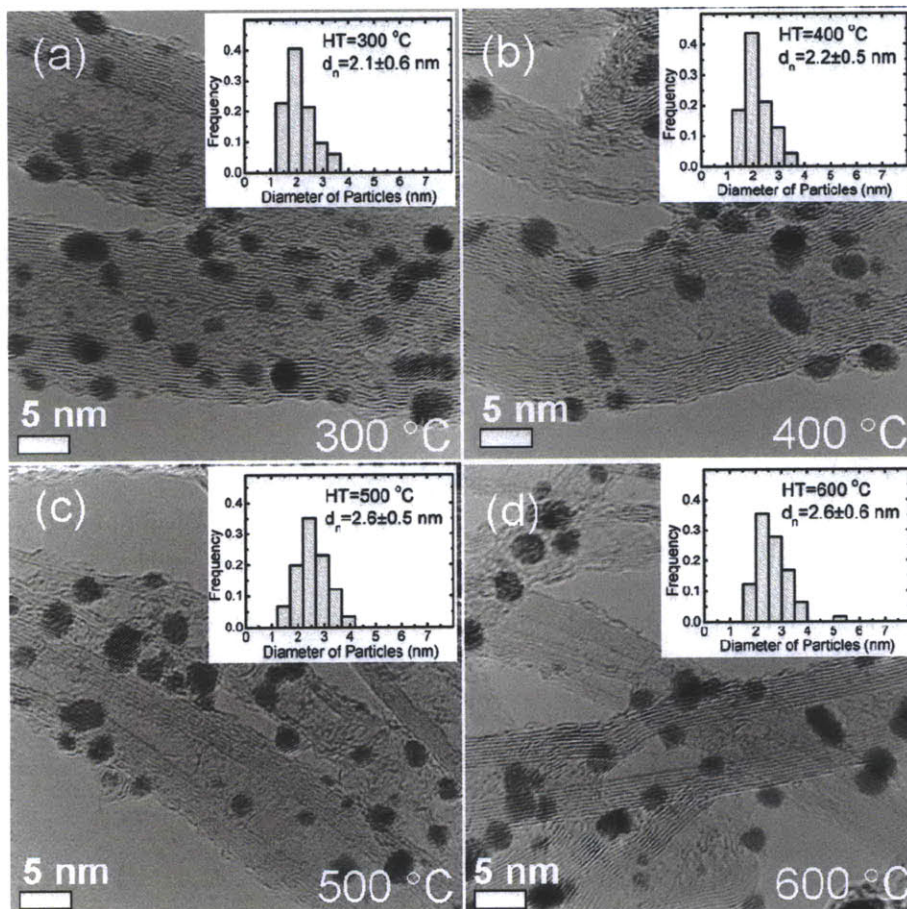


**Figure 4.6.** HRTEM images of Pt/MWCNTs formed by heat-treatment of  $\text{PtCl}_4^{2-}$ /MWCNTs in  $\text{H}_2$  atmosphere at (a): 300 °C; (b): 400 °C; (c): 500 °C and (d): 600 °C.

To compare the durability of Pt/MWCNTs and commercial high-surface-area-carbon supported Pt NPs (Pt/C), potential holding experiments were performed in Ar-saturated 0.1 M  $\text{HClO}_4$ . After holding the potential at 1.5 V/RHE for a certain period of time, cyclic voltammograms (CVs) of Pt/MWCNTs and Pt/C were recorded at 50 mV/s as shown in Figure 4.7a and 4.7b. The CVs show a typical Pt-H adsorption/desorption region below  $\sim 0.4$  V/RHE, a double layer region between 0.4 V and 0.6 V and Pt-OH

interaction region above 0.6 V, which agree well with the literature.<sup>33, 34</sup> Both of Pt/MWCNTs and Pt/C lose the electrochemical surface area upon potential holding and the ESA of the two types of catalysts drops to 50% of the original values after 36 hours (Figure 4.7c). There does not seem to be substantial difference in the ESA loss upon potential holding. However, the double layer current changes significantly (by a factor of two) with potential holding for Pt/C while it stays constant for Pt/MWCNTs as shown in Figure 4.7d. This current increase corresponds to quinone/hydroquinone redox couple due to the surface oxidation of the carbon support at 1.5 V, as suggested by previous study<sup>35</sup>. This observation strongly suggests that MWCNTs are more resistant towards electrochemical oxidation than amorphous carbon, thus are appropriate for the application as the catalyst support.



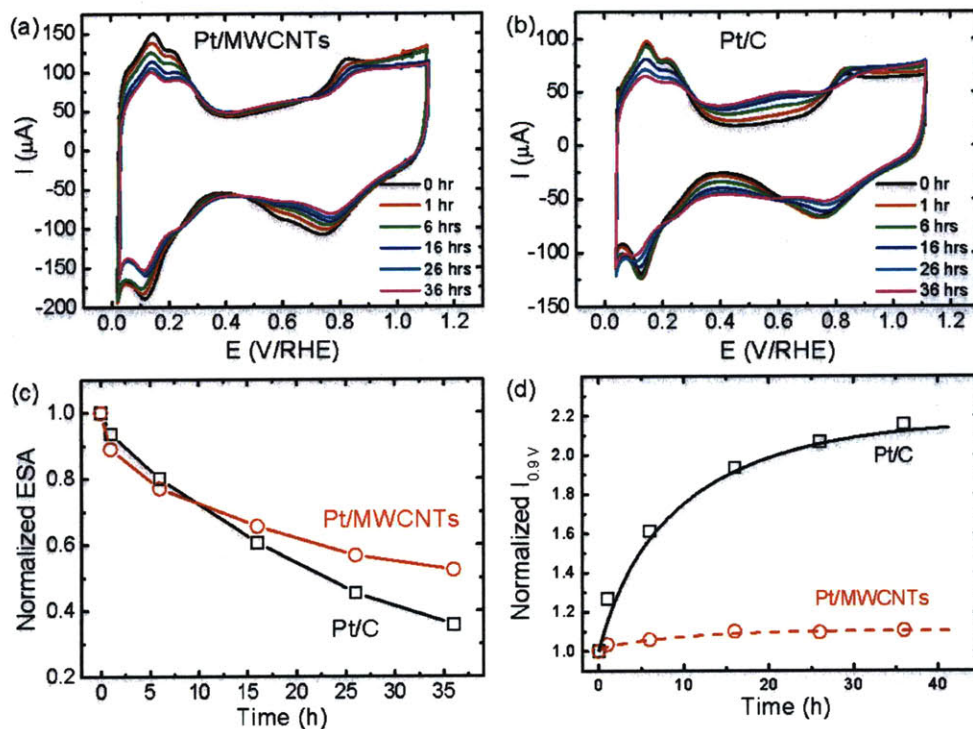


**Figure 4.7.** Cyclic voltammograms collected in Ar-saturated 0.1 M  $\text{HClO}_4$  upon potential holding at 1.5 V/RHE for (a): Pt/MWCNTs; and (b): Pt/C. The scanning rate is 50 mV/s. (c): Normalized electrochemical surface area of Pt/MWCNTs and Pt/C upon potential holding; and (d): normalized double-layer currents at 0.6 V/RHE of Pt/MWCNTs and Pt/C upon potential holding.

The morphology of Pt/MWCNTs and Pt/C after potential holding shows significant particle growth for both of the two types of catalysts (Figure 4.8). The length of the worm-like Pt particles for both cases is on the order of 10 nm. Because the potential was held at 1.5 V/RHE at which Pt dissolution is inhibited due to the passivation of Pt oxides<sup>36</sup>, we speculate that the ESA loss for Pt/MWCNTs and Pt/C is entirely caused by the particle growth via particle coalescence.<sup>37</sup>

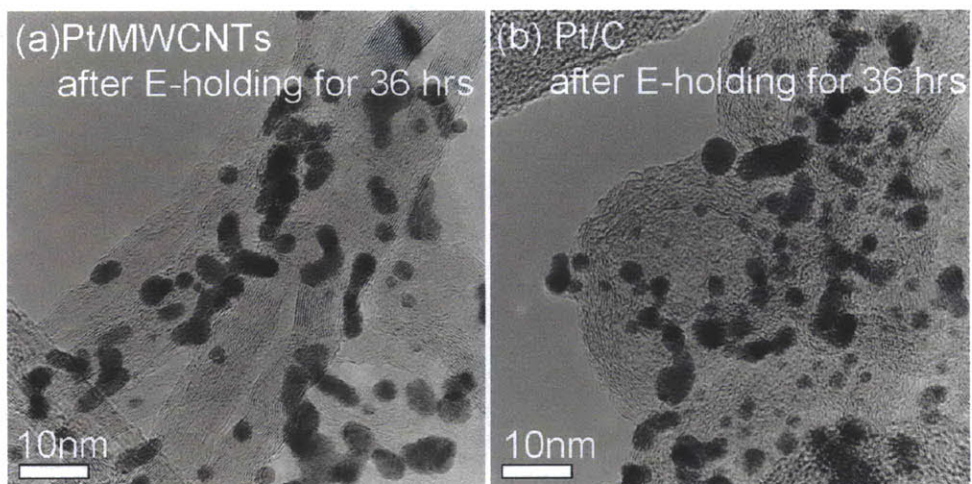


**Figure 4.8.** HRTEM images of (a): Pt/C and (b): Pt/MWCNTs after potential holding at 1.5 V/RHE for 36 hours.

Oxygen reduction reaction (ORR) on Pt/MWCNTs was measured in O<sub>2</sub>-saturated 0.1 M HClO<sub>4</sub> using the rotating disk electrode (RDE) method. Representative ORR polarization curves of Pt/MWCNTs (treated at 600 °C) at different rotation speeds and at room temperature are shown in Figure 4.9a. Following the kinetic-controlled region above 0.95 V/RHE, ORR enters the kinetic-diffusion mixed controlled region between 0.8 V and 0.95 V/RHE and subsequently is completely limited by mass transport starting from 0.8 V, which matches very well with previous reports<sup>38, 39</sup>. The Koutecky-Levich plot (inset) obtained at 0.6 V/RHE based on the Levich equation,  $\frac{1}{i}$  vs.  $\frac{1}{\omega^{1/2}}$  at different rotating speeds gives a perfect line, from the slope of which  $Bc_0$  is determined to be  $0.1514 \text{ mAcm}^2\omega^{-1/2}$ , which is in good agreement with the previously reported value<sup>39</sup> and suggests a four-electron transfer process of ORR. ORR specific activities at 0.85 V and 0.9V are obtained by normalization of kinetic currents, which are calculated from the Levich equation, to the true electrochemical surface area and compared with that of Pt/C as shown in Figure 4.9b. Regardless of the heat-treatment temperature, Pt/MWCNTs

show identical ORR activity with that of Pt/C, which agrees with the so-called particle size effect on ORR because Pt/MWCNTs treated at different temperature have very close particle size with that of Pt/C.<sup>38</sup> This result also indicates that the type of carbon support does not seem to influence on the activity of Pt NPs.

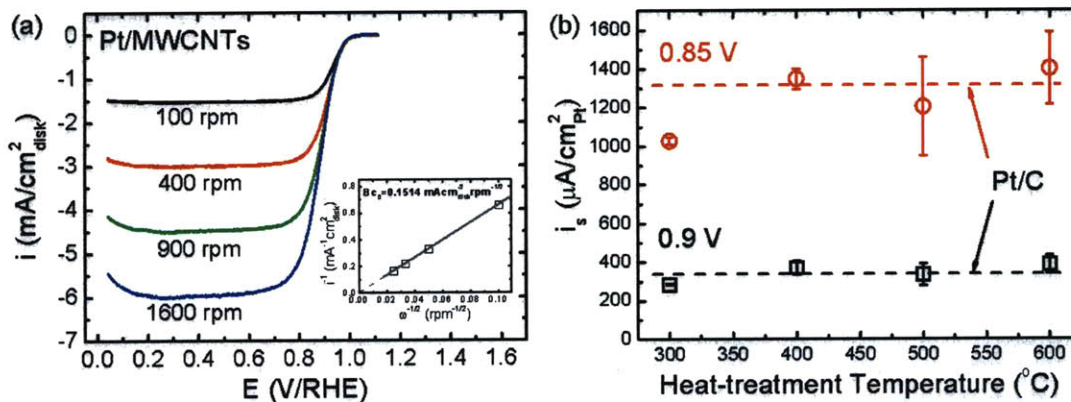


**Figure 4.9.** (a): Representative ORR polarization curves of Pt/MWCNTs in O<sub>2</sub>-saturated 0.1 M HClO<sub>4</sub> at different rotating speeds. The inset is the Koutecky-Levich plot obtained at 0.6 V/RHE; and (b): specific ORR activities at 0.9 V and 0.85 V of Pt/MWCNTs treated at different temperatures, compared with those of Pt/C.

#### 4.4 Conclusions

In summary, we have demonstrated an approach to synthesize MWCNT supported Pt NPs as electrocatalyst for oxygen reduction reaction. Through the electrostatic interaction between anion PtCl<sub>4</sub><sup>2-</sup> precursor and amine-functionalized MWCNTs, PtCl<sub>4</sub><sup>2-</sup> anions are introduced onto MWCNTs and subsequently reduced to form Pt NPs upon heat-treatment in H<sub>2</sub>. The results show that the loading of Pt on MWCNTs can be tuned by adjusting either the pH value of the reaction suspension or the

concentration of  $\text{PtCl}_4^{2-}$ . XPS combined with TGA measurements illustrate that a complete reduction of  $\text{PtCl}_4^{2-}$  on MWCNTs takes place above 300 °C and the functional groups are also removed completely around this temperature. HRTEM characterizations show that as-prepared Pt NPs are 2 nm in average particle size with a narrow distribution and they are well-dispersed on MWCNTs. As-prepared Pt/MWCNTs catalysts exhibit a greatly enhanced durability upon potential holding due to the higher resistance of MWCNTs over high-surface-area carbon towards carbon corrosion, while maintaining comparable ORR activities to that of Pt/C. The study indicates that MWCNTs have great potential to solve the problem of carbon corrosion during the fuel cell operation.

## 4.5 References

1. O'Hayre, R.; Cha, S.-W.; Colella, W.; Prinz, F. B., *Fuel Cell Fundamentals*. John Wiley & Sons: New York.
2. Barbir, F., System design for stationary power generation. In *Handbook of Fuel Cells: Fundamentals, Technology and Applications*, Vielstich, W.; Lamm, A.; Gasteiger, H. A., Eds. John Wiley & Sons: New York, 2003; Vol. 4.
3. Konrad, G.; Sommer, M.; Loschko, B.; Schell, A.; Docter, A., System design for vehicle applications: DaimlerChrysler. In *Handbook of Fuel Cells: Fundamentals, Technology and Applications*, Vielstich, W.; Lamm, A.; Gasteiger, H. A., Eds. John Wiley & Sons: New York, 2003; Vol. 2.
4. Gasteiger, H. A.; Panels, J. E.; Yan, S. G., Dependence of PEM fuel cell performance on catalyst loading, *Journal of Power Sources*, **2004**, *127*, (1-2), 162-171.
5. Markovic, N. M.; Ross, P. N., Surface science studies of model fuel cell electrocatalysts, *Surface Science Reports*, **2002**, *45*, (4-6), 121-229.
6. Norskov, J. K.; Rossmeisl, J.; Logadottir, A.; Lindqvist, L.; Kitchin, J. R.; Bligaard, T.; Jonsson, H., Origin of the overpotential for oxygen reduction at a fuel-cell cathode, *Journal of Physical Chemistry B*, **2004**, *108*, (46), 17886-17892.
7. Gasteiger, H. A.; Kocha, S. S.; Sompalli, B.; Wagner, F. T., Activity benchmarks and requirements for Pt, Pt-alloy, and non-Pt oxygen reduction catalysts for PEMFCs, *Applied Catalysis B-Environmental*, **2005**, *56*, (1-2), 9-35.
8. Reiser, C. A.; Bregoli, L.; Patterson, T. W.; Yi, J. S.; Yang, J. D. L.; Perry, M. L.; Jarvi, T. D., A reverse-current decay mechanism for fuel cells, *Electrochemical and Solid State Letters*, **2005**, *8*, (6), A273-A276.
9. Zhang, J. X.; Litterer, B. A.; Gu, W.; Liu, H.; Gasteiger, H. A., Effect of hydrogen and oxygen partial pressure on Pt precipitation within the membrane of PEMFCs, *Journal of the Electrochemical Society*, **2007**, *154*, (10), B1006-B1011.
10. Yu, P. T.; Gu, W.; Makharia, R.; Wagner, F. T.; Gasteiger, H. A., The Impact of Carbon Stability on PEM Fuel Cell Startup and Shutdown Voltage Degradation, *ECS Transactions*, **2006**, *3*, (1), 797-809.
11. Makharia, R.; Kocha, S. S.; Yu, P. T.; Sweikart, M. A.; Gu, W.; Wagner, F. T.; Gasteiger, H. A., Durable PEM Fuel Cell Electrode Materials: Requirements and Benchmarking Methodologies, *ECS Transactions*, **2006**, *1*, (8), 3-18.
12. Liu, Z. Y.; Brady, B. K.; Carter, R. N.; Litterer, B.; Budinski, M.; Hyun, J. K.; Muller, D. A., Characterization of carbon corrosion-induced structural damage of PEM fuel cell cathode electrodes caused by local fuel starvation, *Journal of the Electrochemical Society*, **2008**, *155*, (10), B979-B984.
13. Patterson, T. W.; Darling, R. M., Damage to the cathode catalyst of a PEM fuel cell caused by localized fuel starvation, *Electrochemical and Solid State Letters*, **2006**, *9*, (4), A183-A185.
14. Gasteiger, H. A.; Gu, W.; Litterer, B.; Makharia, R.; Brady, B.; Budnski, M.; Thompson, E.; Wagner, F. T.; Yan, S. G.; Yu, P. T., Catalyst degradation mechanisms in PEM and direct methanol fuel cells, *Mini-Micro Fuel Cells: Fundamentals and Applications*, **2008**, 225-233.

15. Borup, R.; Meyers, J.; Pivovar, B.; Kim, Y. S.; Mukundan, R.; Garland, N.; Myers, D.; Wilson, M.; Garzon, F.; Wood, D.; Zelenay, P.; More, K.; Stroh, K.; Zawodzinski, T.; Boncella, J.; McGrath, J. E.; Inaba, M.; Miyatake, K.; Hori, M.; Ota, K.; Ogumi, Z.; Miyata, S.; Nishikata, A.; Siroma, Z.; Uchimoto, Y.; Yasuda, K.; Kimijima, K. I.; Iwashita, N., Scientific aspects of polymer electrolyte fuel cell durability and degradation, *Chemical Reviews*, **2007**, *107*, (10), 3904-3951.
16. Endo, M.; Strano, M. S.; Ajayan, P. M., Potential applications of carbon nanotubes, *Carbon Nanotubes*, **2008**, *111*, 13-61.
17. Unger, E.; Duesberg, G. S.; Liebau, M.; Graham, A. P.; Seidel, R.; Kreupl, F.; Hoenlein, W., Decoration of multi-walled carbon nanotubes with noble- and transition-metal clusters and formation of CNT-CNT networks, *Applied Physics a-Materials Science & Processing*, **2003**, *77*, (6), 735-738.
18. Kongkanand, A.; Kuwabata, S.; Girishkumar, G.; Kamat, P., Single-wall carbon nanotubes supported platinum nanoparticles with improved electrocatalytic activity for oxygen reduction reaction, *Langmuir*, **2006**, *22*, (5), 2392-2396.
19. Henley, S. J.; Watts, P. C. P.; Mureau, N.; Silva, S. R. P., Laser-induced decoration of carbon nanotubes with metal nanoparticles, *Applied Physics a-Materials Science & Processing*, **2008**, *93*, (4), 875-879.
20. Day, T. M.; Unwin, P. R.; Macpherson, J. V., Factors controlling the electrodeposition of metal nanoparticles on pristine single walled carbon nanotubes, *Nano Letters*, **2007**, *7*, (1), 51-57.
21. Quinn, B. M.; Dekker, C.; Lemay, S. G., Electrodeposition of noble metal nanoparticles on carbon nanotubes, *Journal of the American Chemical Society*, **2005**, *127*, (17), 6146-6147.
22. Qu, J. Y.; Chen, H. J.; Dong, S. J., In Situ Fabrication of Noble Metal Nanoparticles Modified Multiwalled Carbon Nanotubes and Related Electrocatalysis, *Electroanalysis*, **2008**, *20*, (22), 2410-2415.
23. Sun, Z. Y.; Fu, L.; Liu, Z. M.; Han, B. X.; Liu, Y. Q.; Du, J. M., Synthesis of noble metal/carbon nanotube composites in supercritical methanol, *Journal of Nanoscience and Nanotechnology*, **2006**, *6*, (3), 691-697.
24. Qu, L. T.; Dai, L. M.; Osawa, E., Shape/size-control led syntheses of metal nanoparticles for site-selective modification of carbon nanotubes, *Journal of the American Chemical Society*, **2006**, *128*, (16), 5523-5532.
25. Choi, H. C.; Shim, M.; Bangsaruntip, S.; Dai, H. J., Spontaneous reduction of metal ions on the sidewalls of carbon nanotubes, *Journal of the American Chemical Society*, **2002**, *124*, (31), 9058-9059.
26. Wang, S.; Jiang, S. P.; Wang, X., Polyelectrolyte functionalized carbon nanotubes as a support for noble metal electrocatalysts and their activity for methanol oxidation, *Nanotechnology*, **2008**, *19*, (26), 5601-5606.
27. Wang, S. Y.; Jiang, S. P.; White, T. J.; Guo, J.; Wang, X., Assembling Interconnected Pt Nanoparticles on Multiwalled Carbon Nanotubes and Their Electrocatalytic Activity for Fuel Cells, *Advanced Functional Materials*, **2009**, (19), 1-8.
28. Guo, S. J.; Dong, S. J.; Wang, E. K., Constructing Carbon Nanotube/Pt Nanoparticle Hybrids Using an Imidazolium-Salt-Based Ionic Liquid as a Linker, *Advanced Materials*, **2010**, *22*, (11), 1269-1272.

29. Lee, S. W.; Kim, B. S.; Chen, S.; Shao-Horn, Y.; Hammond, P. T., Layer-by-Layer Assembly of All Carbon Nanotube Ultrathin Films for Electrochemical Applications, *Journal of the American Chemical Society*, **2009**, *131*, (2), 671-679.
30. Chen, S.; Sheng, W. C.; Yabuuchi, N.; Ferreira, P. J.; Allard, L. F.; Shao-Horn, Y., Origin of Oxygen Reduction Reaction Activity on "Pt<sub>3</sub>Co" Nanoparticles: Atomically Resolved Chemical Compositions and Structures, *Journal of Physical Chemistry C*, **2009**, *113*, (3), 1109-1125.
31. Nart, F. C.; Vielstich, W., Normalization of porous active surfaces, . In *Handbook of Fuel Cells: Fundamentals, Technology and Applications*, Vielstich, W.; Lamm, A.; Gasteiger, H. A., Eds. John Wiley & Sons: New York, 2003; p 302.
32. Bard, A. J.; Faulkner, L. R., *Electrochemical Methods: Fundamentals and Applications*. John Wiley & Sons: New York, 2001.
33. Mayrhofer, K. J. J.; Strmcnik, D.; Blizanac, B. B.; Stamenkovic, V.; Arenz, M.; Markovic, N. M., Measurement of oxygen reduction activities via the rotating disc electrode method: From Pt model surfaces to carbon-supported high surface area catalysts, *Electrochimica Acta*, **2008**, *53*, (7), 3181-3188.
34. Zhang, J.; Sasaki, K.; Sutter, E.; Adzic, R. R., Stabilization of platinum oxygen-reduction electrocatalysts using gold clusters, *Science*, **2007**, *315*, (5809), 220-222.
35. Kangasniemi, K. H.; Condit, D. A.; Jarvi, T. D., Characterization of vulcan electrochemically oxidized under simulated PEM fuel cell conditions, *Journal of the Electrochemical Society*, **2004**, *151*, (4), E125-E132.
36. Wang, X. P.; Kumar, R.; Myers, D. J., Effect of voltage on platinum dissolution relevance to polymer electrolyte fuel cells, *Electrochemical and Solid State Letters*, **2006**, *9*, (5), A225-A227.
37. Shao-Horn, Y.; Sheng, W. C.; Chen, S.; Ferreira, P. J.; Holby, E. F.; Morgan, D., Instability of supported platinum nanoparticles in low-temperature fuel cells, *Topics in Catalysis*, **2007**, *46*, (3-4), 285-305.
38. Mayrhofer, K. J. J.; Blizanac, B. B.; Arenz, M.; Stamenkovic, V. R.; Ross, P. N.; Markovic, N. M., The impact of geometric and surface electronic properties of Pt-catalysts on the particle size effect in electrocatalysis, *Journal of Physical Chemistry B*, **2005**, *109*, (30), 14433-14440.
39. Paulus, U. A.; Wokaun, A.; Scherer, G. G.; Schmidt, T. J.; Stamenkovic, V.; Radmilovic, V.; Markovic, N. M.; Ross, P. N., Oxygen reduction on carbon-supported Pt-Ni and Pt-Co alloy catalysts, *Journal of Physical Chemistry B*, **2002**, *106*, (16), 4181-4191.





## Chapter 5

### Achievements and Perspectives

#### 5.1 Achievements

The ORR and the HOR are the two main reactions in a H<sub>2</sub>-O<sub>2</sub> based PEMFCs or alkaline FCs. In addition to a prospect of improving FC performance, both of the ORR and the HOR kinetics are also of scientific interests for understanding physical chemistry at the solid-liquid interface. In this thesis, the ORR activities and HOR activities on carbon supported Pt NPs were studied in both acidic and alkaline electrolytes to develop a better understanding of the electron-transfer kinetics at the solid-liquid interface and to provide fundamental understandings of the electrocatalytic behaviors of Pt nanoparticles for the ORR and the HOR as a function of electrolytes.

Our findings that the specific ORR activities are size-independent below 5 nm in both HClO<sub>4</sub> and H<sub>2</sub>SO<sub>4</sub> acids suggest that smaller Pt NPs can be used for the cathode of FCs for higher mass activities due to their larger surface area per mass. However, the instability tests of Pt NPs show that larger sizes can maintain a long-term operation in FC better than smaller ones. Therefore, we suggest that a moderate NP size that is optimized for both high mass activity and stability is most desirable for FC applications. Investigations of the surface electronic structure by the UPS measurements and surface composition by the XPS measurements help identify the material properties relevant for

the ORR activity. We expect these findings to provide significant insights into the design of new Pt NP catalysts with high ORR activity and stability.

The HOR/HER kinetics were studied on a polycrystalline platinum (Pt(pc)) and an industrial applied catalyst Pt/C in 0.1 M KOH successfully. We show for the first time that the slow HOR kinetics in alkaline will induce additional 130 mV~ 150 mV overpotential in alkaline FCs compared with PEMFCs under the same conditions (catalyst loading, temperature, pressure of H<sub>2</sub>). This additional overpotential accounts for almost one third of the ORR overpotential in alkaline FCs and calls for a new research activity for the development of the anode catalysts for the alkaline FCs. From the fundamental point of view, although the information obtained so far cannot exclusively determine the mechanism for the HOR/HER, we have tentatively assigned the reaction mechanism to the Heyrovsky-Volmer mechanism with the Volmer reaction being the rate-determining step, which needs to be verified by further experiments and theoretical calculations.

The studies of the multi-walled carbon nanotube supported Pt NPs present a convenient approach of synthesizing Pt NPs/MWCNTs hybrid material as a stable, corrosion-resistant electrocatalyst for the FC reactions. This approach allows a good dispersion of Pt NPs supported on MWCNTs with a comparable ORR activity to that of the Pt/C. From a durability test, the Pt/MWCNTs have a more durable performance upon potential holding over the Pt/C, which we believe is due to the resistance of the MWCNTs towards carbon corrosion. This work indicates that MWCNTs offer a potentially more robust catalyst support for NPs in FC applications.

## 5.2 Perspectives

The development of a more active catalyst for the ORR is the most crucial research goal for improving the FC efficiency. Currently, Pt-based catalysts are the most active catalytic materials for the ORR. This thesis work suggests that the ORR prefer to take place at the terrace plane, while the Pt dissolution prefers to happen on the corner and edge sites. Therefore developments of highly-faceted Pt NPs with less surface defects, such as nanocubes or nanotetrahedra, are possible approaches for engineering a more durable form of Pt electrocatalyst than the current Pt/C. Furthermore, because only the surfaces of catalysts are responsible for the electrochemical reactions, the inner core can be replaced with other materials in order to reduce the cost. Studies of such core/shell structures have been carried out in many research groups, which have demonstrated the use of lower cost transition metal cores to lower the Pt mass activity<sup>1,2</sup>. In addition, using transition metal core also offers a possibility of further increasing the mass activity by way of changing the Pt electronic structure. From the study of the model bulk surfaces<sup>3-5</sup>, the chemical composition underneath the surface Pt layer can significantly affect the outer most Pt surface electronic structure, which has resulted in a ten-fold improvement in the ORR catalytic activity. Such an enhancement has also been observed at the nano-scale<sup>6</sup>. The core/shell NP structure thus represents a promising group of materials for the ORR catalysis.

Another approach to improve the ORR activity is to develop non-precious metal catalysts to replace the expensive Pt catalysts used in the low-temperature FCs. In the past decade, researchers<sup>7,8</sup> have shown many progresses in this regard. For example, Fe-based catalysts have been demonstrated to show very comparable ORR catalytic activity

to that of Pt in both acid and alkaline. However, the lifetime of these materials in the actual FC operation is not yet sufficient and further work in the durability of the non-precious-metal-containing catalysts is therefore needed.

As stated in Chapter 3, the HOR presents an additional overpotential to the overall alkaline FC performance, which we found to account for almost 1/3 of the cathode voltage loss. Although a higher Pt catalyst loading on the anode in alkaline FCs can easily solve this issue, such a solution will lead to a more expensive FC, which is not desirable. More active catalysts for the HOR in alkaline FCs are therefore in demand for cost-efficient alkaline FCs.

### 5.3 References

1. Zhang, J.; Lima, F. H. B.; Shao, M. H.; Sasaki, K.; Wang, J. X.; Hanson, J.; Adzic, R. R., Platinum monolayer on nonnoble metal-noble metal core-shell nanoparticle electrocatalysts for O<sub>2</sub> reduction. *Journal of Physical Chemistry B* 2005, 109, (48), 22701-22704.
2. Mani, P.; Srivastava, R.; Strasser, P., Dealloyed Pt-Cu core-shell nanoparticle electrocatalysts for use in PEM fuel cell cathodes. *Journal of Physical Chemistry C* 2008, 112, (7), 2770-2778.
3. Stamenkovic, V.; Schmidt, T. J.; Ross, P. N.; Markovic, N. M., Surface composition effects in electrocatalysis: Kinetics of oxygen reduction on well-defined Pt<sub>3</sub>Ni and Pt<sub>3</sub>Co alloy surfaces. *Journal of Physical Chemistry B* 2002, 106, (46), 11970-11979.
4. Stamenkovic, V. R.; Fowler, B.; Mun, B. S.; Wang, G. F.; Ross, P. N.; Lucas, C. A.; Markovic, N. M., Improved oxygen reduction activity on Pt<sub>3</sub>Ni(111) via increased surface site availability. *Science* 2007, 315, (5811), 493-497.
5. Stamenkovic, V. R.; Mun, B. S.; Mayrhofer, K. J. J.; Ross, P. N.; Markovic, N. M., Effect of surface composition on electronic structure, stability, and electrocatalytic properties of Pt-transition metal alloys: Pt-skin versus Pt-skeleton surfaces. *Journal of the American Chemical Society* 2006, 128, (27), 8813-8819.
6. Zhang, J.; Yang, H. Z.; Fang, J. Y.; Zou, S. Z., Synthesis and Oxygen Reduction Activity of Shape-Controlled Pt<sub>3</sub>Ni Nanopolyhedra. *Nano Letters* 2010, 10, (2), 638-644.
7. Lefevre, M.; Proietti, E.; Jaouen, F.; Dodelet, J. P., Iron-Based Catalysts with Improved Oxygen Reduction Activity in Polymer Electrolyte Fuel Cells. *Science* 2009, 324, (5923), 71-74.
8. Meng, H.; Jaouen, F.; Proietti, E.; Lefevre, M.; Dodelet, J. P., pH-effect on oxygen reduction activity of Fe-based electro-catalysts. *Electrochemistry Communications* 2009, 11, (10), 1986-1989.



## Acknowledgement

I am grateful to my thesis supervisor Professor Yang Shao-Horn for providing me the great opportunity of entering the amazingly interesting electrochemical energy field. Her guidance, advices, and continuous assistance have helped me improve my experimental skills and independent research ability through my graduate study. The enlightening discussions with her often inspire me to do better.

I would like to thank Professor Hubert Gasteiger, who has been a great mentor and taught me how to conduct the best electrochemical measurements. I appreciate all the help and friendship from the group members of the electrochemical energy laboratory. Special thanks to Dr. Shuo Chen, who has helped me with large amount of HRTEM measurements, Ethan Crumlin, who has taken all the XPS measurements in my thesis work, and Jin Suntivich for proof-reading my thesis.

I would like to thank all my friends from MIT. Hong He, Wei Chai, Shuo Chen, Hongmei Yan, Yunpeng Yin and Minggang She et al have been very supportive. They have helped me not only in life but also provided instructive suggestions as to my graduate study. They have made my life at MIT enjoyable.

Lastly but most importantly, I would like to thank my parents, whom I am in the greatest debt to, for their selfless love and spiritual support through all these years. They have given me the most but asked the least for return. This thesis is dedicated to them.





## List of Publications

- **Wenchao Sheng**, Ethan J. Crumlin, Shuo Chen, Seungwoo Lee, and Yang Shao-Horn, "Synthesis of monodispersed Pt nanoparticles supported on multi-walled carbon nanotubes and their electrocatalytic activity", (in preparation)
- **Wenchao Sheng**, Shuo Chen, Elio Vescovo, and Yang Shao-Horn, "Particle Size Effect on the Oxygen Reduction Reaction Activity and Instability of Carbon-supported Pt Catalysts in Acidic Environment", (to be submitted)
- **Wenchao Sheng**, Hubert Gasteiger and Yang Shao-Horn, "Hydrogen Oxidation and Evolution Reaction Kinetics on Platinum: Acid vs. Alkaline Electrolytes", (Submitted)
- Seung Woo Lee, Shuo Chen, **Wenchao Sheng**, Naoaki Yabuuchi, Yong-Tae Kim, Tadaoki Mitani, Elio Vescovo, and Yang Shao-Horn, "The Roles of Surface Steps on Pt Nanoparticles in Electro-Oxidation of Carbon Monoxide and Methanol", *Journal of the American Chemical Society*, **131**, 15669-15677 (2009).
- Edward F. Holby, **Wenchao Sheng**, Yang Shao-Horn, Dane Morgan, "Pt nanoparticle stability in PEM fuel cells: influence of particle size distribution and crossover hydrogen", *Energy & Environmental Science* **2**, 865-871 (2009).
- Shuo Chen, **Wenchao Sheng**, Naoaki Yabuuchi, Paulo J. Ferreira, Lawrence F. Allard, and Yang Shao-Horn, "Origin of oxygen reduction reaction activity on Pt<sub>3</sub>Co nanoparticles: atomically resolved chemical compositions and structures", *Journal of Physical Chemistry C* **113(3)** 1109-1125 (2009).
- Shuo Chen, Paulo J. Ferreira, **Wenchao Sheng**, Naoaki Yabuuchi, Lawrence F. Allard, and Yang Shao-Horn, "Enhanced activities for oxygen reduction reaction on "Pt<sub>3</sub>Co" nanoparticles: Direct evidence of percolated and sandwich-segregation structures", *Journal of the American Chemical Society*, **130(42)**, 13818-13819 (2008).
- Y. Shao-Horn, **W. C. Sheng**, S. Chen, P. J. Ferreira E., Holby D. Morgan, "Instability of Supported Platinum Nanoparticles in Low-Temperature Fuel Cells", *Topics in Catalysis*, **46:285-30** (2007).
- **Wenchao Sheng**, Sungjee Kim, Jinwook Lee, Sang-Wook Kim, Klavs Jensen, and Mounqi G. Bawendi, "In-Situ Encapsulation of Quantum Dots into Polymer Microspheres", *Langmuir*, **22**, 3782-3790 (2006) (top 20 most accessed article in 2006).

- Longwu Chen, **Wenchao Sheng**, Lihua Gan, “Preparation of TiO<sub>2</sub> functional thin films and factors influencing their photocatalytic activity”, *Journal of Functional Materials*, 33(3), 246-249, 2002.